The Effect of Horizontal Magnetic Field on Liquid Metal Rayleigh-Bénard Convection

U. Burr, L. Barleon, K.-J. Mack, U. Müller
Institut für Angewandte Thermo- und Fluiddynamik
Projekt Kernfusion

The effect of horizontal magnetic field on liquid metal Rayleigh-Bénard convection

U. Burr, L. Barleon, K.-J. Mack, U. Müller

The effect of horizontal magnetic field on liquid metal Rayleigh-Bénard convection

Abstract

Thermal convection of liquid metals is considerably influenced by imposing an external magnetic field. Such magnetoconvective flows control the heat and tritium removal from the breeding material in current fusion blanket designs. A magnetic field may be used also to influence heat transfer controlled solidification in material processing like casting or crystal growth. As the geometries of technical applications are rather complex, a fundamental understanding of the phenomena may only be obtained from simple well defined configurations.

This report presents an experimental study of the influence of a horizontal magnetic field on the integral heat transfer and the temporal behavior of liquid metal Rayleigh-Bénard convection. For this specific flow configuration the magnetic field exerts not only a damping effect on the convective motions by Joule's dissipation, the non-isotropic character of the electromagnetic forces gives rise to the transition of the three-dimensional convective flow patterns into increasingly two-dimensional structures in the sense that convective rolls become aligned with the magnetic field.

The test section is a rectangular box of large aspect ratio 20 : 10 : 1 whereby a parameter range of Rayleigh numbers $0 < Ra < 10^5$ and of Chandrasekhar numbers $0 < Q < 1.44 \cdot 10^6$ is covered. The Prandtl number of the test fluid sodium potassium $Na^{22}K^{78}$ is very small i.e. $\mathrm{Pr} \approx 0.02$ and therefore the nonlinear inertial forces lead to strong time dependent flow.

The integral heat transfer across the layer is characterized by the Nusselt number, calculated from the time averaged temperatures at the upper and the lower boundary. Local, time-dependent temperatures are evaluated from a four-element temperature probe placed in the middle of the liquid metal layer. The non-coplanar arrangement of the thermocouples enables the evaluation of the time-dependent temperature gradient vector which allows to estimate the local isotropy properties of the time dependent flow.

From the Rayleigh- Nusselt number curves it has been demonstrated for the first time that a horizontal magnetic field may increase considerably the critical Rayleigh number for the onset of convection in a finite layer of fluid. The results are in reasonable agreement with predictions based on linear theory taking into account conducting Hartmann walls. At high supercritical conditions the electromagnetic forces cause a transition of the time dependent flow from a state of turbulent convection obtained at ordinary hydrodynamic conditions into an increasingly organized state where the temporal dynamics are dominated by only a few governing frequencies. For highly organized flow, the convective heat transfer is considerably increased and, even though Joule's dissipation may be strong, higher Nusselt numbers than in case of ordinary hydrodynamic flow are found. The probe measurements confirme that the time dependent flow exhibits a strong non-isotropic character in form of time dependent convective rolls aligned with the direction of the applied magnetic field.

Der Einfluß eines horizontalen Magnetfeldes auf Flüssigmetall Rayleigh-Bénard Konvektion

Zusammenfassung

Thermische Konvektionsströmungen können durch die Wirkung eines äußeren Magnetfeldes stark beeinflußt werden. Solch magnetokonvektive Strömungen bestimmen die Wärme- und Tritiumabfuhr aus dem Brutmaterial derzeitig betrachteter Fusionsblankets. Die gezielte Beeinflussung des Wärmetransportes und der Strömungsstruktur kann darüberhinaus zur Verbesserung von Materialprozessen wie dem Formguß oder dem Ziehen von Einkristallen eingesetzt werden.

In einem Experiment wird der Einfluß eines horizontalen Magnetfeldes auf den integralen Wärmedurchgang sowie das zeitliche Verhalten einer Flüssigmetall Rayleigh-Bénard Konvektionsströmung experimentell untersucht. Neben der zusätzlichen Dämpfung der Konvektionsbewegungen durch Joulsche Dissipation bewirkt die Anisotropie der elektromagnetischen Kräfte hier einen Übergang von dreidimensionalen Konvektionsmustern hin zu zweidimensionalen Konvektionsrollen, deren Achsen bevorzugt in Magnetfeldrichtung orientiert sind.

Die Teststrecke ist ein rechtwinkliger Behälter mit großem Seitenverhältnis 20 : 10 : 1, in dem ein Parameterbereich der Rayleigh-Zahlen $0 < Ra < 10^5$ und der Chandrasekhar-Zahlen $0 < Q < 14400$ untersucht wurde. Die Prandtl-Zahl der als Experimentierflüssigkeit eingesetzten Natrium-Kalium Legierung $Na^{22}K^{78}$ beträgt lediglich $Pr \approx 0.02$, so daß sich aus den nichtlinearen Trägheitskräften ein stark zeitabhängiger Strömungszustand ergibt.

Der integrale Wärmetransport durch die Flüssigmetallschicht wird anhand der Nusselt-Zahl charakterisiert, die aus den zeitlich gemittelten Temperaturen an der oberen und der unteren Berandung bestimmt wird. Lokale Temperaturschwankungen werden von einer Vier-Element-Temperaturprobe, die in Schichtmitte angeordnet ist, erfaßt. Die antiparallele Anordnung der Thermoelemente ermöglicht die Bestimmung des lokalen, zeitabhängigen Temperaturgradientenvektors. Aus diesem können die lokalen Isotropieeigenschaften der zeitabhängigen Strömung abgeleitet werden.

Anhand der Rayleigh- Nusselt-Zahl Kurven wurde erstmals gezeigt, daß bei endlicher Schichtbreite ein horizontales Magnetfeld die kritische Rayleigh-Zahl für das Einsetzen einer Konvektionsbewegung signifikant erhöht. Die erzielten Ergebnisse stimmen hinreichend mit Vorhersagen einer linearen Stabilitätsanalyse überein, bei welcher der Einfluß der Hartmann Wände berücksichtigt ist. Für stark überkritische Zustände bewirken die elektrodynamischen Kräfte einen Übergang der im Fall rein hydrodynamischer Strömung turbulenten Konvektionsströmung hin zu mehr und mehr geordneten Strömungsformen, bei welchen das Zeitverhalten lediglich durch wenige Schwankungsfrequenzen dominiert ist. Im Fall hochgradig geordneter Strömung steigt der konvektive Wärmetransport merklich an und trotz der hohen Joulschen Dissipation werden höhere Nusselt-Zahlen als bei rein hydrodynamischer Strömung erreicht. Anhand der Sondenmessungen zeigt sich, daß bei Anlegen eines Magnetfeldes das zeitabhängige Strömungsfeld dergestalt anisotrop wird, daß sich die Achsen zeitabhängiger Konvektionsrollen nach dem angelegten Magnetfeld ausrichten.

Contents

1 Introduction

When a liquid is exposed to a temperature gradient, the thermal expansion causes gradients in the density and from the acceleration of gravity a convective motion determined by buoyant, viscous and inertial forces may set in.

Thermal convection of liquid metals is an important phenomena that occurs in a wide range of technical applications. In current fusion blanket designs a lithium-lead alloy is used mainly as a breeding material whereas the heat deposited in the liquid metal is removed by water cooled tubes inside the liquid (Giancarli, Severy, Baraer, Leroy, Mercier, Proust and Quintric-Bossy (1992)). The externally forced flow required for a continuous circulation and for tritium extraction is very weak and buoyant flow may therefore become dominant.

As the flow of the electrically conducting fluid within the blanket is exposed to the strong magnetic field confining the fusion-plasma, electric currents are induced. The interaction of these currents with the applied magnetic field introduces Lorenz forces to the momentum balance of the flow and a magnetohydrodynamic (MHD) convective flow is established. From the generally damping effect of electromagnetic forces on fluid motion by Joule's dissipation the heat transfer from the liquid metal to the cooling tubes is expected to be significantly reduced. Without any knowledge about the magnitude of damping, the thermo hydraulic design may be carried out with the conservative approach of stagnant fluid with pure heat conduction. But for the removal of tritium respectively to avoid tritium accumulation at least some marginal velocity is necessary. Thus a clear understanding of the influence of the magnetic field on the convective motion is essential for the technical feasibility of such a blanket design.

An other field of technical application, where liquid metal convective phenomena are important, is the processing of metallic workpieces by casting or pulling large single crystals from a melt. In casting the solidification requires the removal of heat from the melt and a temperature gradient has therefore to be maintained between the cold mould and the melt giving rise to strong convective motion. The same situation holds when large single crystals are grown from a melt by the Czochralsky-process or zone-melting techniques. There, a temperature gradient has to be maintained even for practically infinite time.

Though, for the design of heat transfer units the suppression of convective motion by magnetic fields is an undesirable effect, for material processing it offers a powerful possibility to control various phenomena like the grain size or segregation during the solidification process. On one hand the convective motion causes an intense mixing of the melt ensuring homogeneous conditions at the liquid-solid interface. On the other hand if the temperature gradient is large, non-linear inertial forces may become dominant and unstable flow phenomena will lead to non-homogeneous physical properties in the solid. Only from the controlled suppression of either all or only time-dependent convective motions we can take benefit of magnetic fields to improve material processing. Moreover there are situations where the effect of the magnetic field is not a purely dissipative one. The spacial structure as well as the temporal dynamics of the flow can be influenced by well defined magnetic fields in such a way that an enhancement of heat transport becomes possible.

As the geometries of technical applications are rather complex, a fundamental understanding of the phenomena may only be obtained from simple well defined configurations.

3

This report presents an experimental study of liquid-metal Rayleigh-Bénard convection with an imposed horizontal magnetic field. In figure 1 the geometry and the coordinates of the investigated flow problem are sketched. An electrically well conducting fluid (liq-
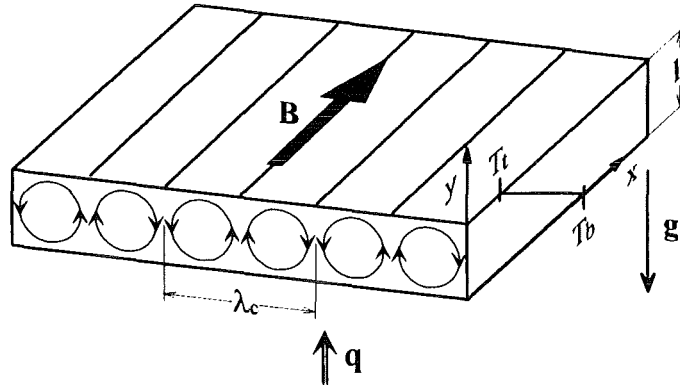
Figure 1: Geometry and coordinates of the investigated flow problem.

uid metal) is confined between two horizontal walls of distance h. By heating the lower boundary and by cooling the upper wall a temperature gradient is maintained parallel to the acceleration of gravity g. Due to the thermal expansion, the fluid at the bottom is lighter whereas the fluid at the upper wall is heavier. If the temperature gradient and therefore the differences in density exerts a certain critical value, a convective motion in the form of stationary convective rolls of distinct critical spacial wave length λ_c sets in. This onset of convection without magnetic field is determined by a single non-dimensional parameter. The Rayleigh number

$$Ra = \frac{\beta g \Delta T h^3}{\nu \kappa} \tag{1}$$

denotes the ratio of buoyant- to viscous forces. Where $\beta = 1/\rho \cdot d\rho/dT$ is the cubic thermal expansion coefficient defined as the relative change of the density ρ with temperature T, g the magnitude of the acceleration of gravity, $\Delta T = T_b - T_t$ the temperature difference between the lower and the upper fluid-wall interface, ν the kinematic viscosity and $\kappa = \lambda/\rho c_p$ the thermal diffusivity calculated from the thermal conductivity λ the density ρ and the specific heat c_p. The critical Rayleigh number for the onset of convection Ra_c is easily obtained by a linear stability analysis. If the non-slip condition ($\mathbf{v} = \mathbf{0}$) is satisfied at the upper and the lower wall and both bounding surfaces are isothermal the calculations of Pellew and Southwell (1940), and Reid and Harris (1958) have yielded

$$Ra_c = 1707.76 \tag{2}$$

at

$$a_c = 3.117.$$

Where a_c is the horizontal wave number which becomes unstable first at the point of marginal stability. The spacial wave number is calculated from $\lambda_c = 2\pi/a_c$ as $\lambda_c \approx 2$, indicating that instability sets in as convective rolls with the same horizontal length scale than the vertical determined by the height h of the layer.

4

At fixed experimental setup, the Rayleigh number depends only on the temperature difference across the layer and may therefore be used as a non-dimensional measure for the driving force of the flow. If the Rayleigh number is increased to supercritical conditions, the flow undergoes a transition from steady three-dimensional flow patterns to time dependent three-dimensional and finally turbulent flow (see Krishnamurti (1973), Clever and Busse (1974), Busse (1978), and Chu and Goldstein (1973)). As at higher Rayleigh numbers the convective velocities are increased, inertial forces become more important in the momentum balance and the Prandtl number

$$Pr = \frac{\nu}{\kappa} \tag{3}$$

occurs as an additional relevant parameter that further controls the coupling between the velocity and the temperature field. From definition 3 the Prandtl number turns out to be independent of the flow problem and describes therefore the characteristic physical properties of the investigated fluid in case of pure natural convection. As the Prandtl number of liquid metals usually is very small non-linear inertial forces are leading to strong time dependent flow.

This experiment is the continuation of a previous one described in Burr, Barleon, Mack and Müller (1999), where the influence of a vertical magnetic field $\mathbf{B}$ (parallel to the y direction) of magnitude B_0 has been investigated. At this configuration, the vortex like convective motions always have to cross magnetic field lines and therefore the magnetic field exerts a strong damping effect on the convective motions by Joule's dissipation. Altough strong non isotropic electromagnetic forces act on the flow the horizontal symmetry of the convective patterns is not broken by the magnetic field i.e. no predominant orientation of convective rolls in the horizontal directions can be observed. The damping effect by the magnetic field here is familiar with the dissipation of isotropic velocity fluctuations in MHD turbulence that acts on the short time scale $\tau_{JD} \sim \rho/\sigma B_0^2$ (see Shercliff (1965)). When the hight of the layer h is taken as a characteristic length scale of a vortex, viscous dissipation acts on the time scale $\tau_{VD} \sim h^2/\nu$. The ratio of this time scale to the one of Joule's dissipation gives the non-dimensional Chandrasekhar number

$$Q = \frac{B_0^2 h^2 \sigma}{\rho \nu} \tag{4}$$

denoting further the ratio of electromagnetic to viscous forces. The Chandrasekhar number may further be used as a non-dimensional measure for the strength of the applied magnetic field.

In the present experiment a homogeneous magnetic field $\mathbf{B}$ of magnitude B_0 was imposed to the layer parallel to the x coordinate. In MHD duct flows it is convinient to calculate the characteristic number denoting the strength of the applied magnetic field using the half width of the duct in the direction of the magnetic field as a characteristic length. Here we will keep the hight of the layer for the calculation of the Chandrasekhar number because in an infinite layer of fluid this is the only characteristic length of the problem.

With the maintenance of a temperature difference between the upper and lower boundaries, a heat flux $\mathbf{q}$ of magnitude q is passing the layer (see figure 1). The effectivity of the convective heat transport is characterized by the non dimensional Nusselt number

$$Nu = \frac{q}{q_0} \tag{5}$$

5

defined from the ratio of the total heat flux q to the one of pure heat conduction at the same temperature difference. From Fouriers law q_0 is calculated as

$$q_0 = \lambda \frac{\Delta T}{h}. \qquad (6)$$

At subcritical conditions the Nusselt number becomes unity whereas the occurrence of convective heat transport at supercritical conditions is indicated by Nusselt numbers larger than one. With provided geometrical similarity the Nusselt number depends on all three parameters i.e. the Rayleigh number, the Prandtl number and the Chandrasekhar number and furthermore on the electrical conductivity of the walls. For an overview, Nusselt numbers of ordinary Bénard convection, obtained in several relevant experiments with different Prandtl numbers are summarized in Kek (1989).

For a horizontal magnetic field, the directional character of the electromagnetic forces leads to the formation of convective roll pattern with roll axis predominantly aligned with the magnetic field. This effect has already been outlined by Chandrasekhar (1961) and is demonstrated in the experiments of Lehnert and Little (1956), Fauve, Laroche, Libchaber and Perrin (1984) and Kishida and Takeda (1994). The dynamics of this process are essentially the same like for the formation of two-dimensional (2D) or quasi two-dimensional (Q2D) MHD turbulence in duct flows (see Burr (1998) and literature cited therein).

Compared to flow fields with isotropic velocity fluctuations Joule's dissipation is considerably reduced by the elongation of vortex structures in the direction of the magnetic field (see Davidson (1995)). In this case electric currents, induced by the vortex motion in planes perpendicular to the magnetic field, have to close over longer distances along the magnetic field lines and therefore the current density in the fluid is reduced. However, if the applied magnetic field is strong enough a two-dimensional roll pattern is established which in an infinite layer exhibits no more Joule's dissipation. But if the layer is finite, i.e. the fluid is confined between two vertical walls perpendicular to the magnetic field, the vortices have to match the non-slip condition at these, so called Hartmann walls. This is obtained by the formation of thin Hartmann layers whereas, if the magnetic field is strong enough, the flow in the core region remains two-dimensional. With their deviation from the pure two-dimensional state the Hartmann layers provide an additional current path for the electric currents induced by the fluid motion and Joule's dissipation occurs even though the flow is two-dimensional except in the boundary layers. We will see in the later sections that this Joule's dissipation of Q2D-flow, commonly called Hartmann braking, depends not only on the strength of the applied magnetic field but also on the extension of the layer in the direction of the magnetic field and on the electrical conductivity of the Hartmann walls.

From the strong aligning effect of the magnetic field two-dimensional vortices are formed at MHD flow, the three-dimensional cascading process of large vortices towards small scale structures at ordinary hydrodynamic (OHD) flow is inhibited and from this viscous dissipation may be considerably reduced by the magnetic field. If the effect of Joule's dissipation is smaller than the reduced viscous dissipation, the convective velocities are relatively increased and therefore an enhancement of heat transfer may be observed when imposing a magnetic field.

The influence of a horizontal magnetic field on the temporal dynamics of Rayleigh-Bénard convection was investigated experimentally by Fauve, Laroche and Libchaber

(1981), Libchaber, Laroche and Fauve (1982), Libchaber, Fauve and Laroche (1983), Fauve et al. (1984) and Kishida and Takeda (1994), computations have been performed by Busse and Clever (1983) and Busse and Clever (1989) but most of the present works are limited to marginal supercritical Rayleigh numbers. Although we intend to compare our experimental results with the results of the above literature the presented experiment is focused on the high Rayleigh and Chandrasekhar numbers as they occur in technical applications. From the evaluation of heat transfer rates the blanket design may be improved and the study of the temporal dynamics may give an estimate of the possibilities of melt control in materials processing. Furthermore, results obtained in the well defined geometry of the experimental setup can be used to develop computer codes for the simulation of MHD-natural convection. Here, special emphasis is posed on the question for what parameters the flow may be described by a simplified model using two-dimensional equations.

2 Governing equations

Most MHD flows in technical systems are well described by the limiting case of $Pm \ll 1$ with the magnetic Prandtl number $Pm = \nu\mu\sigma$ as the ratio of viscous momentum transport to diffusive transport of the magnetic field, where μ is the magnetic permeability. In this case and by using the Bousinesq assumption, the buoyant flow is governed by the following set of inductionless equations for conservation of

mass, momentum and charge

$$\nabla \cdot \mathbf{v} = 0, \tag{7}$$

$$\frac{1}{\mathrm{Pr}} \left[\frac{\partial \mathbf{v}}{\partial t} + (\mathbf{v} \cdot \nabla) \mathbf{v} \right] = -\nabla p^* + \mathbf{\Delta v} + Ra T \mathbf{e}_y + Q \mathbf{j} \times \mathbf{B}, \tag{8}$$

$$\nabla \cdot \mathbf{j} = 0, \tag{9}$$

Ohm's law

$$\mathbf{j} = -\nabla\phi + \mathbf{v} \times \mathbf{B} \tag{10}$$

and the temperature equation

$$\frac{\partial T}{\partial t} + (\mathbf{v} \cdot \nabla) T = \Delta T \tag{11}$$

In these equations $\mathbf{r} = (x, y, z)$, $\mathbf{v} = (u, v, w)$, $\mathbf{j} = (j_x, j_y, j_z)$, $\mathbf{B} = (b_x, b_y, b_z)$, ϕ, t and T denote the non-dimensional coordinates, velocity, current density, magnetic field, electric potential, time and temperature. They are obtained by introducing the scales h, v_0, $\sigma v_0 B$, B, $h v_0 B$, t_0 and ΔT. Here $p^* = h^2(p + \rho g h)/(\rho\nu\kappa)$ is the non-dimensional pressure and $\mathbf{e}_y$ is the unit vector directed opposite to the gravity vector. The characteristic time-scale is the thermal diffusion time $t_0 = h^2/\kappa$. A characteristic velocity is then $v_0 = h/t_0$. A frequency f can be scaled by the characteristic frequency $f_0 = 1/t_0$.

The electrical conductivity of walls is expressed by the non dimensional wall conductance ratio

$$c = \frac{\sigma_W s}{\sigma h}, \tag{12}$$

where σ_W and σ are the electrical conductivities of the wall material and the fluid and s is the thickness of the wall considered.

7

From Ohm's law (equation 10), the motion of an electrically conducting fluid under the influence of a magnetic field induces a potential gradient $\nabla \phi = \mathbf{v} \times \mathbf{B} - \mathbf{j}$. Electric currents $\mathbf{j}$ are driven along the gradient of the electric field forming current loops that may either close within the fluid or in conducting walls. By interaction with the magnetic field, the current density induces Lorenz forces $\mathbf{F}_L = \mathbf{j} \times \mathbf{B}$ which act perpendicular to the current density and the magnetic field and enter the momentum equation of the fluid.

3 Basic Phenomena

3.1 Natural convection

The inverse density gradient in the fluid induces a recirculating vortex like motion with a characteristic time scale namely the eddy turnover time

$$\tau_{to} = d/v_0 \tag{13}$$

where d is a characteristic length scale i.e. the diameter of the vortex and v_0 a characteristic velocity i.e. the tangential velocity. In order to estimate the relevance of Lorenz forces on the vortex motion we first define characteristic time and velocity scales for the convective motion in the case of purely hydrodynamic flow.

In natural convection all kinetic energy per volume of the fluid $k_e = \rho/2v_0^2$ is produced by buoyant forces that scale as $F_b \simeq \beta \rho g \Delta T$. From the balance of the energy per volume of fluid released by the work of buoyant forces $e_b \simeq F_b \cdot h$ and the kinetic energy the buoyant velocity

$$v_b \simeq \sqrt{2\beta g \Delta T h} \tag{14}$$

is obtained as a new velocity scale. Introducing the buoyant velocity in equation 13 $(v_0 = v_b)$ we obtain the buoyant time-scale

$$\tau_b \simeq \frac{d}{\sqrt{2\beta g \Delta T h}}. \tag{15}$$

Furthermore, the buoyant velocity defines a Reynolds number as the ratio of inertial to viscous forces in the form

$$\mathrm{Re} = \frac{v_0 h}{\nu} = \sqrt{\frac{Ra}{\mathrm{Pr}}}, \tag{16}$$

where the factor two has been neglected for convenience. Generally unstable flow phenomena can be characterized by the balance of non-stationary inertial forces $F_{iu} \simeq \rho v_0/\tau$ and stationary inertial forces $F_{is} \simeq \rho u^2/d$ resulting in a Strouhal number $Str = d/v_0\tau$. Thus similar time scales τ are expected for stable as well as for unstable flow phenomena.

3.2 The effect of a horizontal uniform magnetic field

In closed cavities the flow is always influenced by walls. A qualitative description of the influence of a magnetic field on the vortex dynamics in natural convective flows can be obtained by simple arguments formulated for isolated vortex structures evolving in time and space in an otherwise quiescent fluid.

If we consider an isotropic time dependent motion of a fluid lump initiated by a three-dimensional buoyant release from the upper or the lower boundary layer, the motion is

affected on a Joule's dissipation time-scale $\tau_{JD} \simeq \rho/\sigma B_0^2$ similarly to the decay of isotropic MHD turbulence (see Shercliff (1965)). The ratio of the Joule's dissipation time-scale to the characteristic time-scale of the vortex motion, i.e. the eddy turnover time, gives a non-dimensional Joule's time-scale

$$\tau_{JD}^* = \frac{1}{N} \tag{17}$$

which proves to be the inverse of the interaction parameter

$$N = \frac{\sigma d B_0^2}{\rho v_0} \tag{18}$$

based on the characteristic length scale d of a single vortex. The interaction parameter is well known in MHD flows and denotes the ratio of electromagnetic and inertial forces. If N is small the momentum equations approach the hydrodynamic balance exhibiting isotropic flow finally. If N is large, isotropic convective motions decay on a fast time scale. If the characteristic velocity in definition 18 is replaced by the viscous buoyant velocity v_b defined in equation 14, the interaction parameter

$$N = \frac{Q}{\mathrm{Re}}\frac{h}{d} = Q\sqrt{\frac{\mathrm{Pr}}{\mathrm{Ra}}}\frac{d}{h} \tag{19}$$

may be obtained from the Chandrasekhar number Q and the Reynolds number Re which, furthermore may be expressed from equation 16 by the Rayleigh- and the Prandtl number. Additionally, the ratio of the eddy diameter to the height of the layer enters. When d decreases the interaction parameter decreases and therefore higher isotropy is expected at smaller scales. This might lead to the argument that there is always isotropic motion if the length scale is only small enough. But small eddies are damped by viscosity on a viscous dissipation time-scale $\tau_V = d^2/\nu$. Scaling with the eddy turnover time and using the buoyant velocity the non dimensional decay time of viscous dissipation is obtained as a Reynolds number based on the characteristic length of the eddy d. This dimensionless time-scale may be expressed in terms of Rayleigh and Prandtl numbers:

$$\tau_V^* = \mathrm{Re}_d = \sqrt{\frac{Ra}{\mathrm{Pr}}}\frac{d}{h}. \tag{20}$$

We conclude, when Re_d becomes small, viscosity will strongly damp the convective motion.

Furtheron, we restrict ourselves to situations where Re_d is large and N is moderate or large. In this case an isolated vortex structure can be considered as approximately inviscid and an initially three-dimensional flow structure will then evolve from inertia into an increasingly two-dimensional structure in the sense that the velocity distribution becomes uniform in the direction of the magnetic field.

The formation of a convective flow pattern consisting of rolls predominantly orientated in the direction of the magnetic field can be explained by considering single vortex structures with different orientations in respect to the magnetic field. In figure 2a a convective roll with axis perpendicular to the horizontal magnetic field is sketched. From the horizontal motion perpendicular to the magnetic field potential differences are induced parallel to the roll axes. The potential gradients $\nabla\phi = \mathbf{v} \times \mathbf{B}$ left and right of the vortex center oppose each other and therefore electric currents close near the periphery of the convective roll and a high current density is produced. The induced Lorenz forces
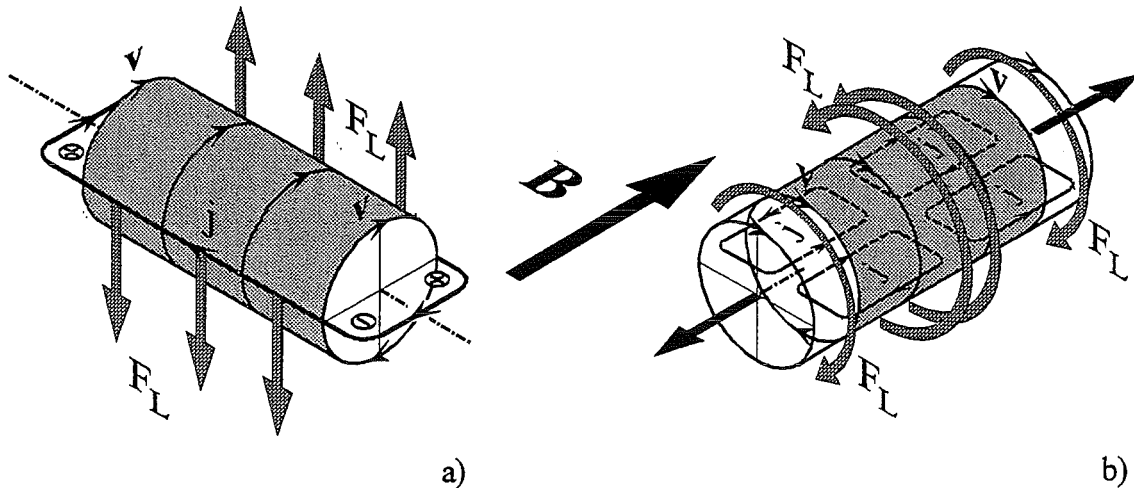
9

Figure 2: Current density **j** and Lorentz forces $\mathbf{F}_L$ induced by the action of a horizontal magnetic field **B** on vortex motion at velocity **v**. a) roll axis perpendicular to the magnetic field and b) roll axis aligned with the magnetic field.

$\mathbf{F}_L = \mathbf{j} \times \mathbf{B}$ are opposing the vertical motions of the fluid and cause therefore strong electromagnetic damping.

In figure 2b the other limiting case of a convective roll with an axis aligned with the horizontal magnetic field is sketched. The circulating flow in the plane perpendicular to the applied magnetic field induces a radial potential difference $\nabla\phi = \mathbf{v} \times \mathbf{B}$. Electric currents driven by this potential difference close along magnetic field lines in the quiescent fluid zones in the vicinity of the vortex. Within the region of swirl the Lorentz force $\mathbf{F}_L = \mathbf{j} \times \mathbf{B}$ opposes the motion, whereas in the quiescent regions at the ends of the vortex the non vanishing Lorentz force accelerates the fluid at rest and thereby propagate the vortex motion in the direction of the main vortex axis. Thus in some way the electromagnetic forces provide a transport mechanism of kinetic energy along magnetic field lines.

For large interaction parameters N Sommeria and Moreau (1982) have described the tendency of turbulent structures to extend in the direction of magnetic field lines as a preferred electromagnetic diffusion process of vorticity $\boldsymbol{\omega} = \nabla \times \mathbf{v}$ in this particular direction. It is characterized by a diffusivity $\alpha = \sigma B^2 l_\perp / \rho$ based on a length scale perpendicular to the magnetic field $l_\perp$ of the eddy, which is in our case the diameter d. The axial diffusion process implicates differences in the velocity field of two transverse planes of a distance l to be equalized on a time-scale $\tau_D \cong (\rho/\sigma B^2)(l^2/d^2)$. By forming the ratio of this diffusion time-scale to the eddy turnover time we obtain the non-dimensional diffusion time scale as

$$\tau_D^* \cong \frac{1}{N}\left(\frac{l}{d}\right)^2. \tag{21}$$

Introducing equation 19 yields

$$\tau_D^* \cong \frac{1}{Q}\sqrt{\frac{Ra}{Pr}}\frac{hl^2}{d^3}. \tag{22}$$

If the magnetic forces act for a long enough time on the vortex any differences in the velocity distribution along the direction of magnetic field are removed and a pure two-dimensional flow is established provided that this is consistent with the boundary

conditions and that inertial forces are not destabilizing the flow. Applying the curl-operator to equation (10) we obtain

$$\nabla \times \mathbf{j} = \mathbf{B} \cdot \nabla \mathbf{v}. \tag{23}$$

From this relation it follows that the current density is curl-free if the velocity field does not vary in the direction of the applied magnetic field. Irrotational contributions to the current density do not appear in unbounded flows and thus, the electromagnetic forces disappear. Thereby the effect of the magnetic field is reduced to maintaining the two-dimensionality of the velocity field. The flow itself is governed by two-dimensional hydrodynamics. However, a purely two-dimensional state can only be obtained in an infinite layer of fluid. If the layer of fluid is confined by vertical walls perpendicular to the magnetic field the convective rolls have to match the non-slip boundary condition at Hartmann walls. In this case the maximum diffusion length l is the extension of the layer in the direction of the magnetic field respectively the distance between the two Hartmann walls. If the diffusion process of kinetic energy along this distance is faster than the characteristic time-scale of the convective motion, i.e. if the non-dimensional diffusion time τ_D^* defined by equation 21 is small, isotropic disturbances of the velocity field are quickly equalized and the condition $\tau_D^* \ll 1$ holds for the formation of a so called quasi-two-dimensional (Q2D) flow. In figure 3a the expected flow pattern of Q2D flow for a Rayleigh-Bénard convection is sketched. In the center of the liquid metal layer we have convective rolls with uniform velocity distribution in the direction of the magnetic field. These vortices match the non-slip boundary condition at the Hartmann-walls by the formation of individual Hartmann layers. From definitions 21 and 22 we conclude, that the diffusion time depends significantly on the characteristic scale of the vortex d. Thus, vortices of smaller scales may exhibit higher isotropy than large scale motions.

In figure 3b the current paths of one particular convective roll at Q2D flow is shown. Due to the reduced circulating velocity in the boundary layer, the induced electric potential is smaller at the Hartmann walls. The Hartmann layers and the Hartmann walls, provided they are electrically conducting, offer therefore a closure path for the electric currents induced in the core region. The electromagnetic forces are damping the convective motions in the core by Joule's dissipation in the Hartmann walls and Joule's and viscous dissipation in the Hartmann layers. The characteristic time-scale for this process, called Hartmann braking, has been given by Sommeria and Moreau (1982) for insulated Hartmann walls as $\tau_H \cong b/B_0(\rho/\sigma\nu)^{1/2}$, where $b = l/2$ is half of the distance between the Hartmann walls. Scaling by the eddy turnover time gives the non-dimensional time-scale for the decay of a vortex confined by insulating Hartmann walls. One gets

$$\tau_H^* = \frac{M}{N} \tag{24}$$

where

$$M = B_0 b \sqrt{\frac{\sigma}{\rho\nu}} \tag{25}$$

is the Hartmann number M which is the square root of the Chandrasekhar number based on the characteristic length in the direction of the magnetic field b i.e. half of the distance between the Hartmann walls.
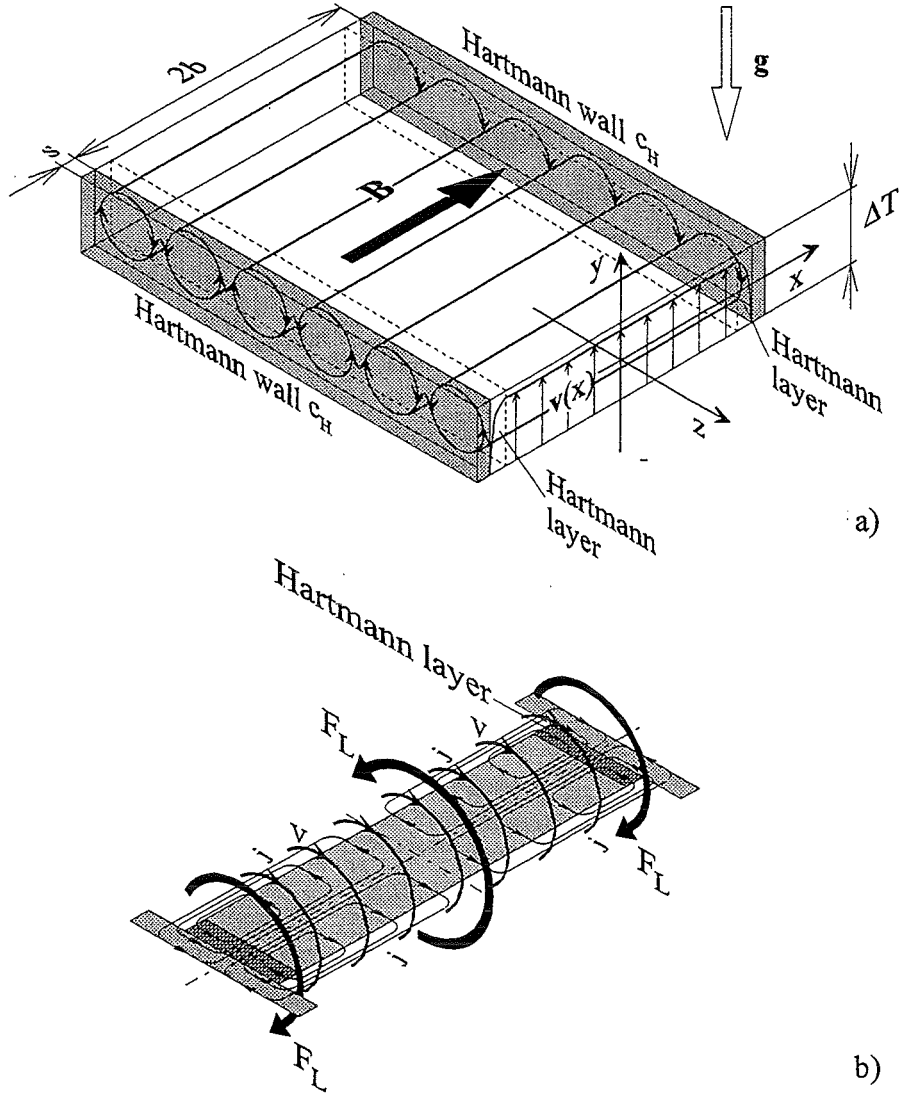
Figure 3: Quasi two-dimensional (Q2D) flow at high magnetic fields. a) Flow pattern of convective rolls aligned with the magnetic field. Perfect two dimensional flow is inhibitid by the non-slip condition at Hartmann walls perpendicular to the magnetic field. b) Electric currents and Lorenz forces in one vortex. The electric currents induced by the fluid motion close in the Hartmann layer and in the electrically conducting Hartmann wall. Thus energy is removed from the core region and dissipated in the Hartmann layers and the Hartmann walls by Joule's and viscous dissipation.

This theory of Hartmann braking has been extended by Bühler (1996) to conditions of thin conducting Hartmann walls of conductivity c_H. Bühler derives the expression

$$\tau_H^* = \left(\frac{N}{M} + \frac{c_H N}{1 + c_H} \right)^{-1}, \tag{26}$$

where the current path in the wall is represented by the second term in the brackets. c_H

12

is the uniform wall conductance ratio of the Hartmann walls

$$c_H = \frac{\sigma_W s}{\sigma b} \tag{27}$$

which, in this case is based also on b. Introducing equation 19 in equation 26 and substituting definition 27 by definition 12 we obtain

$$\tau_H^* = \sqrt{\frac{Ra}{Pr}} \frac{h}{d} \left(\frac{\sqrt{Q}}{b/h} + \frac{c_H Q}{b/h + c_H} \right)^{-1} . \tag{28}$$

The non dimensional decay time of quasi-two-dimensional flow τ_H^* may serve as one and only similarity parameter describing the effect of the magnetic field, provided that the flow is quasi two-dimensional. The electromagnetic damping now may be increased by either increasing the Chandrasekhar number, the electrical conductivity of the Hartmann wall or by reducing the aspect ratio b/h. The influence on the flow will be the same in all cases. Any damping effect disappears even at high Chandrasekhar numbers if the extension of the layer in the direction of the magnetic field is large respectively b/h tends to infinity.

If τ_H^* has a moderate or large size the damping effect of the magnetic field is weak, whereas small values are indicating strong damping even though the flow is quasi two-dimensional. Both the diffusion time-scale τ_D^* (equation 22) and the decay time of quasi two-dimensional flow τ_H^* are decreasing with increasing Chandrasekhar number. Therefore the promotion of Q2D flow is coupled with an increased damping of the motion by Hartmann braking.

Bühler (1996) derived two-dimensional equations for duct flow that take into account Hartmann braking of Q2D flow. In the next section these equations are extended to the situation of buoyant convection in order to obtain a simplified treatment of this problem in case of high magnetic fields.

3.3 Formulation of two-dimensional equations

For the formulation of two-dimensional equations describing Q2D flows we refer to figure 3a. The fluid domain is limited in the direction of the magnetic field by two thin electrically conducting walls of distance $2b$ and uniform wall conductance ratio c_H where b is now the non dimensional half width between the Hartmann walls (scaled by h) and c_H is calculated from equation 27. Symmetry conditions at $x = 0$ hold and the thin wall condition (Walker (1981))

$$-c\nabla_t^2 \phi = \mathbf{j} \cdot \mathbf{n} \tag{29}$$

is assumed to be valid at the vertical walls. The magnetic field is strong enough, or more precisely, the diffusion process along the magnetic field is fast enough to obtain Q2D flow (see section 3.2). The flow may then be split up in two regions: Firstly the core region with uniform flow properties along the direction of the magnetic field and secondly the Hartmann layers where the non-slip condition holds and boundary layers occur showing a steep decrease of the velocity. Flow properties in the core region will further be denoted by a superscript c those in the Hartmann layers by a superscript δ. Finaly, the temperature field is assumed to be independent from the direction of the magnetic field.

It is essential for the validity of simplified two-dimensional equations for Q2D flows that the electric potential induced by the fluid motion is uniform along the magnetic

field. At walls parallel to the magnetic field (side walls), thin viscous boundary layers are formed. In case of electrically insulating walls ($c = 0$) the boundary layers introduce an additional electric resistance for the current paths towards the Hartmann walls which results in a potential difference in the direction of the magnetic field. If walls parallel to the magnetic field are assumed to be perfect electrical conductors ($c \to \infty$) potential differences along the magnetic field in the near wall region vanish. Provided that the diffusion process along the magnetic field is fast enough we may then obtain Q2D flow even in the presence of side walls.

Q2D flows are well described by the balance of momentum and heat in a plane of the core region, perpendicular to the magnetic field (see figure 3a). Applying curl ($\nabla\times$) to the momentum equation 8 we obtain a conservation equation for the vorticity $\omega = \partial_y w - \partial_z v$ in the x direction in the form

$$\frac{1}{\mathrm{Pr}} \left[\partial_t \omega + \partial_y \psi \partial_z \omega - \partial_z \psi \partial_y \omega \right] = \nabla^2_{yz} \omega - Ra \partial_z T + Q \partial_x j_x \tag{30}$$

which describes, together with a two-dimensional temperature equation

$$\partial_t T + v \partial_y T + w \partial_z T = \nabla^2_{yz} T \tag{31}$$

the thermo-convection in the y, z-plane. ψ is a stream function from which $v = -\partial_z \psi$ and $w = \partial_y \psi$ are defined and $\nabla^2_{yz} = (\partial_{yy} + \partial_{zz})$ is the vertical Laplacian in the y, z-plane.

From figure 3b it is seen that the two-dimensional flow in the y, z-plane is overlapped by a three dimensional distribution of the current density. In order to reduce the problem to the two dimensions of the flow the variations of the current density along the magnetic field represented by the electromagnetic term in equation 30 have to be expressed by analytical methods that take into account the current path via the Hartmann walls.

Applying the divergence operator $\nabla\cdot$ to Ohm's law (equation 10) and using the conservation of charge (equation 9) we obtain

$$\nabla^2 \phi = \left(\partial_{xx} + \nabla^2_{yz} \right) \phi = \omega. \tag{32}$$

Calculating the derivative ∂_x of the current density j_x in x-direction from Ohm's law

$$\partial_x j_x = -\partial_{xx} \phi = \nabla^2_{yz} \phi - \omega \tag{33}$$

the electrodynamic term in equation 30 may be expressed as a function of properties defined in the yz-plane only.

In the viscous Hartmann layers the balance of forces is mainly governed by viscous and Lorenz forces. Introducing equation 33 and the rescaled coordinate $\zeta = x/\delta$ in equation 30 we obtain a simplified vorticity equation

$$\frac{1}{\delta^2} \partial_{\zeta\zeta} \omega \delta + Q \omega \delta = 0 \tag{34}$$

which describes the distribution of vorticity $\omega\delta$ in the boundary layers. From this equation we obtain the scaling law of the thickness of the Hartmann layer namely $\delta_H \sim Q^{-1/2}$. As the balance of forces in the Hartmann layer is independent of the coordinates perpendicular to the magnetic field, the distribution of the flow properties ω and ψ along the

direction of the magnetic field may be expressed by a separation ansatz using a shape function $f(x)$ in the form (see figure 3a):

$$\omega(x,y,z) = \omega_c(y,z) \cdot f(x), \quad \psi(x,y,z) = \psi_c(y,z) \cdot f(x). \tag{35}$$

Equations (35a and b) determine the flow in the core as well as in the Hartmann layers. The shape function $f(x)$ has to satisfy the non-slip condition $f(\pm b) = 0$ and the symmetry condition $\partial_x f(0) = 0$. For large Chandrasekhar numbers f corresponds to the solution of Hartmann's problem and we obtain

$$f = 1 - e^{\sqrt{Q}(x-b)}. \tag{36}$$

As the Hartmann layers are very thin the approximation

$$\frac{1}{b} \int_0^b f(x) = 1 \tag{37}$$

can further be made.

Introducing equations 35a and b and 36 into the vorticity equation 30 and Ohm's law (equation 32) and using the thin wall condition (equation 29) we obtain after integrating along x and using equation 37, two-dimensional equations describing the electric potential

$$\nabla_{yz}^2 \phi = \frac{b}{b + c_H} \omega \tag{38}$$

and the vorticity

$$\frac{1}{\text{Pr}} \left[\partial_t \omega + \partial_y \psi \partial_z \omega - \partial_z \psi \partial_y \omega \right] = \nabla^2 \omega - Ra \partial_z T - \frac{\omega}{\tau} \tag{39}$$

where

$$\frac{1}{\tau} = \frac{\sqrt{Q}}{b} + \frac{Q c_H}{b + c_H} \tag{40}$$

The influence of the magnetic field on the flow is represented by the last term of equation 39. The similarity parameter τ is the non-dimensional decay time of Q2D flow by Joule's dissipation. It corresponds to the parameter defined by Bühler (1996) that is given in equation 26.

For electrically insulating Hartmann walls ($c_H \to 0$) the damping effect exhibits the asymptotic limit $1/\tau \sim Q^{1/2}$ whereas for electrically well conducting Hartmann walls ($c_H \to \infty$) $1/\tau \sim Q$ determines mainly the damping of vortices.

The vorticity equation 39 and the two-dimensional temperature equation 31 form a complete set of equations to perform analytical and numerical investigations of quasi two-dimensional flow. Moreover, the electric potential induced by the fluid motion can be calculated from equation 38. It has to be mentioned, that the effect of magnetic field in this equations is only dissipative. Dissipation by the magnetic field may only be reduced by growing two-dimensionality of the flow and thereby reducing viscous dissipation. Burr and Müller (1997) performed a detailed analytical and numerical investigation of Q2D Rayleigh-Bénard convection. Here we will refer to some results being relevant for the present experimental investigation.

15

3.4 Onset of convection

The onset of convection from the state of pure heat conduction has been investigated by Chandrasekhar (1961) in a linear stability analysis. For a magnetic field exactly parallel to the acceleration of gravity a strong damping effect of the magnetic field was demonstrated by significantly higher values of the critical Rayleigh number for the onset of convection with increasing Chandrasekhar number Q. Simultaneously the critical wave number at the onset of convection increases with the magnetic field indicating smaller horizontal scales of the convective flow pattern. If the magnetic field is inclined to the direction of gravity, convection at marginal stability will manifest itself as longitudinal rolls aligned with the horizontal component of the magnetic field, whereas for the delay in the onset of convection only the vertical component of the magnetic field is active. The onset of convection as longitudinal rolls in case of a purely horizontal magnetic field has been demonstrated in an experiment by Lehnert and Little (1956). They otherwise did not observe any discernible inhibition of convection by the magnetic field and, however they observed horizontal streamlines running parallel to the magnetic field. This last observation does not match our idea of quasi two-dimensional flow and is presumably an effect of the geometrically circular test section.

In case of a rectangular box with vertical walls exactly perpendicular to the horizontal magnetic field, the situation is well defined and we can expect the onset of convection to occur in the form of quasi two-dimensional rolls aligned with the magnetic field.

Burr and Müller (1997) performed a linear stability analysis based on the governing equations 38, 39 and 31 of quasi two-dimensional flow. The geometry and the coordinates of the flow problem are given in figure 3. Under the assumption that both horizontal walls are isothermal and perfect electrical conductors, linearizing the governing equations and assuming periodic solutions of the form

$$F(z) = \exp[iaz] \tag{41}$$

where a is the horizontal wave number they obtained the linearized differential equation

$$\left(\partial_{yy} - a^2\right)^3 \psi(y) - \frac{1}{\tau}\left(\partial_{yy} - a^2\right)^2 \psi(y) = -Ra \cdot a^2 \psi(y) \tag{42}$$

which defined the marginal state at the onset of convection as a stationary motion. The additional stiffness introduced by Joule's dissipation of Q2D flow is represented by the second term on the left side of equation 42.

If slip conditions hold at both horizontal walls the basic mode of odd functions in the intervall $0 < y < 1$

$$\psi(y) = \cos(\pi y) \tag{43}$$

for the vertical constituent of the solution leads, by minimizing the function $Ra(a)$, to the critical wave number:

$$a_c = \frac{\pi}{2}\sqrt{\sqrt{\xi^2 + 8\xi} - \xi}, \quad \xi = 1 + \frac{1}{\pi^2 \tau} \tag{44}$$

and the critical Rayleigh number

$$Ra_c = \frac{\left(\pi^2 + a_c^2\right)^3 + \frac{1}{\tau}\left(\pi^2 + a_c^2\right)^2}{a_c^2} \tag{45}$$

at the onset of convection. In figures 4a and b the critical wave number and the corresponding critical Rayleigh number are plotted versus the decay time of Q2D flow $1/\tau$. The critical wave number increases from the value for purely hydrodynamic flow

a)

b)
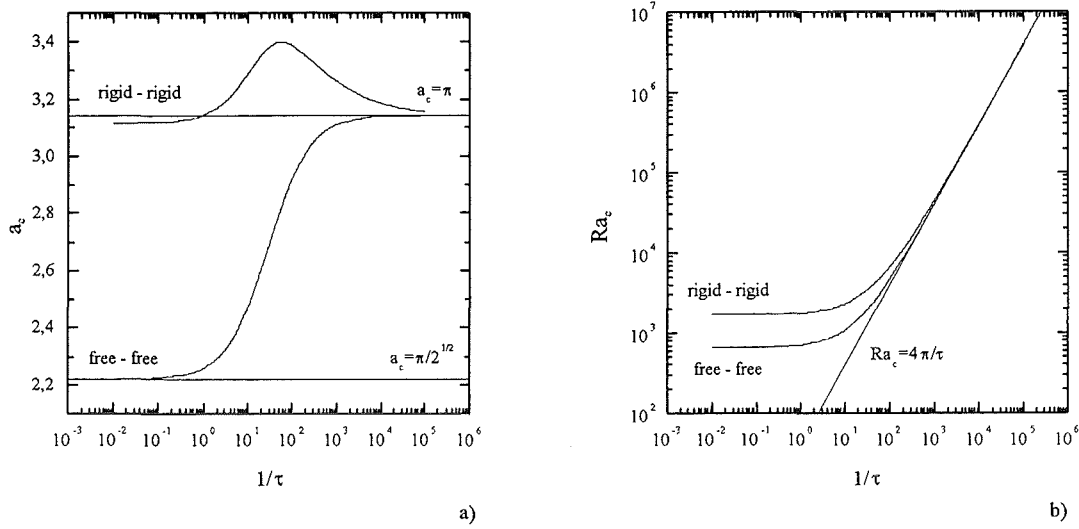
Figure 4: Onset of convection as stationary motion from the state of pure heat conduction for Q2D flow in the pressence of Hartmann walls perpendicular to the magnetic field. a) critical wave numbers and b) critical Rayleigh numbers. The influence of the magnetic field is expressed by the inverse of the non-dimensional decay time $1/\tau = \sqrt{Q}/b + Qc_H/(b+c_H)$.

$a_c(1/\tau \rightarrow 0) = \pi/2^{1/2}$ continuously to the asymptotic value at high electromagnetic damping $a_c(1/\tau \rightarrow \infty) = \pi$. In the same way, the critical Rayleigh number increases monotonously from $Ra_c(1/\tau \rightarrow 0) = 27\pi^4/4$ and finally approaches a linear asymptotic law. This asymptotic behaviour can be evaluated by neglecting the effect of viscous friction, described by the first term in equation 42. One obtains

$$Ra_c = \frac{4\pi^2}{\tau} \tag{46}$$

for

$$a_c = \pi. \tag{47}$$

If both horizontal boundaries are considered to provide non-slip conditions the critical values may not be obtained from simple analytical calculations. By expanding $\psi(y)$ into a Fourier series the calculations of Burr and Müller (1997) have yielded the correspondingly denoted values in figures 4a and b. The critical Rayleigh numbers increase from the value at hydrodynamic flow $Ra_c(1/\tau \rightarrow 0) = 1708$ and match at large $1/\tau$ the asymptotic behavior of inviscid flow. The critical wave numbers exhibit an unusual behavior. The values are first increasing from the limiting value at purely hydrodynamic flow $a_c(1/\tau \rightarrow 0) = 3.117$ but then reach a maximum of about $a_c \approx 3.4$ at $1/\tau \approx 60$, from which they decrease when the magnetic field is further increased to the asymptotic value of the inviscid case $a_c = \pi$. Thus, the horizontal length-scale of the convective rolls may, in a certain range of wave numbers be reduced by the magnetic field at a rate of about 10%.

17

4 Experimental setup

The experimental testing was realized in the MEKKA facility of the Institute of Applied Thermo and Fluid Dynamics (IATF) of the Research Center Karlsruhe (FZK). The MEKKA facility has been outlined in details by Barleon, Mack and Stieglitz (1996). The test section is precisely the same as the one described in an earlier report (Burr et al. (1999)) except that a superconducting solenoid magnet was used to generate a horizontal magnetic field instead of the normal conducting magnet that produced the purely vertical magnetic field in the previous experiment. Nevertheless, in the following we outline the main features of the experimental setup once more.

4.1 The test facility

In figure 5a the cross section of the test apparatus is shown. A longitudinal cross section and a view from the top can be obtained from figure 6. The dimensions of the liquid
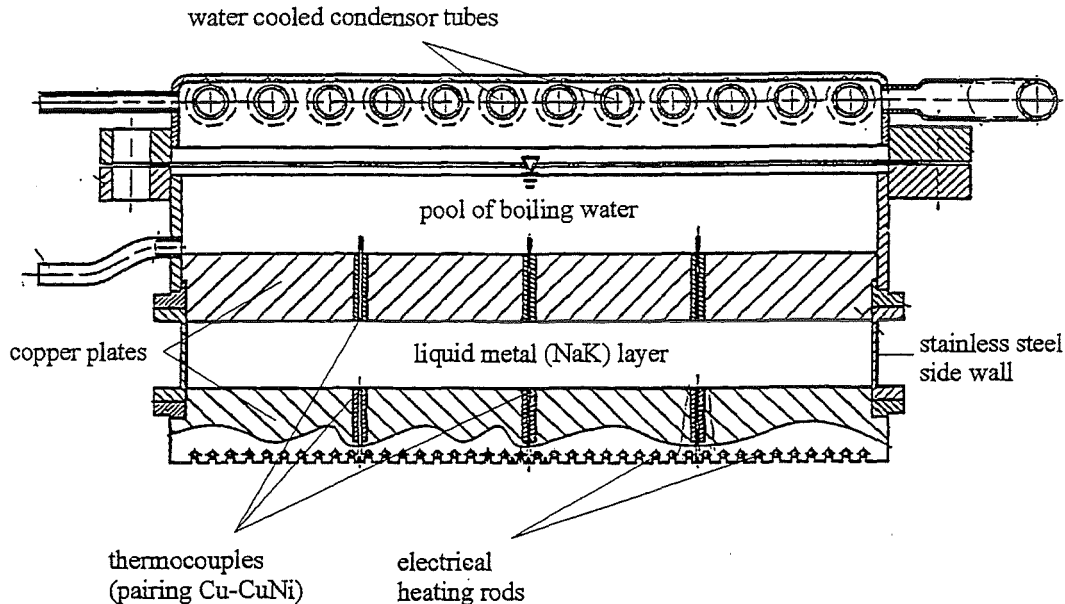
Figure 5: Crossection of the test facility. The liquid metal layer (NaK) is confined between two horizontal copper plates.

metal layer are $20mm$ in height, $200mm$ in width and $400mm$ length giving an aspect ratio of $1 : 10 : 20$. The lower and the upper walls are made of copper plates of $20mm$ thickness, the side walls consist of $1.5mm$ stainless steel sheet metal with an electrical conductivity of $\sigma_W = 1.37 \cdot 10^6 1/\Omega m$. Together with the electrical conductivity of NaK at $120°C$ ($\sigma = 2.4735 \cdot 10^6 1/\Omega m$) we obtain the wall conductance ratio of the Hartmann walls defined by equation 27 as $c_W = 4.1536 \cdot 10^{-3}$. The electrical conductivity of copper $\sigma_{Cu} = 5.81 \cdot 10^7 1/\Omega m$ is significantly higher than the one of NaK resulting in a wall conductance ratio of $c = 23.5$. Thus we may assume the horizontal walls as perfect electrical conductors.

The heat flux is supplied to the lower wall by 40 electrically powered heating rods which are soldered with silver brass into their individual groves to assure good thermal contact.

18

a)   b)
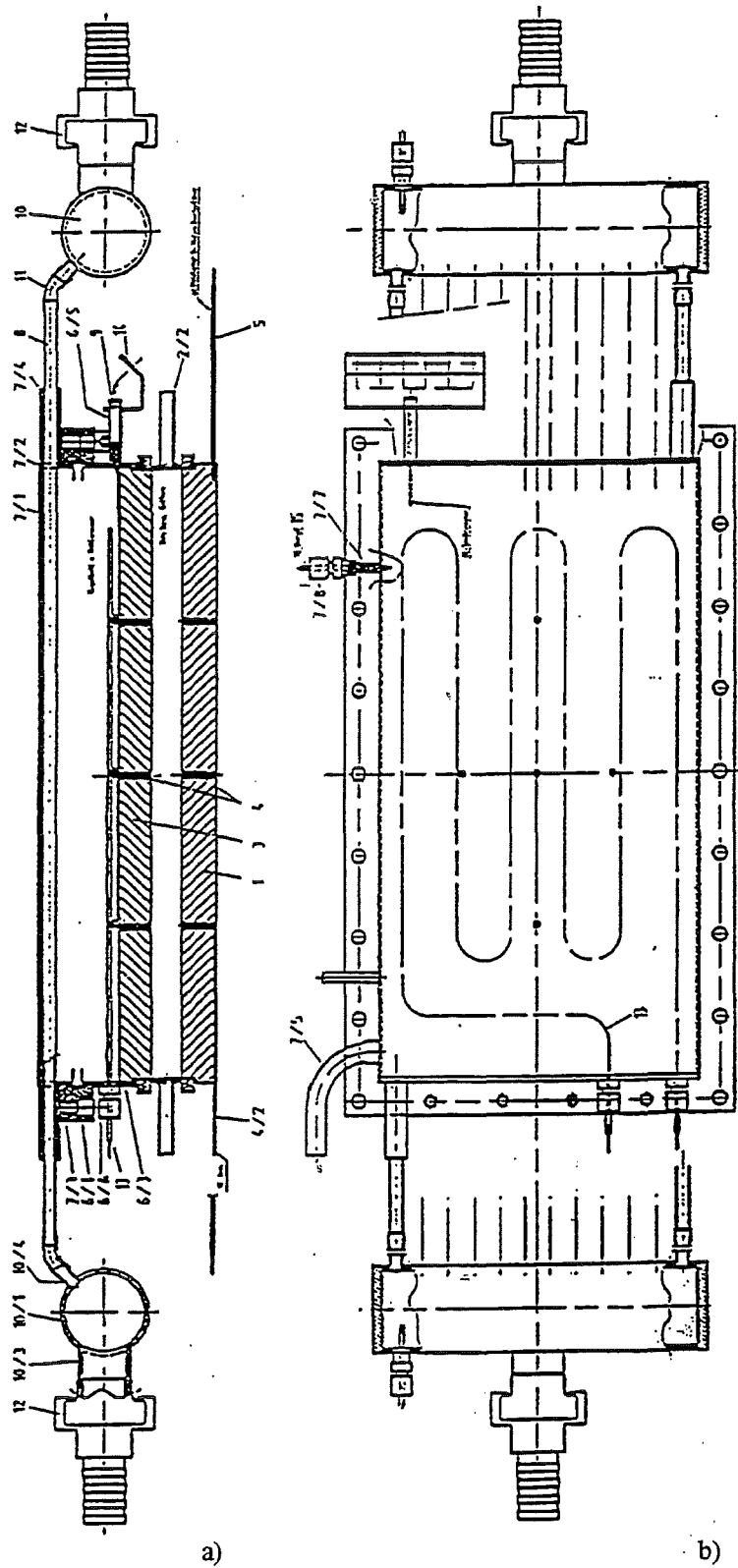
Figure 6: a) longitudinal cross section and b) top view of the test section.

At a maximum heating power of $P = 10.8kW$ a uniform heat flux of $q = 1.35 \cdot 10^5 W/m^2$ can be obtained.

The heat is removed from the upper wall by a boiling pool of water. The steam is condensed on 12 longitudinal copper tubes which are cooled by water from an external loop. In order to get a well defined boiling process with constant superheating of the wall, the pool is filled with glass spheres of $5mm$ diameter. The uniform temperature of the boiling liquid is able to equalize immediately any horizontal temperature variations imposed for example from the condenser and thus a homogeneous temperature distribution at the upper copper plate is obtained.

At small heat flux the heat losses at the pool side walls are inhibiting homogeneous boiling and the temperature distribution at the upper copper plate might become inhomogeneous. To overcome this deficiency, the steam area above the water line was fitted with an additional electrical heating rod to balance heat losses. It turned out that with a moderate overheating of the boiling pool homogeneous temperatures at the upper walls can be maintained.

The magnetic field is produced by a super conducting magnet which provides a homogeneous horizontal magnetic field up to 3.5 *Tesla*. In figure 7 the test section is placed in front of the magnetic bore which has a diameter of $400mm$. In order to facilitate the
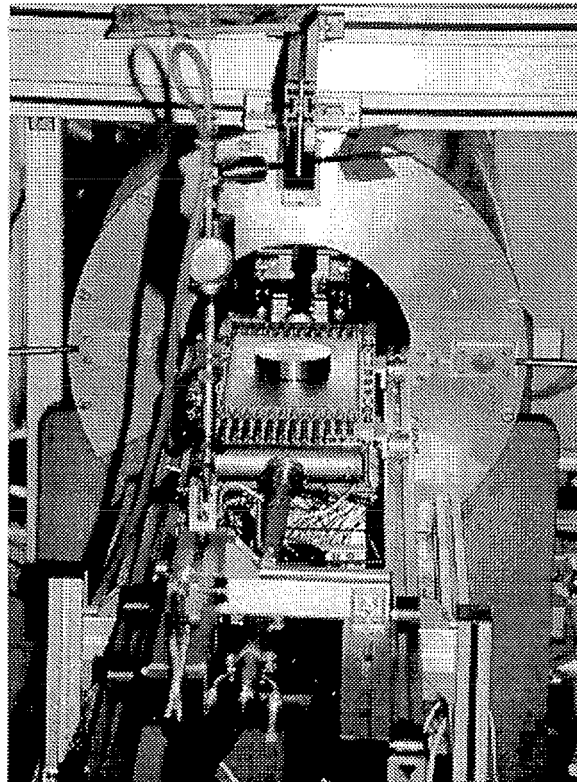
Figure 7: Test section placed in front of the magnetic bore of the super conducting solenoid magnet producing the horizontal magnetic field. For performing the experiments, the test section was isolated and moved on rails into the center of the magnetic bore.

experiments, the test section was thermally isolated and moved on rails into the center of the magnetic bore. The orientation of the test section in respect to the magnetic field

	$Na^{22}K^{78}$	H_2O	
ρ	842.4	998	$[kg/m^3]$
β	0.31	$0.18_{15°C}$	$[10^{-3}]$
ν	$0.5766 \cdot 10^{-6}$	$1.00 \cdot 10^{-6}$	$[m^2/s]$
λ	23.56	0.598	$[W/mK]$
c_p	936.84	4179	$[J/kgK]$
σ	$2.4735 \cdot 10^6$	10^{-9}	$[1/\Omega m]$
κ	$2.5853 \cdot 10^{-5}$	$1.4338 \cdot 10^{-7}$	$[m^2/s]$
Pr	0.019	6.97	$[-]$

Table 1: Thermophysical data of eutectic sodium-potassium alloy $Na^{22}K^{78}$ at $120°C$ compared with the ones of water (H_2O) at $20°C$

was chosen such that its longer side is parallel to the magnetic field lines.

Eutectic sodium-potassium alloy $Na^{22}K^{78}$ was chosen as a test fluid, the temperature dependent thermophysical properties of this liquid metal which is liquid above $T = -11°C$ are calculated from the polynomials in appendix A.1. In table 1 the thermophysical properties of NaK at $120°C$ are compared with those of water (H_2O) at $20°C$ taken from Gieck (1981).

The most significant difference is found in the values of the heat conductivity λ. Together with the smaller heat capacity c_p this leads to a much higher thermal conductivity κ and finally to a Prandtl-number which is two orders of magnitude lower that the one of water.

With this experimental setup the range of parameters $0 < Ra < 10^5$ and $0 < Q < 7 \cdot 10^6$ can be covered. As the Rayleigh and the Chandrasekhar number are controlled by the physical parameters temperature difference ΔT and the magnitude of the applied magnetic field B_0 they may be arbitrarily chosen for a parameter study. But an other situation holds for the Prandtl number which, as a physical property, depends only on the temperature of the fluid. The boiling water pool fixes the temperature at the upper plate to the boiling temperature of water $(T \approx 100°C)$. Higher temperature differences are achieved only by increasing the temperature of the lower plate. Thereby the mean temperature of the liquid and the Prandtl number increases when higher Rayleigh numbers are chosen. In the experimental temperature range $100°C < T < 200°C$ the Prandtl number varies in the range $0.021 < Pr < 0.013$. In order to enable a precise comparison with theoretical predictions the Prandtl number realized in the experiments will be presented also.

4.2 Instrumentation

In the experiments the Rayleigh number is controlled by the magnitude of the applied heat flux q, respectively, the supplied electrical power P. The temperatures at the lower and the upper boundaries are measured by five $Cu - CuNi$ thermocouples inserted into each copper plate. The measuring points of the thermocouples are located at a distance of only $e = 1mm$ from the fluid wall interface. The temperatures at the fluid wall interface are obtained from an interpolation based on Fourier's law (equation. 6) using the thermal conductivity of copper $\lambda_{Cu} = 384W/mK$. In figure 8 the horizontal positions of the thermocouples are shown. They are counted as an array $T_{i,j}$, where the first index i denotes the horizontal position (i.e. M for the central one and the four winds N, S, E

and W) and the second j is indicating the bottom respectively the top wall by b and t. In order to investigate local time dependent flow quantities, a four-element temperature
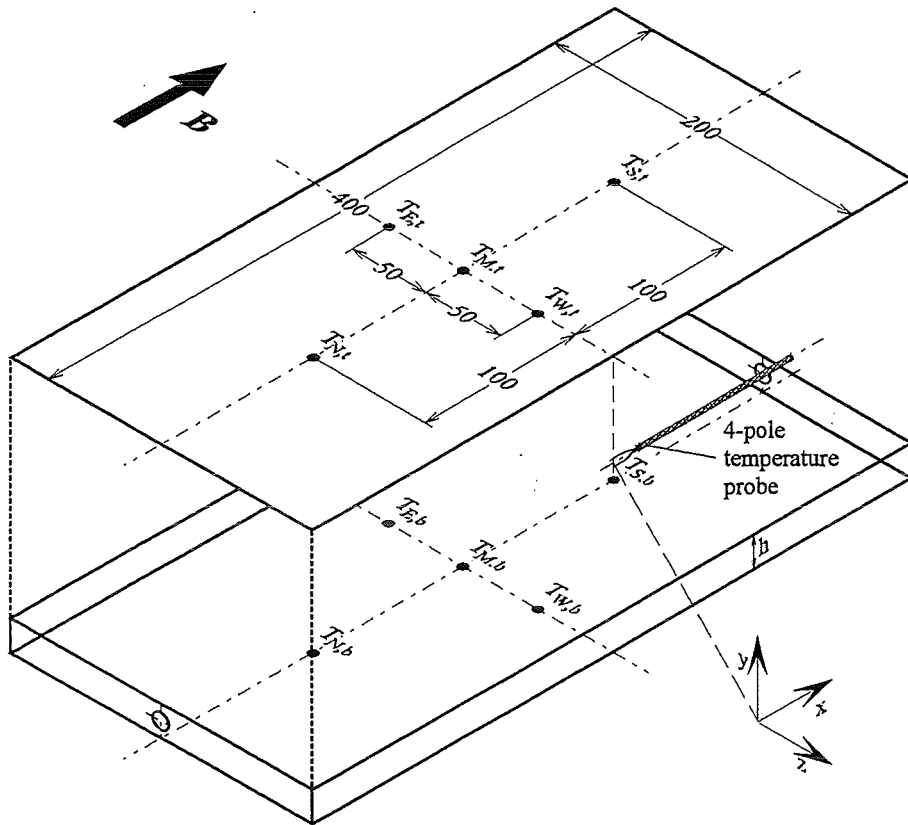
Figure 8: Instrumentation of the heat transfer test facility. Five $Cu-CuNi$ thermocouples are placed at the upper and the lower fluid wall interface to obtain integral heat transfer characteristics. Right in the middle of the fluid layer, between the thermocouples $T_{S,b}$ and $T_{S,t}$, a four-element temperature probe is placed in order to investigate local time-dependent flow quantities. All lengths are given in mm.

probe is placed within the fluid layer, right in the middle between the positions of the thermocouples $T_{S,b}$ and $T_{S,t}$ (see figure 8). In figure 9a the sensing tip of the probe is shown in comparison with a match. The probe shaft is made of an isolating ceramics tube with an outer diameter of $2mm$. Four $Ni-CrNi$ thermocouples of $0.25mm$ diameter are protruding out of the tube into the fluid forming the sensing tip. The precise arrangement of the thermocouples and the distances between them are shown in figure 9b. The non-coplanar arrangement of the thermocouples allows to approximately measure the time dependent temperature gradient ∇T in the fluid by finite differences (see appendix B). As the three-dimensional temperature gradient is a vector property it is possible to obtain additional information on the spacial structure of the convective flow even from a local measurement.

4.3 Data acquisition and evaluation

In the further discussion, any flow variable $\Phi(t)$ is considered to consist of a temporal mean part $\overline{\Phi}$ denoted by an overbar and a fluctuating part with zero mean value $\Phi'(t)$
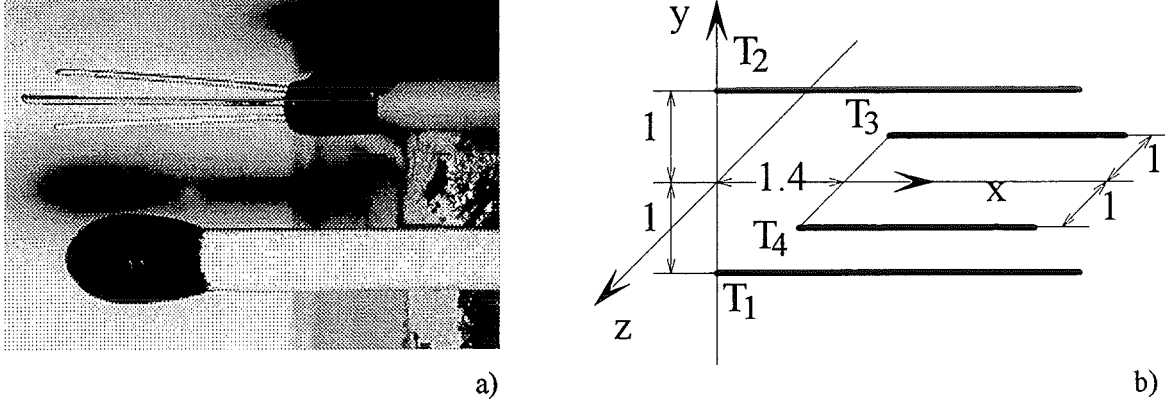
Figure 9: Four-element temperature probe. a) Sensing tip in comparison with a match. b) Geometry of the sensing tip and coordinates.

denoted by a prime. For a detailed definition of statistic properties see appendix D. When recording signals, a quantity $\Phi(t)$ is not obtained as a steady function. Instead, in a time period τ, discrete values Φ^t are recorded for example at an acquisition frequency f_{aq}. Where the upper index t runs from $t = 1$ to the number of acquired points $t = N$ calculated from $N = f_{aq} \cdot \tau$.

The data acquisition is performed by two independent systems. If we are only interested in the temporal mean value of quantities such as the temperatures of the copper plates, the supplied power, and the magnitude of the magnetic field, the data are recorded by a data logger with an acquisition frequency $f_{aq} = 1/30s$. The thermo-voltages U_T obtained from the thermocouples are measured in reference to an ice point $(0°C)$ reference thermocouple. The temperature values in $T[°C]$ are calculated from the standard polynoms for $Cu - CuNi$ thermopairing given in appendix C.

The spacial averages of the temperatures at the lower T_b^t and the upper T_t^t fluid-wall interface are determined for each time step from the non-weighted averages of the five thermocouples as

$$T_b^t \;=\; \frac{1}{5}\left(T_{M,b}^t + T_{N,b}^t + T_{S,b}^t + T_{E,b}^t + T_{W,b}^t\right), \tag{48}$$

$$T_t^t \;=\; \frac{1}{5}\left(T_{M,t}^t + T_{N,t}^t + T_{S,t}^t + T_{E,t}^t + T_{W,t}^t\right). \tag{49}$$

The mean temperature of the fluid is obtained from the relation

$$T_m^t = \frac{T_b^t + T_t^t}{2}. \tag{50}$$

With this mean value the dimensionless groups are calculated in each time step from the physical properties. From the individual time series the temporal mean values of all quantities are calculated at the end of each measurement. As already mentioned, we are not interested in the temporal variations of the characteristic numbers or the temperature differences across the layer the averaging procedure is taken for granted and not further indicated e.g. $Ra = \overline{Ra}$.

23

The time dependent thermo-voltages of the four-element-thermocouple probe are recorded simultaneously by a data acquisition card fitted into a second Personal Computer. In order to have a long time intervall reference for the thermopotential, the thermocouples are first connected to an ice point before their signals are amplified by standard DC amplifiers with a gain of $G = 500$. The temperature values in $T[^{\circ}C]$ are calculated from the thermo-voltages using the standard polynom for $Ni - CrNi$ thermopairing given in appendix C. With the use of amplifiers, the resolution and the signal to noise ratio of the measurement is significantly increased. But it turns out that the mean values of temperature are not obtained with sufficient accuracy due to shifts in the amplifiers offsets. Therefore the probe measurements are limited to temperature fluctuations.

The acquisition time of all experiments is chosen long enough that good statistics for the mean values of the stationary quantities such as Rayleigh- and Nusselt- numbers, but also mean square (ms) values of the probe signals can be achieved.

A more elaborate evaluation of the temporal behavior of the flow, such as power spectra, becomes possible from longer time series. In appendix E the parameters of all performed experiments are summarized.

4.4 Power supply

One general difficulty in performing natural convection experiments is that their temporal dynamics are acting on long time-scales. This requires to maintain constant conditions in an experiment over long time intervalls up to several hours in order to obtain good statistics. Especially at low heating power the Nusselt number is very sensitive to variations of the electric power and the range below $P \approx 4000W$ is therefore covered by controlled power units. Above $P \approx 4000W$ non-controlled units had to be used but the variations of the electric power network at such high power are small and do not to influence the measurements.

The electric power supplied to the bottom copper plate is the crucial control parameter of the facility. It directly determines the heat flux passing the layer and governs the temperature difference across the layer, respectively the Rayleigh number. As the temperature difference across the layer is measured by thermocouples, the Rayleigh number is calculated independently of the applied heat flux, but the heat flux directly enters the Nusselt number and has to be determined with high accuracy.

Therefore the heat flux per area q is calculated from the applied electric power P by taking into account different sources of heat losses:

1) Heat conduction in the stainless-steel side walls confining the layer,

2) Heat conduction from the lower plate through the thermal insulation to the environment,

3) Ohm's losses in the wiring of the heater rods.

4.5 Time scales in the setup

With the dimensions of the experimental setup $h = 0.02m$, $b = 0.20m$ and the wall conductance ratio of the Hartmann walls $c_H = 4.1536 \cdot 10^{-3}$, the times scale derived in section 3.1 can be evaluated as functions of the characteristic numbers Ra, Pr and Q. For

the following estimates a constant Prandtl number Pr = 0.019 is assumed corresponding to a mean temperature of the fluid $T_m = 120°C$. Further we assume convective rolls of the size of the height of the layer i.e. $d = h$.

In figure 10a the buoyant time-scale defined by equation 15 is plotted versus the Rayleigh number. On the left axis, the dimensional values are given. The right axis

a)   b)
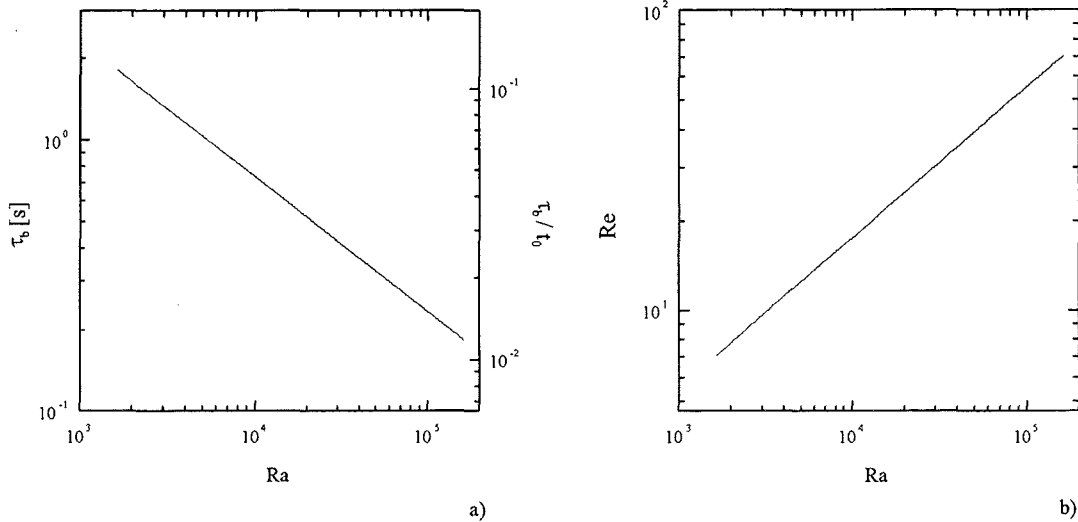
Figure 10: a) Buoyant time-scale τ_b (equation 15) as a function of Rayleigh number. Left axis: dimensional values, right axis: non-dimensional values obtained from scaling with the thermal diffusion time $t_0 = h^2/\kappa \approx 15.5s$. b) Reynolds number (equation 20) based on the buojant velocity. Pr = 0.019, $d = h$.

denotes the non-dimensional values obtained from scaling with the thermal diffusion time $t_0 = h^2/\kappa = 15,5s$. The values are decreasing with Rayleigh number indicating faster dynamics of the flow at larger supercritical conditions. Even at very low values of the Rayleigh number the buoyant time-scale is significantly smaller than the thermal diffusion time. Thus the velocity field may impose significant disturbances on the temperature distribution. In figure 10b the Reynolds number, respectively the non-dimensional viscous time-scale, calculated from equation 20 is shown. Values significantly larger than unity are indicating that inertial forces dominate the viscous friction. This clearly seems to be the case for values $Ra \gtrsim 10^4$. Compared to the viscous time-scale the dissipation of isotropic velocity fluctuations by Joule's dissipation (equation 17) is a very fast process. In figure 11a Joule's time scales, calculated with the interaction parameter defined from equation 19, are plotted for square roots of Chandrasekhar numbers $Q^{1/2} = 200$, $Q^{1/2} = 400$, $Q^{1/2} = 600$ and $Q^{1/2} = 800$. The use of $Q^{1/2}$ instead of Q to denote the strength of the applied magnetic field was choosen just for convinience. Notice that $Q^{1/2}$ is not the Hartmann number defined by equation 25 because there M is calculated from the half width of the layer in the direction of the magnetic field b. From the right axis of figure 11a the corresponding interaction parameters N are obtained. The high values of N are indicating that the Lorentz forces are dominating the momentum balance at these high values of the Chandrasekhar numbers. As the Reynolds numbers also achieve high values, we can expect an initially three-dimensional flow structure to evolve into an increasingly two-dimensional structure by diffusion of angular momentum along the magnetic field
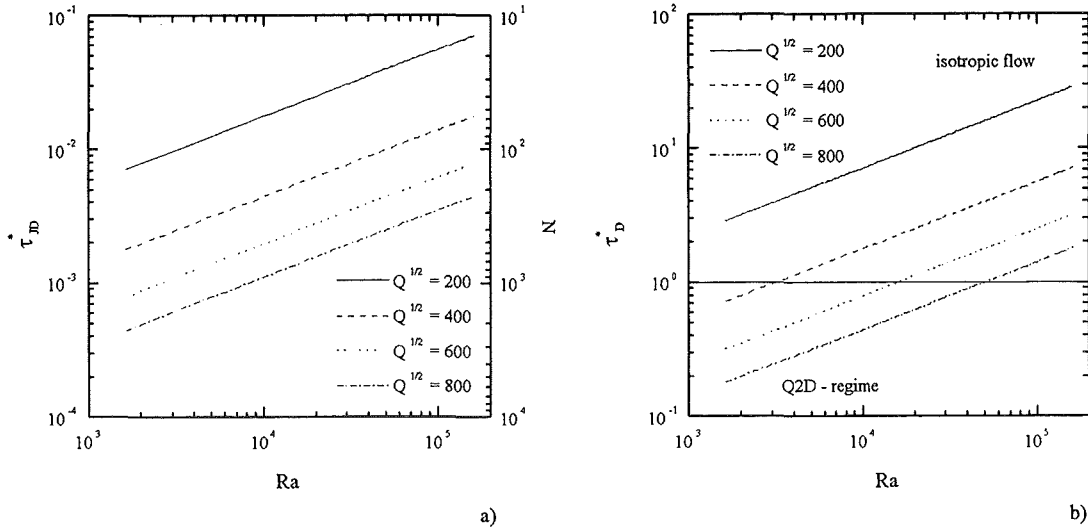
Figure 11: a) Decay time of isotropic flow by Joule's dissipation (Joule's time-scale equation 17) calculated as the inverse of an interaction parameter defined from equation 19. b) Diffusion time of angular momentum along the magnetic field given by equation 22. $Pr = 0.019$, $d = h$ and $l = 0.40m$.

lines as described in section 3.1. In figure 11b the time-scale of this diffusion process is plotted for the same Chandrasekhar numbers as in figure 11a. The values are calculated from equation 22 by taking into account the largest available length-scale, the extension of the layer in the direction of magnetic field $l = 2b = 0.4m$. There is a considerable range of values significantly lower than one. There the equalization of velocity differences along magnetic field lines is much faster than the temporal dynamics of the convective motions and we can expect the formation of Q2D flow whereas in the region of high values of the diffusion time $\tau_D^* \gg 1$ three-dimensional flow patterns may persist.

In regiems where a quasi two-dimensional flow is established the effect of a magnetic field is described purely on the non-dimensional decay time of Q2D flow τ_H^* defined from equation 28. τ_H^* is governed by the similarity parameter $1/\tau$ (equation 40) plotted in figure 12a as a function of the Chandrasekhar number. Below $Q \approx 10^4$ the similarity parameter asymptotes $1/\tau \sim Q^{1/2}$, above $Q \approx 10^5$ the influence of the electrical conductivity of the Hartmann walls becomes obvious and an increase as $1/\tau \sim Q$ is obtained finally. The squares in figure 12a are representing the $1/\tau$ values at $Q^{1/2} = 200$, $Q^{1/2} = 400$, $Q^{1/2} = 600$ and $Q^{1/2} = 800$. Introducing these values in equation 28 we obtain the decay time τ_H of Q2D flow plotted in figure 12b as a function of the Rayleigh number. From the comparison of the obtained values with the Joule's time-scale for the damping of isotropic motions (figure 11a) it is obvious that with the formation of 2D structures dissipation by electromagnetic forces is significantly reduced. Moreover, Joule's dissipation of Q2D flow is significantly lower than viscous dissipation at the large scale flows (see figure 10b).

Up to now all scales have been derived under the assumption of large scale motion ($d = h$) but at least for high Rayleigh numbers smaller structures related to shorter time scales are expected to occur. Under the assumption that they are created by the shear of the larger convective rolls, the magnitude of their characteristic velocity remains unchanged but the characteristic time-scale calculated from equation 15 decreases linearly

26
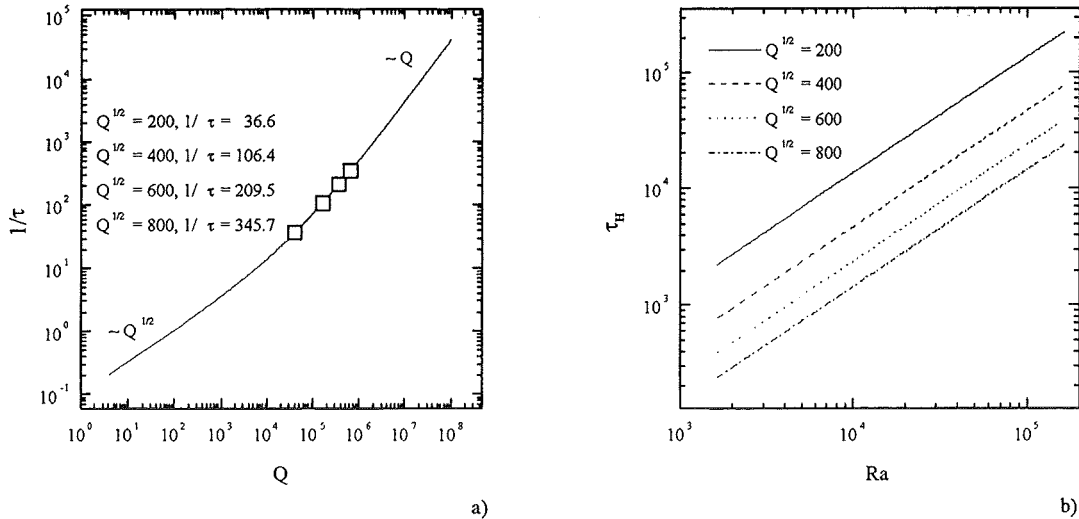
Figure 12: a) Similarity parameter $1/\tau$ of magnetic damping of $Q2D$ flow defined from equation 40 as a function of Chandrasekhar number. b) Non-dimensional decay time of Q2D flow calculated from equation 28. $\mathrm{Pr} = 0.019$, $d = h$.

with d. Thus inertial forces become more important and from equation 19 the interaction parameter is decreased and with it Joule's time-scale (equation 17) is increased. In the same way the diffusion time along the magnetic field plotted in figure 11b (equation 22) is increased at smaller scales. From both effects a significant tendency towards more isotropic flow at smaller scales may be expected. However from equation 20 the viscous decay time decreases with the eddy size and we can expect from the values plotted in figure 10b a dominant influence of viscous forces damping strongly small scale motions.

5   Results

A clear discussion of phenomena is commonly facilitated by keeping all but one characteristic number constant and varying a particular one to evaluate precisely its effect on the flow. In our case it would be desirable to keep the Rayleigh numbers fixed and vary the Chandrasekhar number. However with the used experimental setup the Rayleigh-number itself is obtained as a dependency of the supplied heat flux. To fix the Rayleigh number to a preselected value by varying the applied heat flux is very time consuming because in natural convection the transient effects last very long. Therefore the experiments are performed at fixed heat fluxes, respectively set electrical heating powers. Nevertheless this type of control situation holds for most technical applications where a given amount of heat has to be transported from the heat source to the heat sink. If not mentioned otherwise, experimental results will be presented in non-dimensional form by using the scaling laws introduced in section 2. Occasionally the physical units will be given in the figures.

5.1 General behavior at constant heat flux

From the the discussion of basic phenomena in sections 3.1 and 4.5 it becomes obvious, that the convective flow in the present setup is governed by various counterbalancing effects that are controlled by both the driving force of convection and the magnitude of the applied magnetic field. This may lead to non-systematic behavior of the determined flow quantities like Nusselt numbers or characteristic time-scales when the control parameters Rayleigh and Chandrasekhar numbers are varied. In order to get a first impression of the influence of increasing magnetic field on the flow, a series of experiments $(M0)$ is performed where at a constant heating power of $P = 2400W$, corresponding to a constant heat flux of about $q \approx 2.8W/cm^2$, the magnetic field is systematically increased from hydrodynamic flow $(B_0 = Q = 0)$ up to $B_0 \approx 1.2T$ resulting in $Q = 1.45 \cdot 10^6$. For a detailed listing of the experimental parameters see appendix E. In figure 13a-e relevant integral flow quantities are plotted versus the square root of the Chandrasekhar number. From the measured, time averaged temperature difference across the layer we obtain the Rayleigh numbers (equation 1) plotted in figure 13a. At hydrodynamic conditions $(Q = 0)$ a considerably supercritical value of $Ra \approx 2 \cdot 10^4$ is obtained and one may be shure that a strong, time dependent convective motion exists (see Krishnamurti (1973)). At high Chandrasekhar numbers the Rayleigh number increases up to $Ra \approx 3.24 \cdot 10^4$ but the increase is not monotonous. This latter feature is also observed on the corresponding Nusselt numbers calculated from equation 5 and plotted in figure 13b. Because of the increasing damping effect of the magnetic field at higher Chandrasekhar numbers the Nusselt numbers may be expected also to decrease monotonously from the pure hydrodynamic value to unity $(Nu = 1)$. Thus, decreasing contributions of convective heat transport are indicated until finally at high magnetic field the state of pure heat conduction is reached. First, when a weak magnetic field corresponding to a Chandrasekhar number of $Q^{1/2} \approx 120$ is imposed, the Nusselt number decreases significantly compared to the hydrodynamic value due to Joule's dissipation. But with a further increase of the magnetic field, the Nusselt number starts increasing again to a maximum value, until beyond $Q^{1/2} \approx 300$, it finaly decreases monotonously towards $Nu = 1$. Beyond the value $Q^{1/2} \approx 1200$ the state of pure heat conduction is reached. This result confirms that the onset of convection in a finite layer of fluid is shifted to considerably higher critical Rayleigh numbers. If we interpret the Rayleigh number obtained for the highest Chandrasekhar number as critical Rayleigh number $Ra_c \approx 3.24 \cdot 10^4$, equation 46 gives us a value of the similarity parameter $1/\tau \approx 821$ and from equation 40 we obtain $Q^{1/2} \approx 1291$. This result is in a reasonable agreement with the value predicted by Burr and Müller (1997) plotted in figure 4b.

In figure 13c the mean square (ms) value (see section D) of temperature $\overline{T'^2}$, recorded by one particular thermocouple of the probe in the center, is plotted. From this graph we can estimate the rate of time dependence of the flow. We find similar behavior as for the Nusselt numbers. At an intermediate intensity of the magnetic field, the graph shows a maximum before beyond $Q^{1/2} \approx 650$ stationary flow is indicated by $\overline{T'^2} \approx 0$. We conclude that there exists a stable flow region $650 < Q^{1/2} < 1200$ with a significant convective heat transport by laminar convective motion.

The increase of the convective heat transport at an intermediate intensity of the magnetic field is the most unique feature of this flow problem. However, one might argue that, because the Rayleigh number is not uniform in this experiment, this conclusion might not be valid but, as the Nusselt numbers generally increase with Rayleigh number, the effect
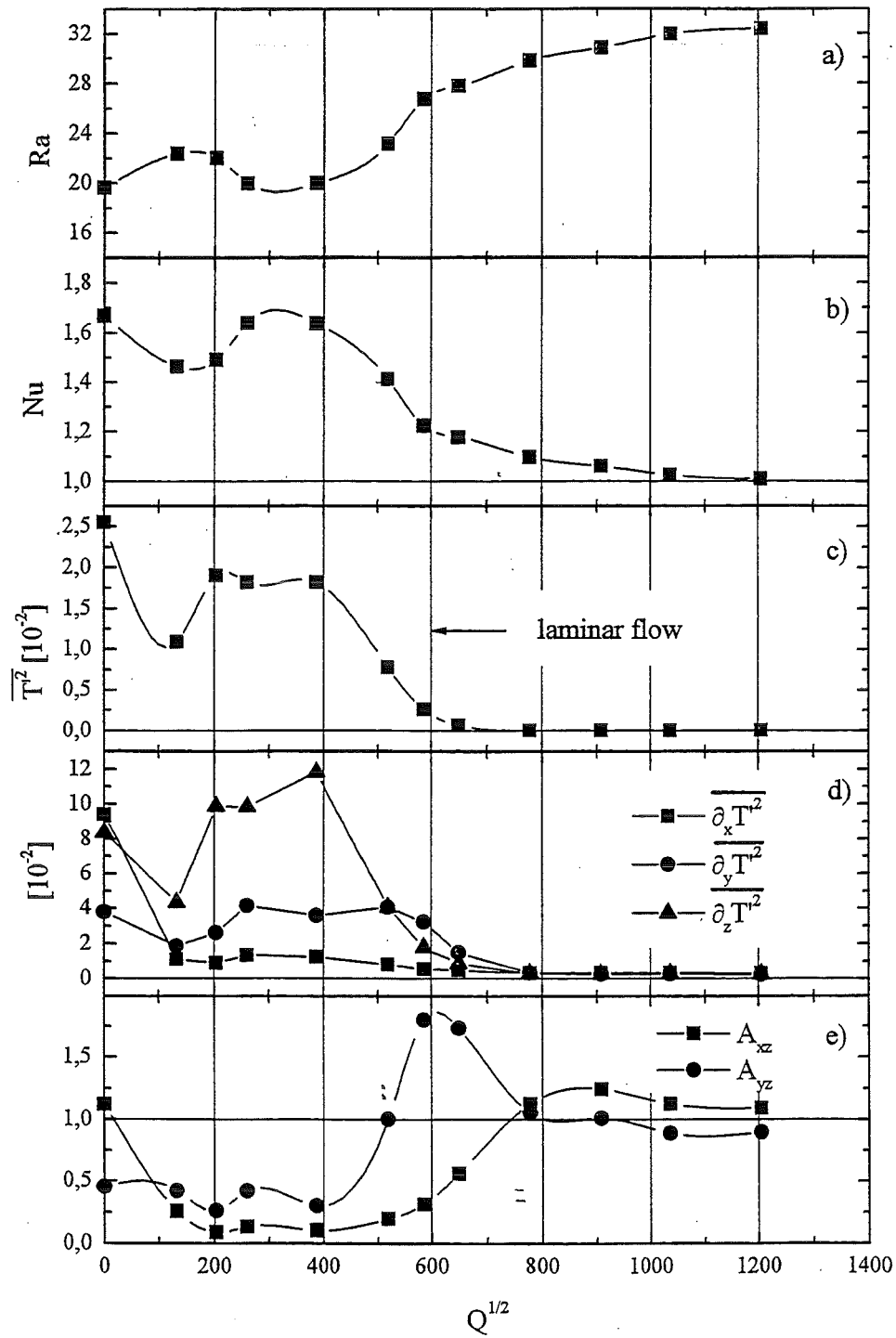
Figure 13: Influence of increasing magnetic field on relevant integral flow quantities at constant heatflux $q = 2.8W/cm^2$, a) Rayleigh numbers Ra. b) Nusselt numbers Nu, c) mean-square (ms) values of the temperature $\overline{T'^2}$ in the fluid measured by the probe, d) ms values of the temperature gradient ∇T measured by the probe $\overline{\partial_x T'^2}$, $\overline{\partial_y T'^2}$ and $\overline{\partial_z T'^2}$ and e) Isotropy coefficients A_{xz} and A_{yz}. The strength of the applied magnetic field is denoted by the square root of the Chandrasekhar number $Q^{1/2}$.

29

would be even more pronounced at constant Rayleigh number.

Next we like to explain that the unsteady behaviour of the Nusselt numbers is caused by significant changes in the flow structure due to the magnetic field. The formation of a flow pattern predominantly orientated in the direction of the magnetic field is demonstrated by utilizing the measured local temperature gradient ∇T in the fluid. In figure 13d the ms values of all three components of the gradient vector, recorded by the probe, are plotted. For purely hydrodynamic flow comparable ms values of the gradients are observed in the two horizontal directions (x and z). In the vertical y-direction the fluctuations of the temperature gradient are much weaker. Under the influence of the magnetic field the values in the directions perpendicular to the magnetic field (y and z) behave similar as the ms value of temperature plotted in figure 13c, but in the x-direction aligned with the magnetic field the ms values of $\partial_x T'$ decay immediately from their very high value at hydrodynamic flow to low values. This holds even for a very weak magnetic field. As in the presence of the magnetic field the spacial derivative of the temperature field disappears, we can conclude from these local measurements that the flow field, at least in the vicinity of the probe, becomes independent from the direction of the magnetic field.

In order to quantify the degree of local isotropy systematically, the two isotropy coefficients

$$A_{xz} = \frac{\overline{\partial_x T'^2}}{\overline{\partial_z T'^2}},$$

(51)

and

$$A_{yz} = \frac{\overline{\partial_y T'^2}}{\overline{\partial_z T'^2}}$$

(52)

are defined. The first coefficient A_{xz} denotes the ratio of fluctuations of the temperature gradient in the direction of the magnetic field to the other horizontal direction and will further be called the horizontal isotropy coefficient. If the time dependent convective flow pattern is three-dimensional and has no preferred orientation in the horizontal (x, z)-plane, the ms-value of the temperature gradient becomes independent of the horizontal directions and, in such case, A_{xz} approaches unity and the flow is called isotropic with regard to the horizontal directions. We may speak of horizontal isotropy. Values of A_{xz} smaller than one indicate horizontal non-isotropy in the sense that the axis of convective rolls become predominantly orientated in the direction of the magnetic field. In the limiting case $A_{xz} \rightarrow 0$ a quasi two-dimensional flow field is indicated. For A_{xz} larger than one convective rolls may be predominantly aligned to the shorter side of the box (see Stork and Müller (1972)).

The second coefficient A_{yz} is calculated as the ratio of ms values in the vertical direction to the horizontal direction perpendicular to the magnetic field. It describes the isotropy properties of the flow in case of quasi two-dimensional flow in the y, z-planes and is therefore called vertical isotropy coefficient. If A_{yz} approaches unity the quasi two-dimensional flow is isotropic with respect to its two-dimensional space. Values smaller than unity are indicating weaker fluctuations in the y -direction, whereas values larger than unity are indicating stronger fluctuations in the horizontal direction. If both coefficients A_{xz} and A_{yz} approach unity the time dependent flow field is isotropic with respect to all three coordinates.

In figure 13e both isotropy coefficients are shown. For hydrodynamic flow the horizontal isotropy coefficient A_{xz} is indicating that the flow is isotropic with respect to the

horizontal directions. Because of the influence of the magnetic field A_{xz} decreases so fast that already at $Q^{1/2} \approx 200$ a minimum value is obtained. Thus, a fast transition from a horizontal isotropic convective flow pattern to a strongly non-isotropic flow pattern of convective rolls predominantly orientated in the direction of the magnetic field is obvious. It has to be mentioned that this non-isotropy obtained from the local measurements of the probe only holds in the vicinity of the probe and does not necessarily indicate Q2D flow in the throughout. However, zero fluctuations may not be obtained from real measurement because there is always a contribution from random noise. Above $Q^{1/2} \approx 500$, A_{xz} increases again with the Chandrasekhar number and finally approaches unity at very high magnetic fields. This indication of higher isotropy with increasing magnetic field is not a real effect. It arrises from the fact that above $Q^{1/2} \approx 500$ the flow becomes stationary and the isotropy coefficients, therefore, describes the ratio of random noise, that in ideal cases results in a value equal to one.

Values of A_{yz} significantly smaller than one in the range $0 < Q^{1/2} < 400$ originate from much weaker fluctuations of the temperature gradient in the vertical direction compared to fluctuations of the horizontal direction perpendicular to the magnetic field. Above $Q \approx 400$ A_{yz} increases steeply until beyond $Q^{1/2} \approx 600$ the influence of noise becomes dominant. The origin of this predominance of horizontal fluctuations at high magnetic fields can not be explained by the current measurements.

The time series of the fluctuating part of the temperature T', recorded by the probe and plotted in figures 14a-h show that the temporal dynamics of the flow are significantly changed with the increasing magnetic field. Without magnetic field ($Q^{1/2} = 0$) the temporal behavior is characterized by fluctuations of random intensity and time-scales typical for turbulent natural convection at high Rayleigh numbers. At MHD flow with $Q^{1/2} = 132$ the amplitude of the fluctuations is significantly decreased but the temporal behavior remains random. If the magnetic field is further increased to $Q^{1/2} = 203$ the fluctuation amplitude increases again and the flow is characterized by a predominant, but significantly faster time-scale. Unless Q2D flow is indicated by the horizontal isotropy coefficent in figure 13e, the temporal dynamics are of random type. However, at $Q^{1/2} = 260$ an intermittent character can be observed. Intervalls of higher order are observed which may be interupted by short time-scale fluctuations of lower order. At $Q^{1/2} = 387$ the flow becomes very well organized. Large amplitude fluctuations of a lower governing frequency are modulated by a second lower frequency. The process that generates this second frequency seems to die off at higher magnetic fields so that at $Q^{1/2} = 519$ only one frequency is observed. In the transition regime to stationary flow beyond $Q^{1/2} \approx 600$ some weak random fluctuations occur until finally at $Q^{1/2} = 1204$ stationary flow is indicated.

In the region of highly organized flow beyond $Q^{1/2} = 260$ the leading time scale of the fluctuations may easily be obtained from the time series but at weaker magnetic fields, where the fluctuations are more random, this is difficult. In order to evaluate the temporal behaviour in this range we first calculate the autocorrelation functions A_k defined from equation 74 (appendix D). In figure 15 the A_k functions are plotted for the same set of parameters as for the time series shown in figure 14. Here the time series with periodic features are clearly identified by pronounced maxima that occur after defined time periods. From the autokorrelation functions the gouverning time-scale is obtained by an integration of A_k from $\underline{t} = 0$ up to the point t_I where A_k first vanishes. The following
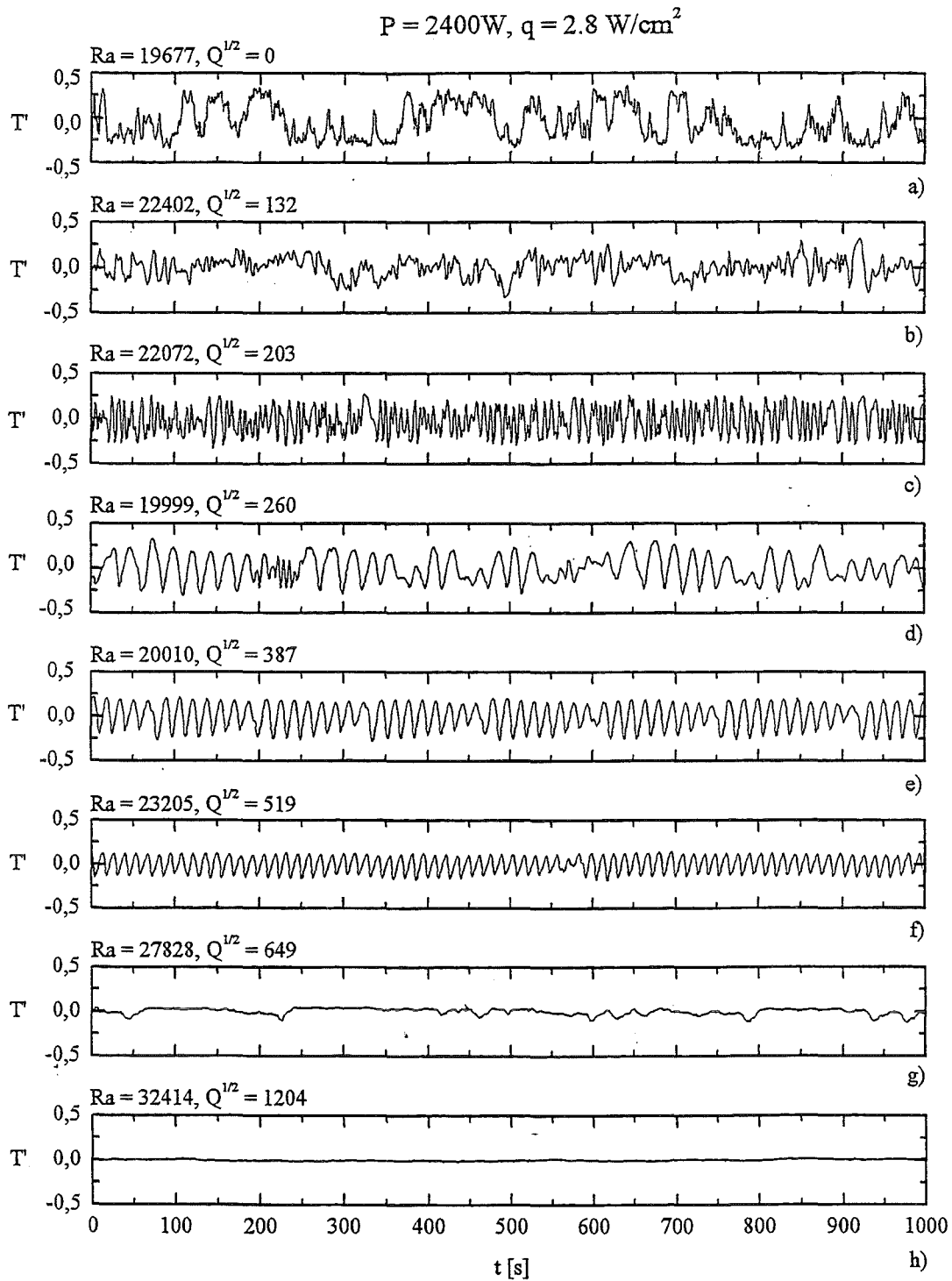
Figure 14: Time series of the fluctuating part of the temperature T' recorded by the probe. At constant heat flux $q = 2.8 W/cm^2$ the magnetic field is increased from hydrodynamic flow ($Q^{1/2} = 0$) to MHD flow at $Q^{1/2} = 1200$.

relation holds:

$$\tau_I = 2\pi \int_0^{t_I} A_k(\underline{t}) d\underline{t}. \tag{53}$$
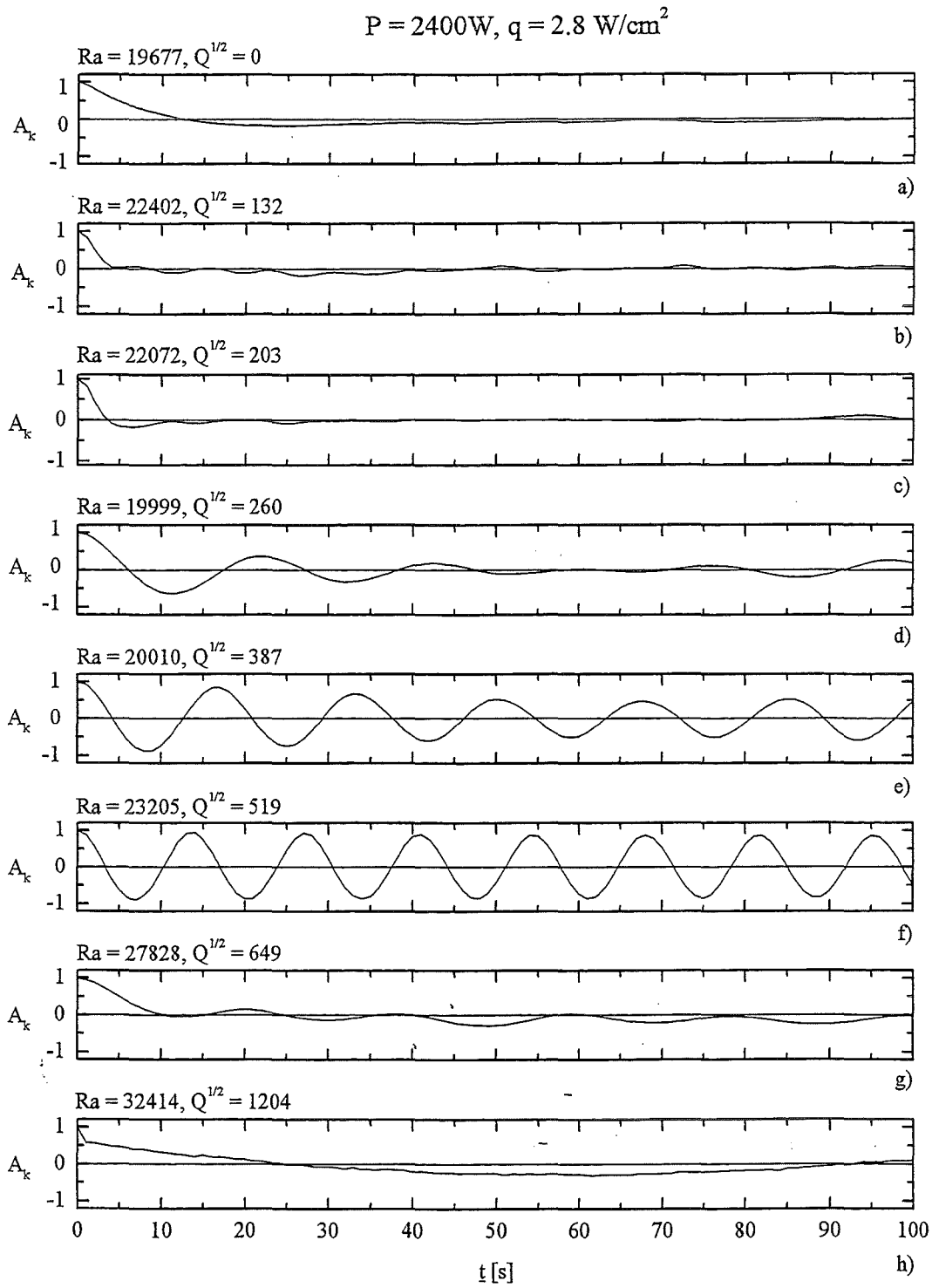
Figure 15: Autocorrelation functions of the time series plotted in figure 14 At constant heat flux $q = 2.8W/cm^2$ the magnetic field is increased from hydrodynamic flow ($Q^{1/2} = 0$) to MHD flow at $Q^{1/2} = 1200$.

τ_I is further called integral time-scale, although the definition is different from the one commonly used in turbulence. In figure 16a the resulting integral time-scales at $q = 2.8W/cm^2$ are plotted as a function of $Q^{1/2}$. The horizontal line corresponds to the thermal diffusion time $t_0 = h^2/\kappa \approx 15.5s$. For hydrodynamic conditions the dynamics
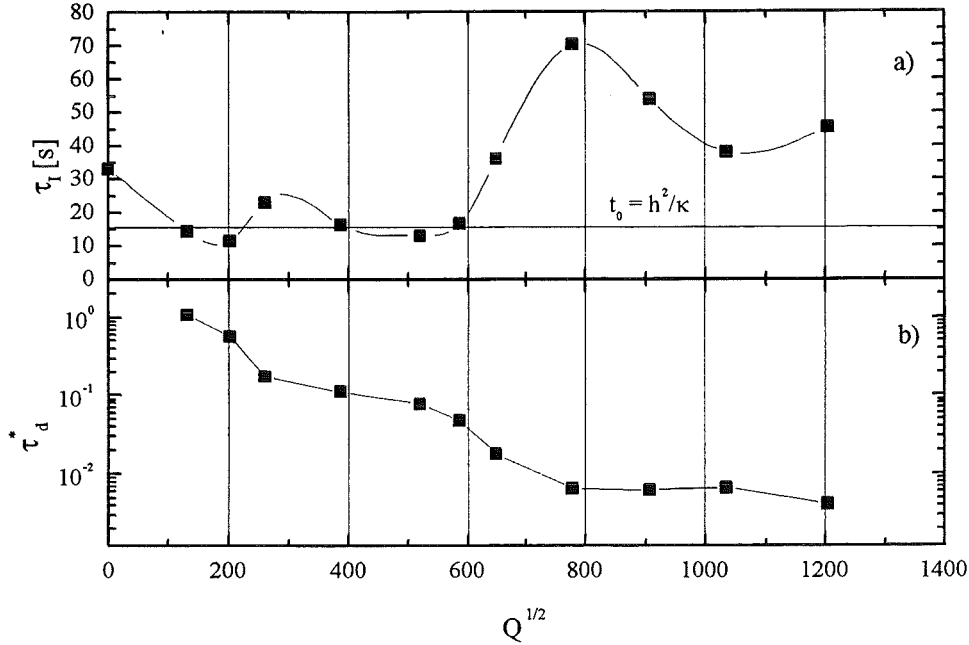
Figure 16: a) Integral timescales τ_I evaluated from autocorrelation functions A_k, compared with the thermal diffusion time and b) non-dimensional diffusion time of angular momentum along the magnetic field τ_D^* obtained by scaling with the integral scale.

of the flow are much slower than the thermal diffusion time. The integral time-scales of MHD flow are significantly smaller, i.e. of the order of the thermal diffusion time, at least in the relevant region of strong time dependent flow below $Q^{1/2} \approx 600$. However, in the transition region from random to organized flow around $Q^{1/2} \approx 260$ the integral scale increases again. Thus, the integral scales represents well the observations made on the time series in figure 14. Above $Q^{1/2} \approx 600$ the integral time-scales increase steeply. However, we have seen from figure 13c that the flow above $Q^{1/2} \approx 600$ is stationary and the obtained values are therefore related to single disturbances in the temperature field or to random noise. Therefore the region above $Q^{1/2} \approx 800$ will be excluded from the further discussion. However in the region of clear time dependent flow a good guess of the governing time-scale is obtained from the thermal diffusion time.

With the integral time-scale we have evaluated a new characteristic parameter for the convective vortex motions and we are now able to replace the buoyant velocity (equation 14) in the definitions of characteristic time-scales and parameters by $v_0 = h/\tau_I$. In figure 16b the non dimensional diffusion time of angular momentum along the magnetic field τ_D, calculated from equation 21, is plotted for an l/d-ratio of 20. Only for the smallest magnetic field $(Q^{1/2} = 132)$ $\tau_D \approx 1$ is obtained. This means, the formation of two-dimensional flow acts on characteristic time-scales of the same order of magnitude as the convective motions. At this low magnetic field we may still expect some three-dimensional flow phenomena; a fact clearly indicated by the horizontal isotropy coefficient A_{xz} plotted in figure 13e. If the magnetic field is further increased, τ_D becomes significantly smaller than one and therefore the diffusion process is so fast that we may conjecture quasi two-dimensional flow at least for the large scale motions. However, if we consider structures

34

of smaller scales e.g. $l/d = 80$ the diffusion time will be increased by one order of magnitude and therefore higher isotropy is expected at least in the small scale fluctuations at moderate Chandrasekhar numbers.

5.2 Integral flow quantities

5.2.1 Heat transfer

In a second series of experiments $(M1)$ the range of Rayleigh numbers $0 < Ra < 10^5$ was covered by electrical heating powers up to $P \approx 10.8kW$. The magnetic field was varied in the range $0 \leq B_0 \leq 0.58T$. Pure hydrodynamic flow $Q = 0$ and MHD flows at four distinct Chandrasekhar numbers $Q = 4.0 \cdot 10^4$, $Q = 1.6 \cdot 10^5$, $Q = 3.6 \cdot 10^5$ and $Q = 6.4 \cdot 10^5$ are realized. For convenience, the intensity of the magnetic field is denoted by the square roots of Chandrasekhar number i.e. $Q^{1/2} = 200$, $Q^{1/2} = 400$, $Q^{1/2} = 600$ and $Q^{1/2} = 800$. For a detailed listing of the parameters see appendix E.

In figure 17a-d the Nusselt numbers of the four MHD flows are plotted versus the Rayleigh number and compared with the Nusselt numbers obtained at OHD flow. The horizontal line $Nu = 1$ denotes the state of pure heat conduction. The onset of convection obtained from linear theory (see Burr and Müller (1997) and section 3.4) is indicated by vertical solid lines. For hydrodynamic flow $(Q = 0)$ the Nusselt number does not approach the value $Nu = 1$ exactly, even at clearly subcritical conditions $(Ra < 1708)$. This obviously erroneous result is likely to be caused by uncertainties in the determination of heat losses. However, it has to be taken into account that the first measuring point $Q = 0$ and $Ra = 1295$ is obtained at a supplied power of $P = 170W$ only and small errors in the determination of heat losses may significantly influence the results. For supercritical values of the Rayleigh number, the Nusselt number increases monotonously to values much higher than one, indicating significant convective heat transport. In figure 17a, a magnetic field corresponding to $Q^{1/2} = 200$ is applied. Similar Nusselt numbers as in case of OHD flow are obtained up to $Ra \approx 10^4$. No observation of a delayed onset of convection due to the effect of Hartmann braking can be made for this parameter value. Above $Ra \approx 10^4$ the slope of the Nusselt number is significantly decreased until the values increase steeply again beyond $Ra \approx 3 \cdot 10^4$. However only beyond $Ra \approx 10^4$ the convective heat transport is diminished compared to OHD flow. For one particular heating power of $P \approx 1800W$ different experiments have lead to three different results (three points around $Ra \approx 17000$). These differences may be attributed to some non specifically identified bifurcation phenomena. Such phenomena become more obvious when the magnetic field is further increased. Therefore, we have to specify more precisly the manner in which the experiments are performed. Using the controlled power supply the electrical power is decreased systematically from $P = 3900W$ to smaller values. The obtained conditions at $P \approx 3900W$ are marked in figures 17a-d by arrows. Higher Rayleigh numbers have to be realized by a non-controlled power supply. Here the electric power is increased from smaller to higher values. For every Chandrasekhar number the magnetic field is regulated to its final value downwards from higher values. For a Chandrasekhar number $Q^{1/2} = 400$ (figure 17b) the onset of convection is shifted to a significantly higher critical Rayleigh number compared to OHD flow, but nevertheless the resolution of the experiment is too poor to confirm exactly the theoretical prediction. Near the onset of convection the slope of the Nusselt number curve is of the same size than the one of OHD flow but
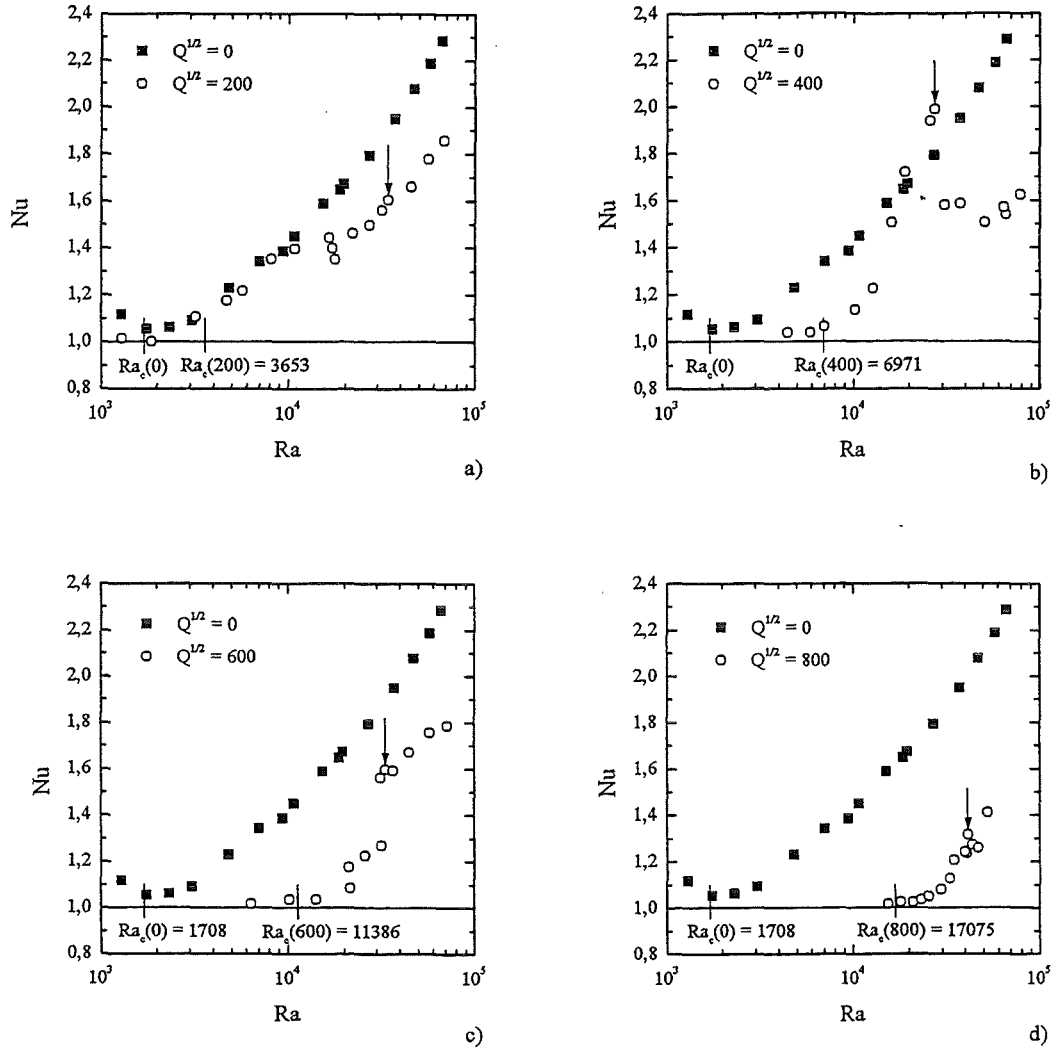
Figure 17: The increase of Nusselt numbers Nu with Rayleigh number Ra for OHD flow $(Q^{1/2} = 0)$ and MHD flow at different Chandrasekhar numbers. The critical Rayleigh numbers for the onset of convection as they are óbtained from linear theory are marked by the vertical lines.

beyond $Ra \approx 1.5 \cdot 10^4$ a steep increase of the Nusselt number occurs and the obtained values even overshoot the values of the hydrodynamic flow with no Joule's dissipation. At $Ra \approx 3.0 \cdot 10^4$ the system changes suddenly to a state with significantly lower convective heat transport. But even for higher Rayleigh numbers the Nusselt numbers are again monotonously increasing. In fact several different heat transfer states have been observed in the intermediate range of Rayleigh numbers for this particular intensity of the magnetic field. These measurements are not all presented in this graph and the subject of multiple bifurcations will be discussed in more detail later. When the magnetic field is increased furtheron to $Q^{1/2} = 600$ (figure 17c) the onset of convection is signifficantly delayed and the experimentally determined critical Rayleigh number is in reasonable agreement with

36

the theoretical value. From the state of pure heat conduction significant convective heat transport sets in at $Ra \approx 2.0 \cdot 10^4$. Beyond $Ra \approx 3.0 \cdot 10^4$ the Nusselt number increases steeply to values comparable to the ones obtained at $Q^{1/2} = 200$ and $Q^{1/2} = 400$. Further, the convective heat transfer above $Ra \approx 5.0 \cdot 10^4$ at $Q^{1/2} = 600$ is significantly higher than the one obtained for the weaker magnetic field resulting in $Q^{1/2} = 400$. For the highest magnetic field corresponding to $Q^{1/2} = 800$ (figure 17d), the observed onset of convection agrees very well with the predicted critical value $Ra_c = 1.7 \cdot 10^4$. The corresponding Nusselt numbers increase monotonously and around $Ra \approx 4 \cdot 10^4$ several bifurcations seems to occur.

Unless the Nusselt numbers behave in a very non-systematic way, there are at least some similarities of the curves obtained at different magnetic fields. At the onset of convection the Nusselt numbers are rising steeply from the level of pure heat conduction. Above certain supercritical values of the Rayleigh number new states of bifurcations occur with different combinations of Rayleigh and Nusselt numbers at the same heat flux. In this region the convective heat transfer may either increase or decrease with increasing heating rates or increasing Rayleigh numbers. At very high supercritical Rayleigh numbers the Nusselt numbers always increase monotonously.

In order to render the obtained results comparable to other experiments or numerical simulations, the Prandtl number evaluated from the thermophysical data has to be known because only at uniform Rayleigh, Chandrasekhar and Prandtl number similarity between two magnetoconvective flows is provided. In figure 18 the Prandtl numbers of all measurements are plotted as a function of Rayleigh number. From a practical point of view, the Prandtl number depends only on the Rayleigh number realized in the experiment. The influence of different Chandrasekhar numbers is not significant.

5.2.2 Onset of time dependent flow and intensity of temperature fluctuations

The evidently non-systematic behavior of the convective heat transfer is likely to be caused by significant changes in the flow structure. In section 5.1, figure 13, the existence of a laminar flow region with significant convective heat transport has been identified by comparing the obtained Nusselt number and the ms value of a temperature signal recorded by the probe. In the same way this matter is displayed for fixed Chandrasekhar numbers in figures 19a-e. Here measurements of $\overline{T'^2}$ (denoted by squares referring to the left axis) are plotted together with the Nusselt numbers (denoted by small circles dots to the right axis) separately for each Chandrasekhar number. Additionally, the onset of stationary convection obtained from linear theory is marked by solid vertical lines. As ms values always suffer from noise the transition point from stable, but noise penetrated flow to real time-dependent flow may only be determined accurately when the level of noise is taken into account simultaneously. Therefore ms values of pure noise, obtained from separate measurements using the isothermal (non-heated) test section are plotted as dashed lines in in the figures. When the noise level is scaled by the temperature difference its normalized value decreases with Rayleigh number as Ra^{-2}. Generally the onset of fluctuations is indicated by the emerging of the scaled measured ms values from the level of noise. If there are additional disturbances arising from the operation of the facility which can not be identified and not taken into account in an error analysis, the measured ms values are higher than the pure noise level even at subcritical conditions. In such cases the measured ms values decrease similarly like the level of noise namely
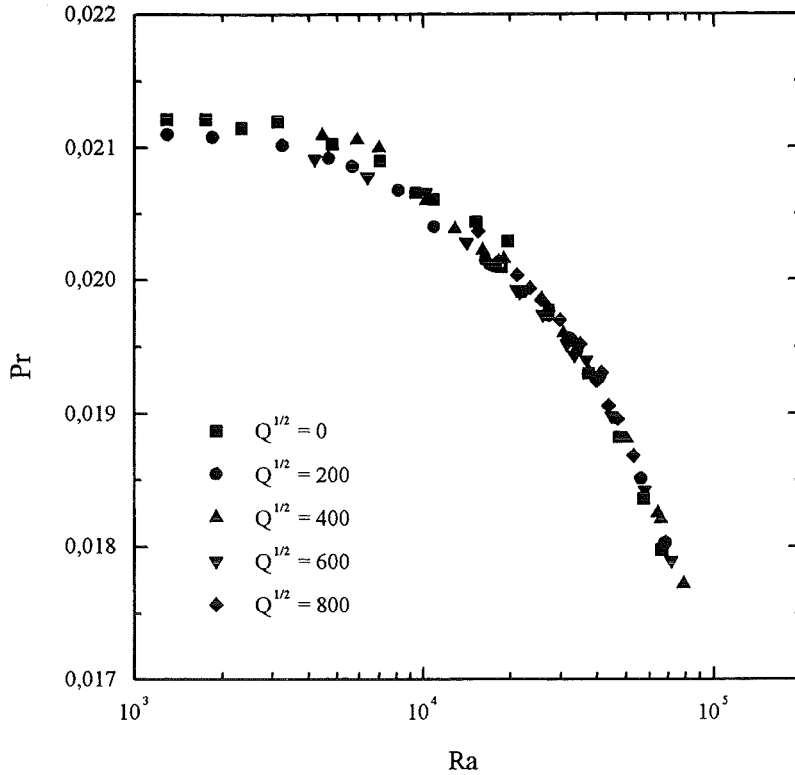
Figure 18: Prandtl numbers Pr derived from the temperature dependent physical properties of $Na^{22}K^{78}$ given in the appendix. Different values are obtained due to changes in the mean temperature of the fluid when different Rayleigh and Chandrasekhar numbers are realized.

like Ra^{-2} but with higher intensity. The critical Rayleigh number Ra_t for the onset of time dependent flow are determined from figures 19a-e as the points where linear fitting curves derived from the ms values at marginal supercritical conditions cross the dashed lines indicating the level of noise. The results are shown in figure 19f as a function of Chandrasekhar number. In figure 19f also the critical Rayleigh numbers for the onset of convection is given as obtained from linear theory. Although only a rough estimate of Ra_t is obtained due to the low resolution of the measurements, a laminar flow region is clearly identified between the onset of convection and the start of a time dependent flow. It is obvious that the laminar range increases with increasing Chandrasekhar number. In some way these results also confirm the predictions for the critical Rayleigh numbers at the onset of convection obtained from linear theory, because the onset of time dependent flow is detected more accurately than an emerging marginal convective heat transport at low supercritical conditions and low Prandtl numbers. It is known from low Prandtl number Bénard convection that steady conditions are only present in narrow regions beyond the onset of convection.

Compared to OHD flow the intensities of the temperature fluctuations of MHD flows are increasing much steeper beyond the onset of fluctuations but reach quickly a saturation level. For $Q^{1/2} = 200$ the saturation level of the ms value of T is maintained even for high Rayleigh numbers. For $Q^{1/2} = 400$ the ms values decrease again for $Ra > 4 \cdot 10^4$. This effect coincides with the deterioration of the convective heat transfer indicated in
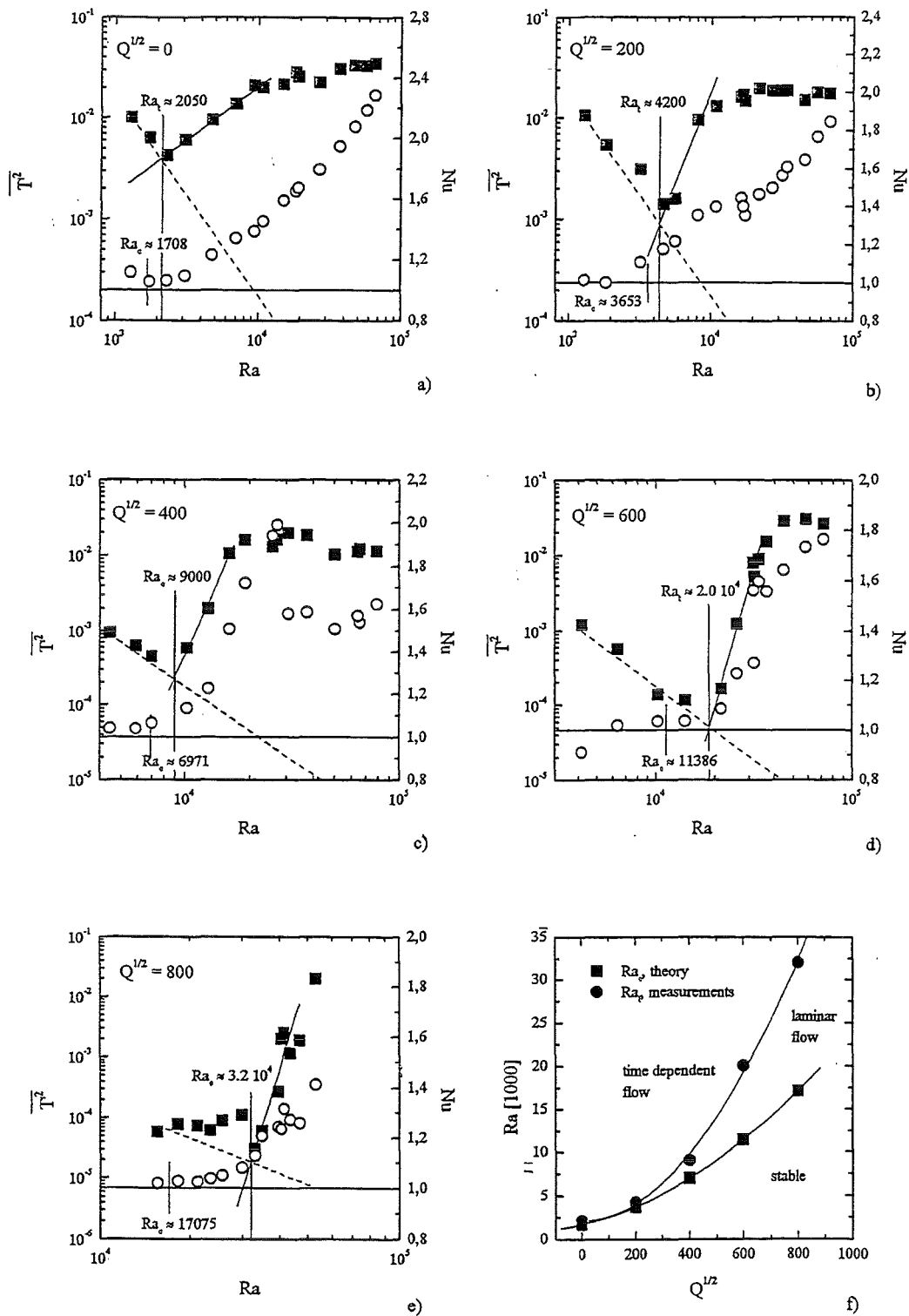
Figure 19: a)-e) mean-square (ms) values of temperature $\overline{T'^2}$ recorded by the probe in the center of the test section (square dots refering to the left axis). The critical Rayleigh number Ra_t for the onset of time dependent flow are determined as the points where the polynominal fitting curves of the ms values cross the dashed lines indicating the level of noise. Circle symbols refer to the right axis and denote Nusselt numbers. The critical Rayleigh numbers Ra_c for the onset of convection, obtained from linear theory are marked by vertical lines. f) Ra_c and Ra_t as a function of $Q^{1/2}$.

the corresponding data plot of the Nusselt number.

In figure 20 the intensities of temperature fluctuations for different magnetic fields are replotted versus the Rayleigh number in one graph. The noise level is indicated by
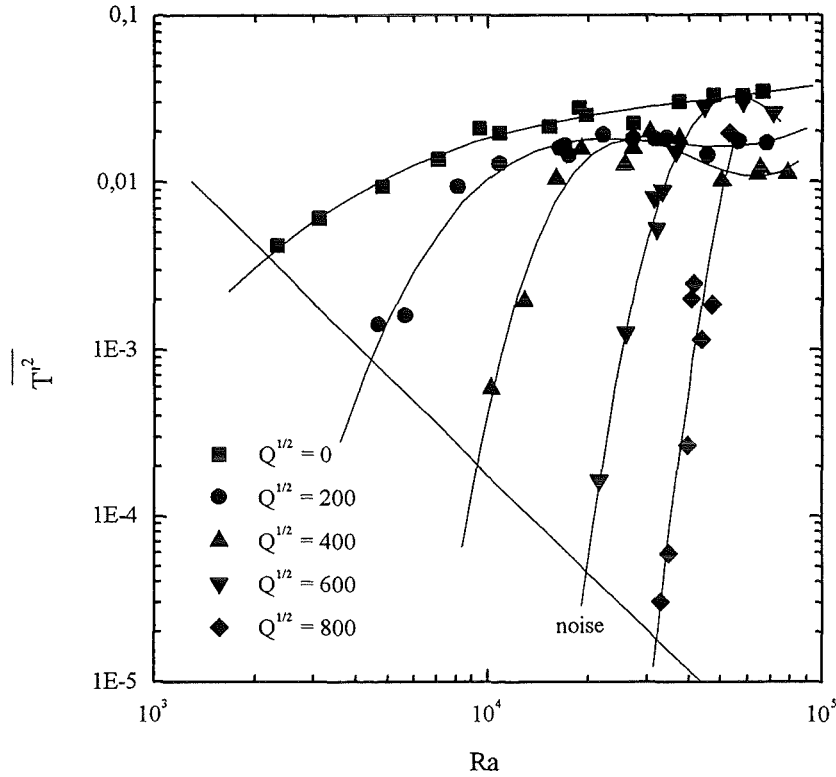
Figure 20: Mean-square (ms) values of temperature $\overline{T'^2}$ recorded by the probe in the center at OHD flow ($Q^{1/2} = 0$) and MHD flow at different Chandrasekhar numbers Q. The level of noise is indicated by the solid line of slope -2. Measurements at clearly stable flow conditions are not plotted.

a solid line. Generally, the ms-values at OHD flow are higher than the ones of MHD flow, at least in the investigated range of Rayleigh numbers. The growth rate of $\overline{T'^2}$ at the beginning of time dependent flow becomes significantly larger for stronger applied magnetic fields. Because of the damping effect of the magnetic field the fluctuation intensities are generally expected to decrease with increasing magnetic fields but in the region of strong time dependent flow ($Ra > 5 \cdot 10^4$) no systematic behavior is observed. The values at $Q^{1/2} = 600$ are overshooting those of lower magnetic fields at $Q^{1/2} = 200$ and $Q^{1/2} = 400$ and reach almost the values of OHD flow. However, the values at $Q^{1/2} = 800$ are lower again but as the saturation level is not reached yet, it may be conjectured that they may achieve a saturation at higher Rayleigh numbers values even above the ones of OHD flow.

5.2.3 Isotropy properties of time dependent flow

The method of determining local isotropy properties from the fluctuations of the local temperature gradient was already outlined in section 5.1. During the measurement one

thermocouple of the probe failed and therefore we lack data of MHD flow for very high Rayleigh numbers. However, for the two smaller Chandrasekhar numbers $Q^{1/2} = 200$ and $Q^{1/2} = 400$ values at supercritical Rayleigh numbers are available and are discussed next.

In figure 21a the horizontal isotropy coefficient A_{xz} defined by equation 51 is plotted versus the reduced Rayleigh number $Ra_r = Ra - Ra_c$ where the critical Rayleigh number for the onset of convection Ra_c is obtained from linear theory (see section 3.4). In figure 21b the vertical isotropy coefficient A_{yz} defined from equation 52 is plotted for the same parameters.
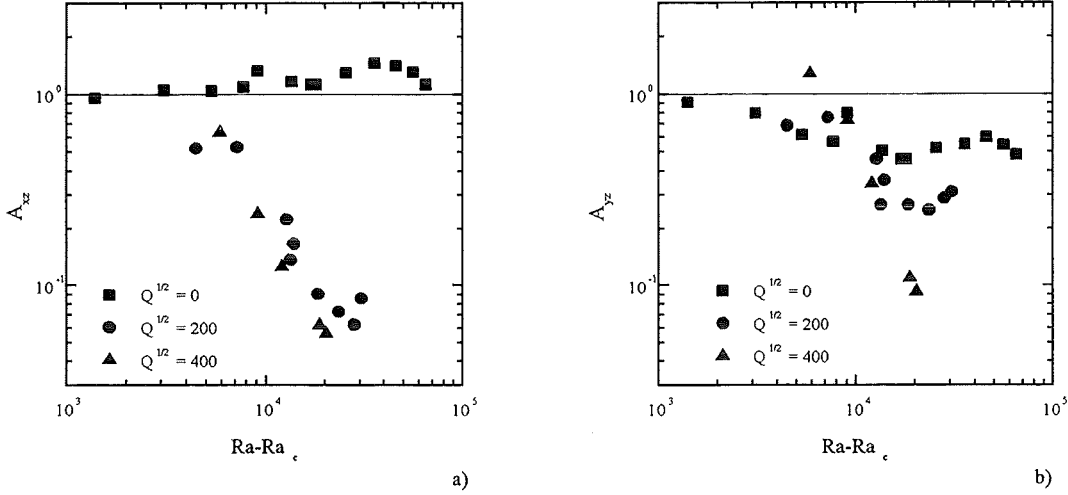
Figure 21: a) Horizontal isotropy coefficent A_{xz} and b) vertical Isotropy coefficient A_{yz} plotted versus the Reduced Rayleigh number Ra_r.

At OHD flow values of the horizontal isotropy coefficient A_{xz} of approximately unity indicate horizontal isotropy of the flow. However, above $Ra_r \approx 10^4$ A_{xz} increases slightly to values larger than one which may indicates a predominant orientation of convective rolls along the shorter side of the box i.e. the z-direction, but the values A_{xz} then return to the value one indicating horizontal isotropy at $Ra_r \approx 8 \cdot 10^4$. The vertical isotropy coefficient A_{yz} decreases with increasing Ra_r at OHD flow and so weaker fluctuations in the vertical direction compared to the horizontal directions are indicated. Similarly like A_{xz} also A_{yz} increases in an intermediate range forming a maximum and then decreases finally. For MHD flow the horizontal isotropy coefficients at slightly supercritical conditions have values around unity. A straight forward interpretation would suggest three-dimensional flow at the onset of convection, but the isotropy coefficients are very sensitive to the effect of random noise. As it was demonstrated in figure 15, both coefficients approach unity when the temperature signals consist of random noise only. In the transition region from laminar to time dependent flow the contribution of noise to the obtained signals is only slowly reduced. This behaviour suggests a transition from horizontal isotropy to strongly non-isotropic flow when the Rayleigh number is increased at slightly subcritical conditions. In contrast to that, we expect from the discussion of time-scales in section 3.1 a higher tendency towards two-dimensional flow. However, when the effect of noise has been overcome at large supercritical Rayleigh numbers a strong non-isotropy of the flow is observed originating from convective rolls aligned with the imposed magnetic field. Simultaneously

41

the vertical isotropy coefficient is decreased for both increasing Rayleigh numbers and increasing Chandrasekhar numbers. Thus at MHD flow significantly lower fluctuations of the temperature gradient in the vertical direction compared to the horizontal direction of the Q2D flow are observed.

5.3 Temporal characteristics of the flow

5.3.1 Time series

A first impression of the structure of the time dependent flow may be obtained from time series of the fluctuating part of the temperature T' recorded by the probe. In figures 22a-h, 23a-h, 24a-h, 25a-h and 26a-h the influence of increasing the Rayleigh number from the subcritical values, denoted by negative reduced Rayleigh numbers $Ra - Ra_c$, up to large supercritical values is demonstrated on selected time series for OHD flow and for four investigated Chandrasekhar numbers.

At OHD flow and for the first two Rayleigh numbers $Ra = 1295$ and $Ra = 1766$ (figures 22a and b) the signals are dominated by the effect of noise (see also figure 19a). This noise level is the result of scaling small fluctuations of the thermo-potential by small temperature differences across the layer. When the Rayleigh number is increased, the intensity of real fluctuations to that of random noise becomes larger and we can observe real temperature fluctuations related to time dependent flow for above $Ra = 3116$. Up to the Rayleigh number $Ra = 9463$ the flow is dominated by variations of the temperature on long time-scales. At higher Rayleigh numbers this time-scale is stil present but additionally fluctuations on significantly smaller time-scales occur. However the OHD flow exhibits always a non-organized chaotic behavior. Periodic flow patterns, as predicted by Clever and Busse (1974), Busse (1978), and Chu and Goldstein (1973), are not observed in our experiment at OHD flow.

When a magnetic field corresponding to $Q^{1/2} = 200$ is applied (figure 23) long period variations of the temperature are observed even at subcritical conditions. We conclude that the layer is not stabilized by the magnetic field. When an obvious time dependent flow sets in at $Ra \approx 8155$ (figure c), a characteristic time-scale is observed, although the flow is not periodic in the sense that only one characteristic frequency occurs. A further increase of the Rayleigh number renders the dynamics of the flow faster and the signals become irregular and similar to those for OHD flow. However compared with OHD flow there is a lack of long time variations especially at high Rayleigh numbers.

At $Q^{1/2} = 400$ (figure 24) the transition process from the state of pure heat conduction to strong convective heat transfer is completely changed by the magnetic field. Temperature fluctuations set in at a well defined frequency and the temperature recordings in figure 24c exhibit almost a sinusoidal shape. If the Rayleigh number is increased furthermore, a second much longer time-scale is observed which generates a sawtooth like modulation of the fluctuations having the primary frequency. However at $Ra = 27625$ (figure 24f) the modulation disappears and only one characteristic frequency is left. When the Rayleigh number is increased above $Ra = 30000$ the high degree of organization is lost and we observe an intermittend and chaotic behaviour of the temperature fluctuations as shown in figures 24g and h. It is worth to mention that the occurrence of non organized flow coincides with the drastic decrease of the Nusselt number for this particular value of the Chandrasekhar number (see figure 17).

42

Figure 22: Time series of the fluctuating part of the temperature T' recorded by the probe for OHD flow at $Q = 0$. The Rayleigh number is increased from the subcritical value $Ra = 1295$ to supercritical values up to $Ra = 66641$.

A similar behavior of the signals is observed for $Q^{1/2} = 600$ (figure 25). Although the intensity of the magnetic field is higher than in the previous case and we would expect therefore an even higher degree of organization, more random disturbances of the periodic flow patterns are observed. The different characteristic fluctuations and oszillations occur at significantly higher values of the Rayleigh number and the governing time-scales are

Figure 23: Time series of the fluctuating part of the temperature T' recorded by the probe. MHD flow at $Q^{1/2} = 200$. The Rayleigh number is increased from the subcritical value $Ra = 3238$ to supercritical values up to $Ra = 68532$.

reduced by the magnetic field. This tendency is maintained when the Chandrasekhar number is further increased to $Q^{1/2} = 800$ (figure 26), however, the region where the dynamics turn into a clearly chaotic state is not reached even for the highest Rayleigh number. Moreover, the signals now even exhibit an intermittent character i.e. there are time intervals in which the governing frequency or the amplitude are drastically changed.

44

Ra = 5892, Ra - Ra_c = -1079 $Q^{1/2} = 400$

T'   a)

Ra = 7022, Ra - Ra_c = 52

T'   b)

Ra = 12879, Ra - Ra_c = 5907

T'   c)

Ra = 16114, Ra - Ra_c = 9142

T'   d)

Ra = 19058, Ra - Ra_c = 12087

T'   e)

Ra = 27625, Ra - Ra_c = 20293

T'   f)

Ra = 30714, Ra - Ra_c = 23743

T'   g)

Ra = 65604, Ra - Ra_c = 58633

T'

0   100   200   300   400   500   600   700   800   900   1000

t [s]   h)
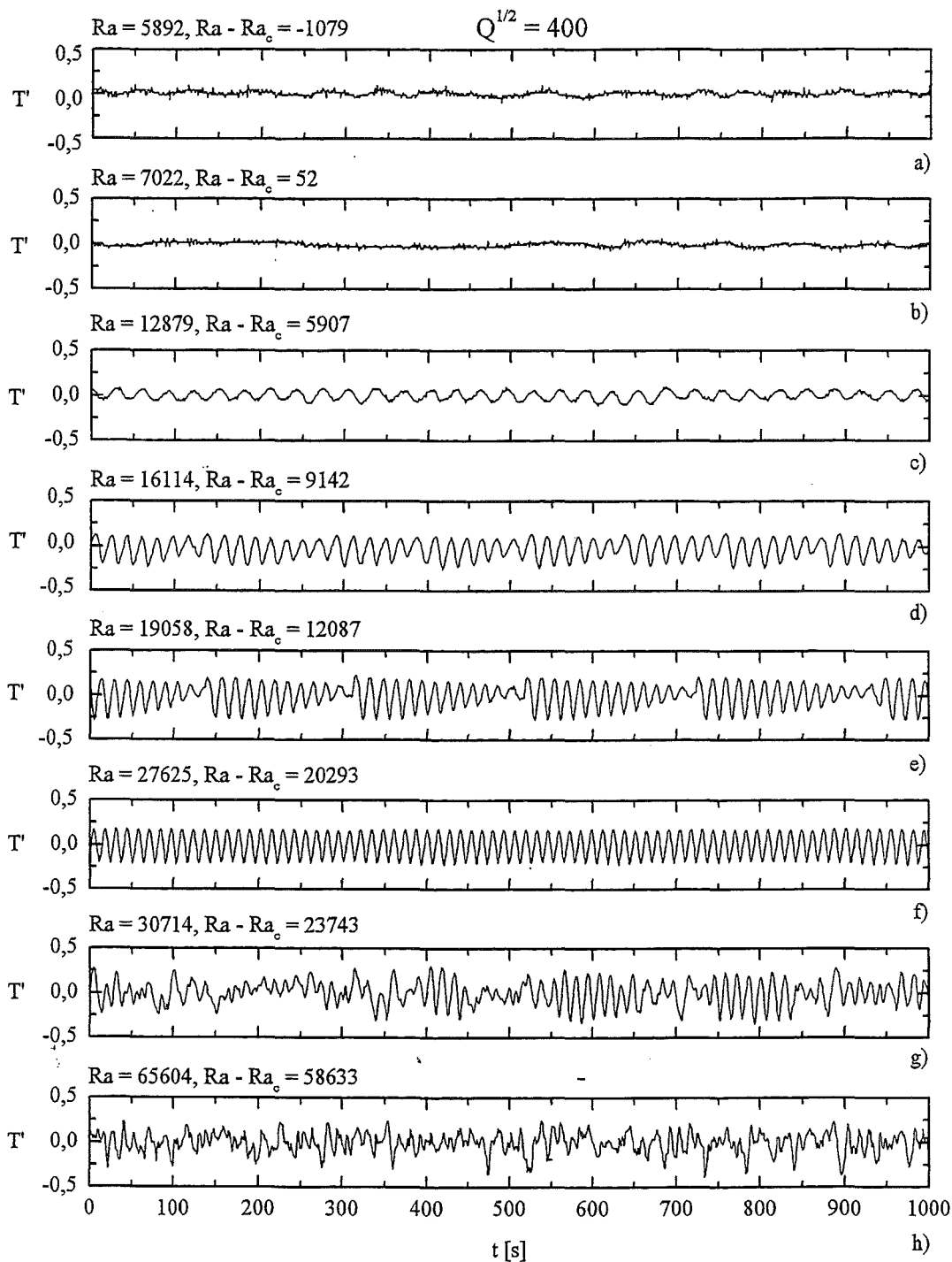
Figure 24: Time series of the fluctuating part of the temperature T' recorded by the probe. MHD flow at $Q^{1/2} = 400$. The Rayleigh number is increased from the subcritical value $Ra = 5892$ to supercritical values up to $Ra = 65604$.

A more objective characterization of the time series is obtained from the integral time-scales τ_I (see equation ??) plotted in figure 27 versus the reduced Rayleigh number $Ra_r = Ra - Ra_c$, in the clearly time dependent range. The left vertical axis denotes non-dimensional time-scales that are obtained from scaling the dimensional time with the thermal diffusion time $t_0 = h^2/\kappa \approx 15.47s$, the dimensional value can be estimated
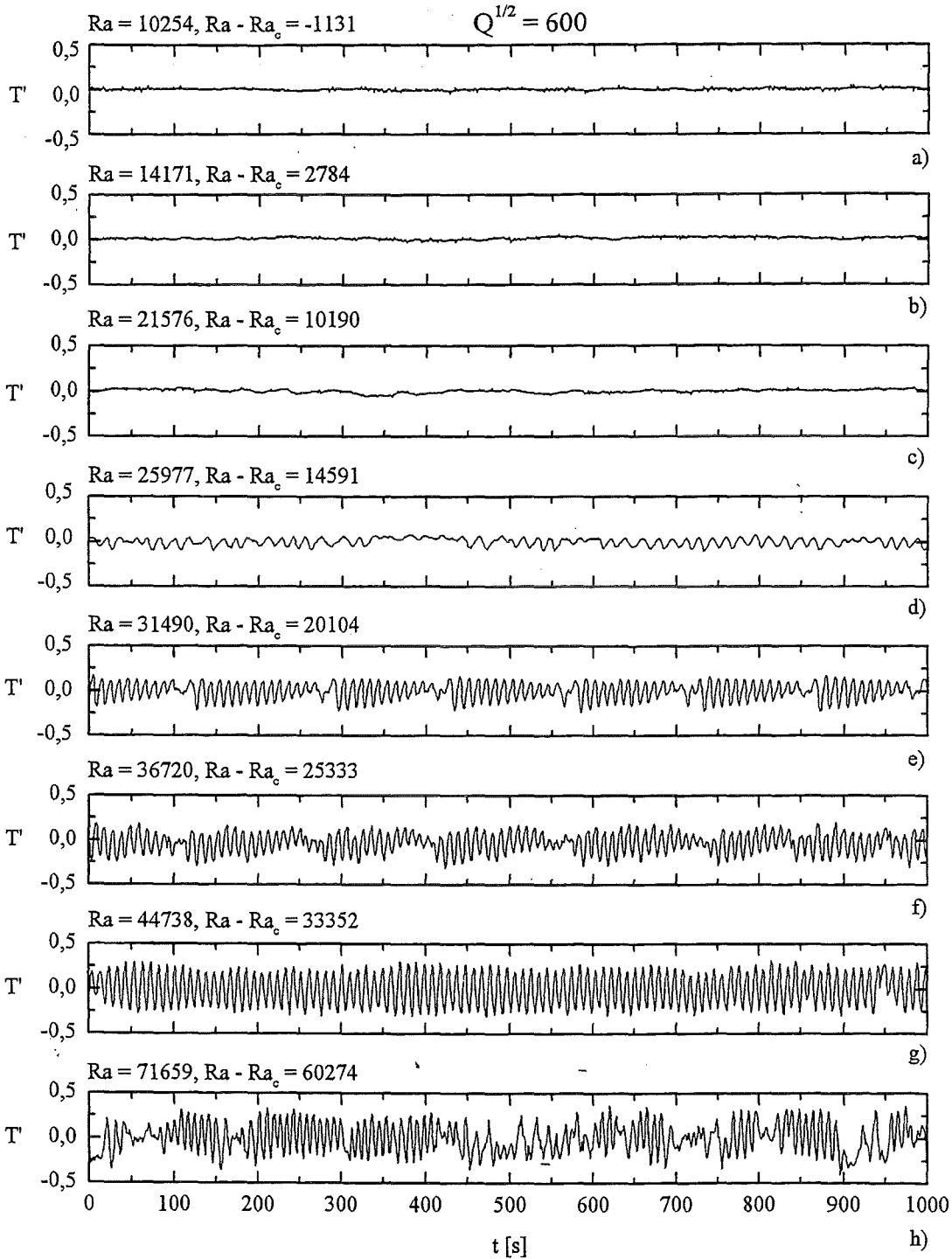
Figure 25: Time series of the fluctuating part of the temperature T' recorded by the probe. MHD flow at $Q^{1/2} = 600$. The Rayleigh number is increased from the subcritical value $Ra = 10254$ to supercritical values up to $Ra = 71659$.

with sufficient accuracy from the right axis. At OHD flow the time-scale of the flow is significantly larger than the thermal diffusion time ($\tau_I > 1$). At slightly supercritical conditions an increase of the Rayleigh number causes a decrease of the integral time-scale indicating faster dynamics of the convective flow. Above $Ra_r \approx 2.5 \cdot 10^4$ this tendency is reversed leading to a minimum value of the integral time-scale at $Ra_r \approx 5.0 \cdot 10^4$. For

46

Ra = 15598, Ra - Ra$_c$ = -1476   Q$^{1/2}$ = 800

0,5

T' 0,0

-0,5
                                                                          a)

Ra = 29853, Ra - Ra$_c$ = 12778

0,5

T' 0,0

-0,5
                                                                          b)

Ra = 32957, Ra - Ra$_c$ = 15882

0,5

T' 0,0

-0,5
                                                                          c)

Ra = 40748, Ra - Ra$_c$ = 23673

0,5

T' 0,0

-0,5
                                                                          d)

Ra = 41418, Ra - Ra$_c$ = 24343

0,5

T' 0,0

-0,5
                                                                          e)

Ra = 43718, Ra - Ra$_c$ = 26643

0,5

T' 0,0

-0,5
                                                                          f)

Ra = 47062, Ra - Ra$_c$ = 29988

0,5

T' 0,0

-0,5
                                                                          g)

Ra = 52994, Ra - Ra$_c$ = 35919

0,5

T' 0,0

-0,5
    0   100   200   300   400   500   600   700   800   900   1000

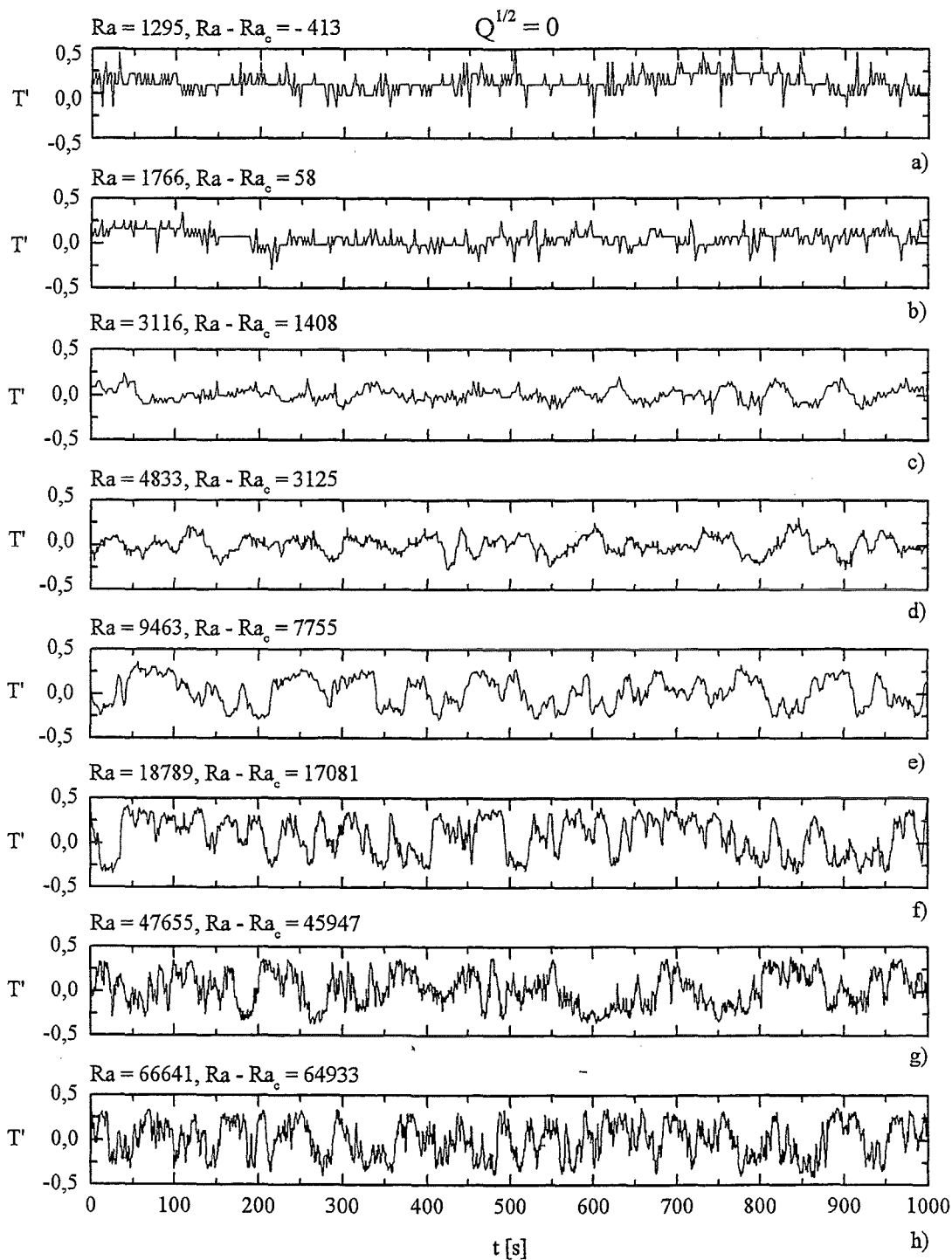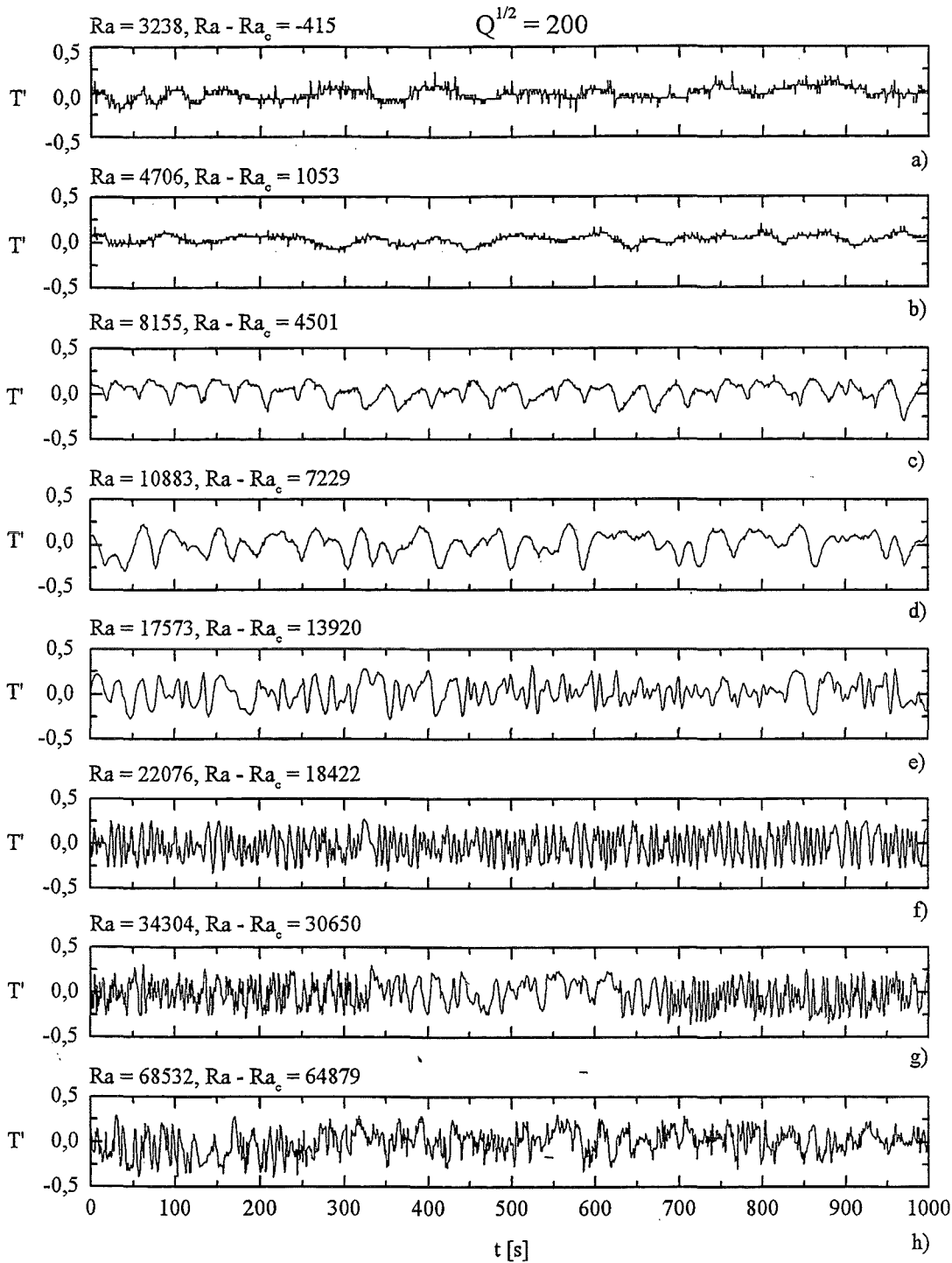   t [s]   h)
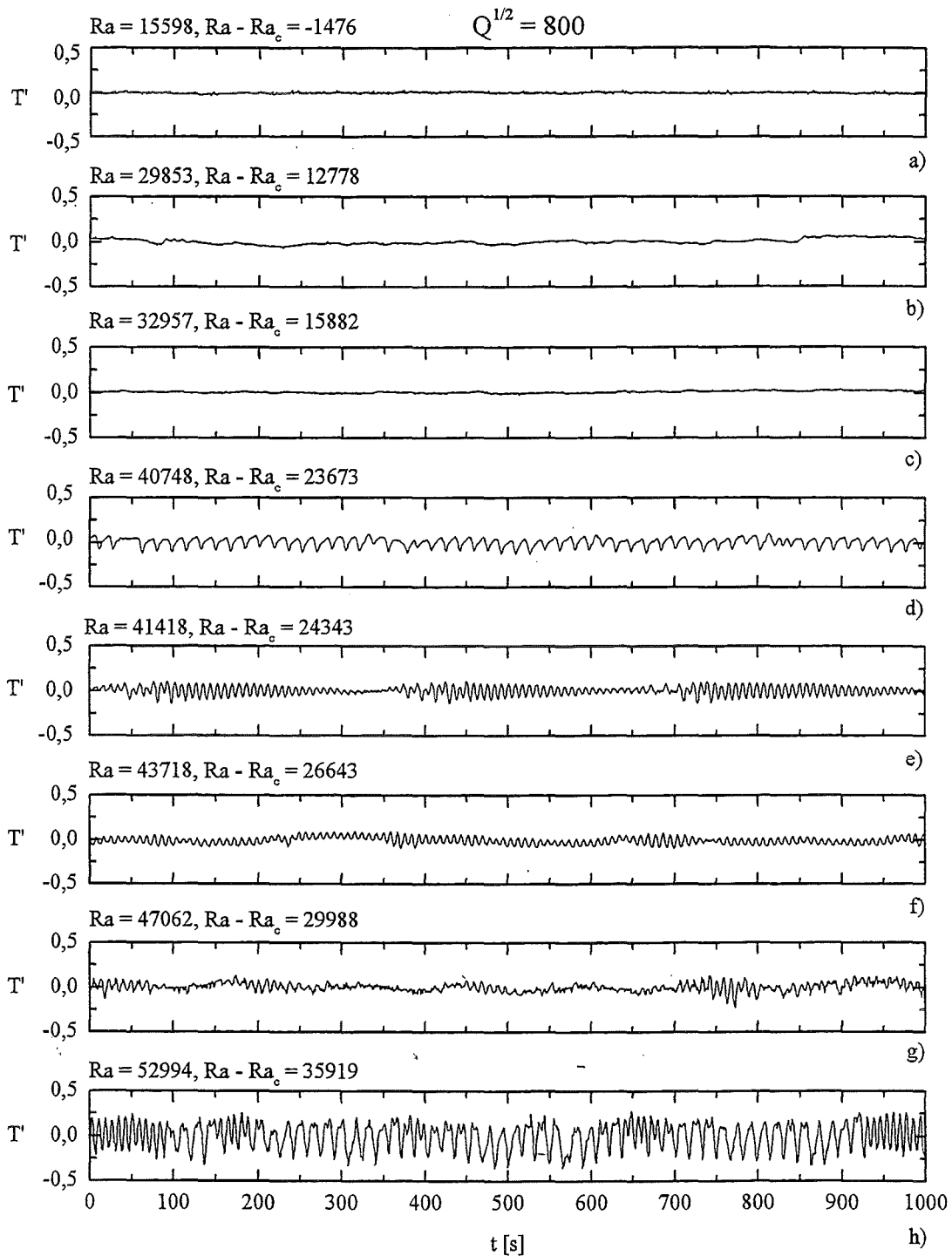
Figure 26: Time series of the fluctuating part of the temperature T' recorded by the probe. MHD flow at $Q^{1/2} = 800$. The Rayleigh number is increased from the subcritical value $Ra = 15598$ to supercritical values up to $Ra = 52994$.

MHD flow at $Q^{1/2} = 200$ similar characteristics are observed at marginally supercritical conditions. However when the Rayleigh number is increased furtheron the integral scale decreases to much smaller values compared to OHD flow. Around $Ra_r \approx 2.5 \cdot 10^4$ a minimum is reached from which the flow evolves into patterns of slower dynamics. Beyond $Ra_r \approx 5.0 \cdot 10^4$ the integral time-scales decreases once more with increasing reduced
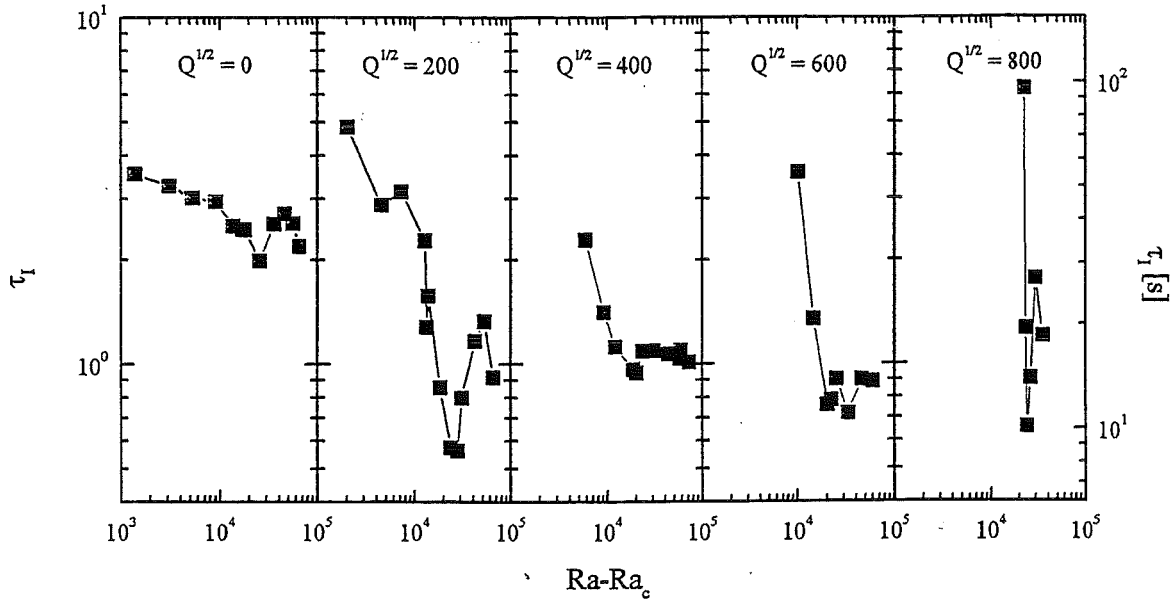
Figure 27: Integral time-scales τ_I at OHD flow ($Q^{1/2} = 0$) and MHD flows at $Q^{1/2} = 200$, 400, 600 and 800. Non-dimensional values are obtained from scaling the integral time-scale with the thermal diffusion time $t_0 = h^2/\kappa \approx 15.47s$ and referd to the left axis. The dimensional values may be estimated with sufficient accuracy from the right axis.

Rayleigh numbers. At stronger magnetic fields i.e. $Q^{1/2} = 400$ and $Q^{1/2} = 600$ the minimum of τ_I is less pronounced but still occurs at $Ra_r \approx 2.5 \cdot 10^4$. Further a plateau is formed at higher Ra_r with almost uniform integral scales. For $Q^{1/2} = 800$ only a narrow band of supercritical conditions is realized, nevertheless a minimum is clearly seen at $Ra_r \approx 2.5 \cdot 10^4$.

Obviously around $Ra_r \approx 2.5 \cdot 10^4$ a significant change in the convective flow pattern occurs for both OHD and MHD flows. It is surprising that for the smallest Chandrasekhar number the fastest dynamics of the flow are observed and, furthermore, that the time series are indicating a much lower degree of organization than for stronger magnetic fields. In order to analyse this phenomenon we evaluate the diffusion time of vorticity along the direction of magnetic field from equation 21 for an l/d-ratio of 20 corresponding to a characteristic length-scale $d = h$ and an N_d based on the characteristic velocity v_0 obtained from the integral scales as $v_0 = h/\tau_I$. In figure 28 the results are shown. All values obtained are smaller than one. From this we conclude that time-dependent three-dimensional disturbances of the velocity field are equalized along the direction of the magnetic field much faster than the governing time-scale of the vortex motion. Thus the flow can be expected to exhibit a strong two-dimensional character i.e. becomes a Q2D flow. However, much faster time-scales as the integral time-scales are evident for example in the time series at $Q^{1/2} = 200$ (see figure 23). For these fluctuations the non-dimensional diffusion times are significantly longer and therefore the flow may exhibit higher isotropy at least at smaller scales.

An other important conclusion may be drawn from the discussion of the diffusion time along the magnetic field. In some time series a saw-toothed modulation of the governing time dependent motion is observed e.g. figure 24e. This modulation frequency is orders of
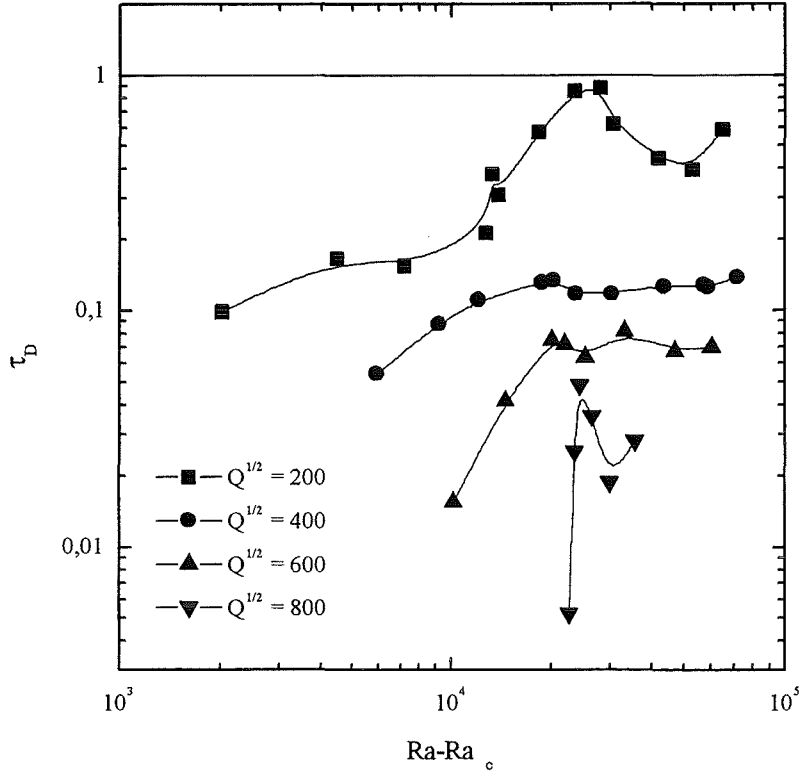
Figure 28: Non-dimensional diffusion time of vorticity along the direction of magnetic field evaluated from equation 21 for an l/d-ratio of 20 corresponding to a characteristic length-scale $d = h$ and with N_d based on the characteristic velocity obtained from the integral scales as $v_0 = h/\tau_I$. Values obtained for different Chandrasekhar numbers are plotted versus the reduced Rayleigh number Ra_r.

magnitude smaller than the governing frequency and therefore the related diffusion time along the magnetic field is even significantly smaller than the values plotted in figure 28. Thus, the modulation of the signals can not be related to some three-dimensional flow phenomena like the propagation of wave-type motion along the magnetic field.

This matter may be investigated furtheron from the comparison of the probe signals T' with the fluctuations of the temperature signals at the lower fluid wall interface described in figure 8. In figures 29a-c time recordings of three selected states of the flow are plotted. The upper parts of the graphs show the measurement of the probe and in the lower part the signals obtained from the three thermocouples $T_{N,b}$, $T_{M,b}$ and $T_{S,b}$ which all are in one line parallel to the magnetic field (see figure 8). For technical reasons, the data had to be recorded in a separate measuring campagne and therefore the signals are not contained in figures 23-26. As the wall thermocouples are embedded in the copper plate at a distance of $e = 1mm$ from the fluid wall interface, their amplitude is significantly reduced compared to the signal taken by the probe in the center of the layer. For a better visualization, the recordings of the north and the south thermocouple $T'_{N,b}$ and $T'_{S,b}$ are shifted by the values given in the diagrams.

In figure 29a the time series of a well organized flow obtained for $Q^{1/2} = 600$ and $Ra = 3.6 \cdot 10^4$ are plotted. The sinusoidal fluctuations of the temperature in the center of
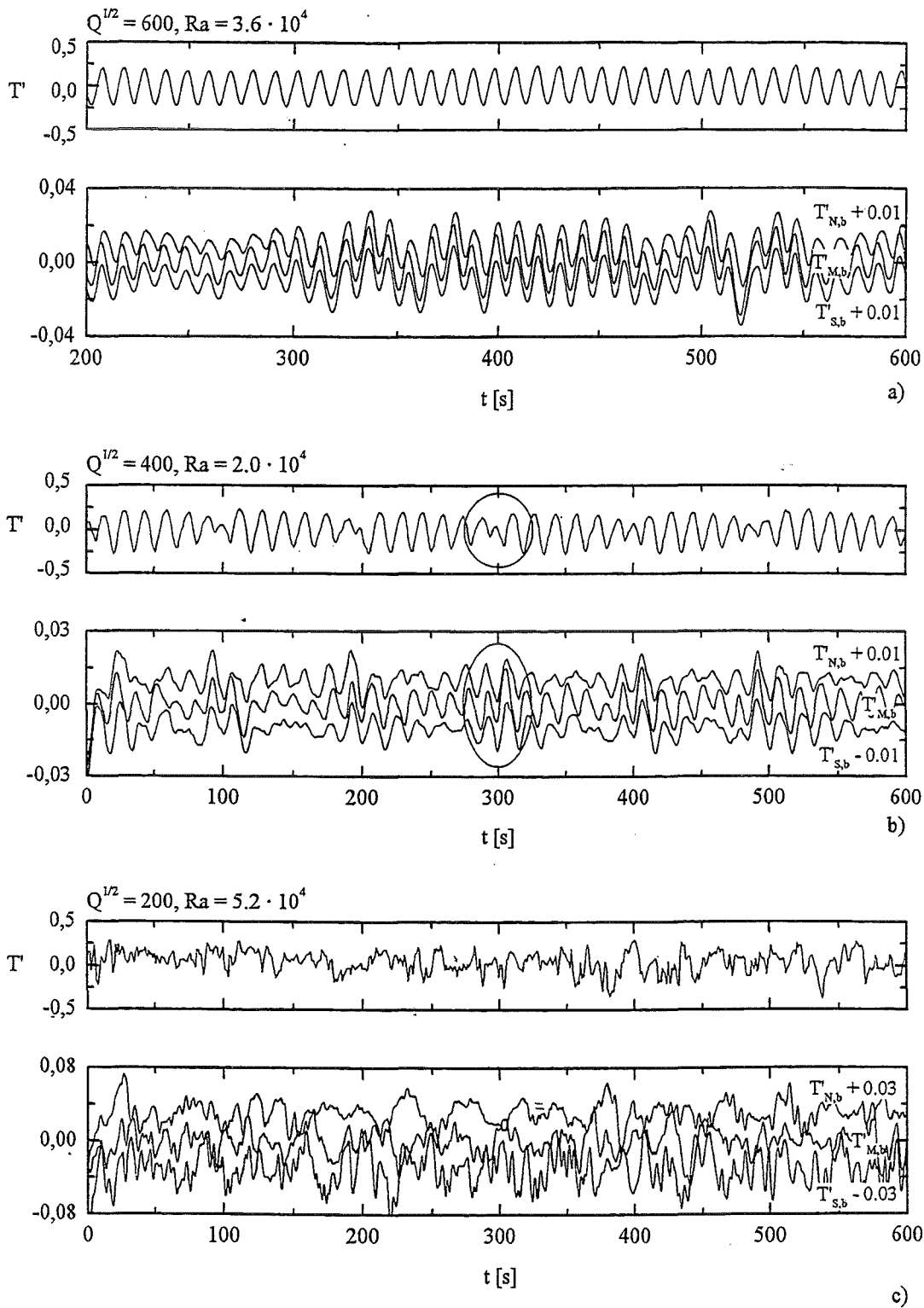
Figure 29: Time series of temperature fluctuations T' for different characteristic flow patterns a, b and c. In the upper graphs the recording of the probe in the middplane is shown. In the lower graphs the fluctuating signals of the three thermocouples $T_{N,b}$, $T_{M,b}$ and $T_{S,b}$ at the bottom wall are shown, which all are in one line parallel to the magnetic field (see figure 8).

the layer recorded by the probe is also clearly visible from the temperature signals recorded by the thermocouples at the fluid wall interface. However, at the thermocouples more disturbances of the organized pattern are observed. It must be mentioned in this context, that the amplitude is smaller by an order of magnitude. It is obvious that all three signals are almost perfectly correlated. Therefore, we conclude from this observation that the fluctuations are caused by a time dependent two dimensional convective roll aligned with the magnetic field which affects all three thermocouples simultaneously.

In figure 29b signals modulated in a saw-tooth shape, obtained for $Q^{1/2} = 400$ and $Ra = 2.0 \cdot 10^4$ are shown. It is observed that the intervalls of reduced fluctuations of the probe signals correspond to intervalls of highly correlated large amplitude fluctuations at the fluid wall interface (see marked region at $t = 300s$). In between these intervalls the signals are much less correlated. From this observation we infer the following scenario for the saw-tooth like signals. If a convective roll starts to form the low initial convective velocity enables the formation of a quasi two-dimensional structure by electromagnetic forces which is low dissipative. Because of the further action of buoyant forces the roll accelerates to a critical turnover velocity at which inertial forces destabilize the two-dimensional motion and three-dimensional disturbances are added to the velocity field which may be imagined as ondulations of a vortex tube around the magnetic field line. Now Joule's dissipation of the fluid motion is drastically increased (see section 3.2) and the convective motion damps out. Out of a nearly stationary flow fluid new Q2D time-dependent structures start up and the process is repeated.

In figure 29c the situation at less organized flow obtained for $Q^{1/2} = 200$ and $Ra = 5.2 \cdot 10^4$ is illustrated. The temperature signals at the wall are in this case uncorrelated especially for the small scale fluctuations. However, for the larger time-scales still some correlation can be found, but the flow in this case is clearly three-dimensional.

5.3.2 Power spectra of temperature fluctuations

A result of the discussion of the ms values obtained from the temperature probe in section 5.2.2 is that time dependent phenomena may be suppressed significantly by increasing the magnetic field. The increase of the critical Rayleigh number for the onset of time dependent flow Ra_t goes along with the increase of the critical Rayleigh number Ra_c for the onset of convection so that there is only a narrow range of convective heat transfer at stationary flow conditions. Figure 20 shows that the damping effect of the magnetic field is not systematic. Although the ms values of temperature at high Rayleigh numbers at MHD flows are all smaller than for OHD flow, the values are not decreasing systematically with the strength of the applied magnetic field. From time series we have already seen that the flow undergoes a transition to higher organized states when the magnetic field is increased. In order to analyse more objectively the composition of the time dependent signals with respect to frequency we calculate the power spectra (see appendix D.3 for definition) of the probe signals. In order to reduce statistical errors, all power spectra $< S >_n$ are calculated as an average of n successive time intervals taken from long time series measurements $(M2)$. For a detailed listing of the parameters see appendix E. In figure 30 the influence of increasing magnetic field intensity on the power spectra at a constant Rayleigh number of $Ra = 5 \cdot 10^4$ is shown. The results are presented in non-dimensional form by scaling temperatures with the temperature difference ΔT across the layer. Non-dimensional frequencies are obtained by using the characteristic frequency
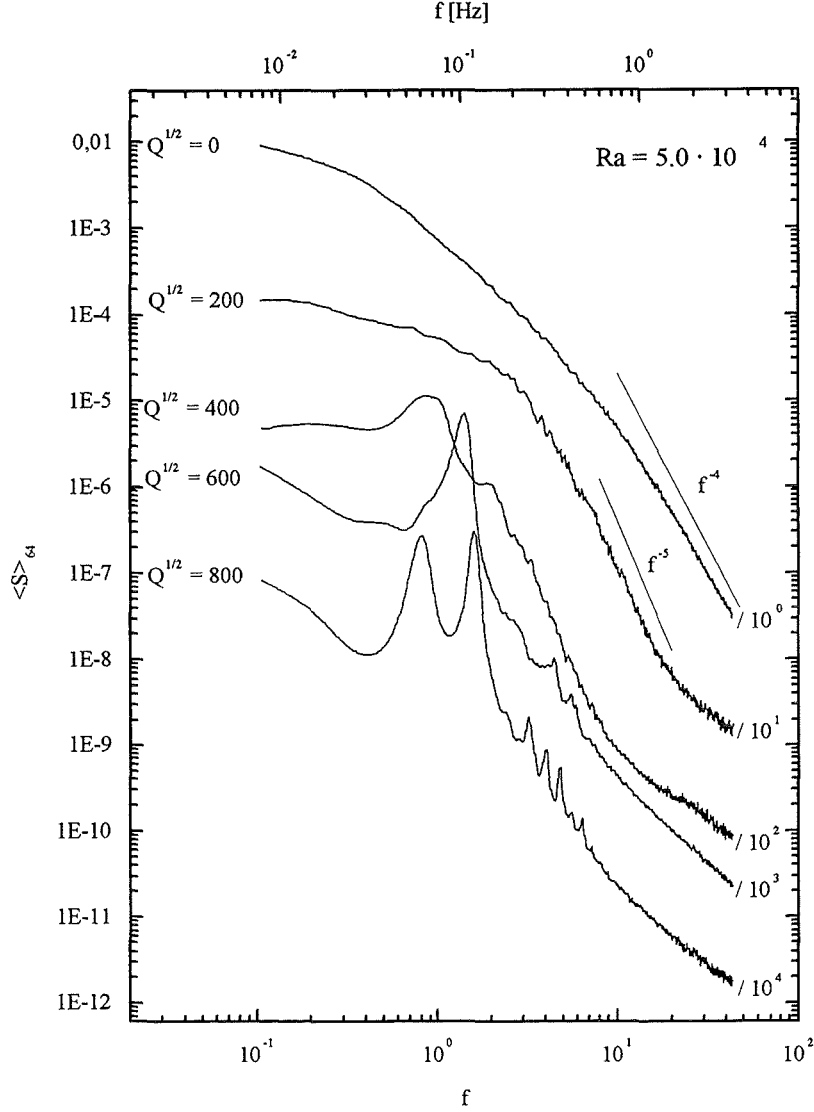
Figure 30: Influence of increasing Chandrasekhar numbers from OHD flow $(Q^{1/2} = 0)$ to MHD flows up to $Q^{1/2} = 800$ on the power spectra $< S >_{64}$ of the temperature signal T' recorded by the probe in the middplane at a constant Rayleigh number $Ra = 5.0 \cdot 10^4$. At Chandrasekhar numbers $Q^{1/2} = 0, 200, 400, 600$ and 800 the Nusselt numbers $Nu = 2.06$, 1.70, 1.45, 1.72 and 1.38 are obtained.

$f_0 = \kappa/h^2$. In order to separate the spectral curves each one is divided by a constant factor given in the figure. The spectrum of OHD flow is calculated as an average of $n = 256$ time intervalls, in case of MHD flow only $n = 64$ time intervalls have been used.

At OHD flow a continuous spectrum with no pronounced frequency is obtained as it is typical for a random signal. In the high frequency range above $f \approx 10$ the energy decays as f^{-4}. This result is not consistent with the predictions of the spectral model of Batchelor (1959) which gives a functional dependence of $S \sim f^{-17/3}$ for low Prandtl number fluids in the inertial-diffusive sub-range of the thermal energy spectrum. However, these predictions are only valid for high Reynolds numbers and isotropic turbulent flow.

If we calculate the Reynolds number from equation 16 we obtain Re ≈ 1580 which is pretty low. Significant energy transfer from large vortices, generated by buoyancy release, to eddies of smaller size can not be expected and Batchelor's model does not apply. Therefore no inertial subrange exists and temperature fluctuations decay predominantly by molecular diffusion. Hinze (1975) (p.294) outlines that in the case of small convective to diffusive transport ratio, the power spectrum of a passive scalar quantity S_T scales as

$$S_T(f,t) = H \cdot \kappa^{-3} \cdot S_v(f,t) \cdot f^{-4}, \tag{54}$$

where H is constant and S_v is the energy spectrum of the velocity field. In a non dissipative, purely convective range of the velocity field S_v can be assumed to be constant and the power spectra of the passive scalar quantity decays on a diffusion process as $S_T(f,t) \sim f^{-4}$. This is in good agreement with our measurements in the frequency range $f > 10$ at OHD flow. If a magnetic field corresponding to $Q^{1/2} = 200$ is applied, the energy spectrum still shows a monotonic decay and from the absence of peaks a random type flow is indicated. However, compared to the energy spectrum of OHD flow the intensity of low frequency contributions is reduced and the slope in the high frequency range is decreased to $S_T \sim f^{-5}$. This indicates a concentration of the fluctuation energy to the intermediate frequency range $1 < f < 10$. Comparing this result with equation 54 we may conclude that in case of MHD flow an additional decay of the velocity spectrum S_v in the convective range as a power f^{-1} occurs. However, additional velocity measurements are necessary to support this conjecture.

If the magnetic field is increased further to $Q^{1/2} = 400$ a hump appears at $f \approx 0.9$. Beyond this value the energy spectrum decays rapidly to a noise dominated level. We conclude that the flow pattern becomes organized with most of the spectral energy concentrated in the frequency range around the hump; high frequency contributions become less important. With a further increase of the magnetic field to $Q^{1/2} = 600$ the hump develops to a peak and the frequency corresponding to the peak is shifted to the higher value $f \approx 1.5$. At $Q^{1/2} = 800$ the energy spectrum is characterized by two pronounced peaks and some others of lower intensity. The governing frequency of the second peak f_2 has approximately twice the value of the first peak with $f_1 \approx 0.83$.

In these experiments, the Nusselt numbers $Nu = 2.06, 1.70, 1.45, 1.72$ and 1.38 are obtained for Chandrasekhar numbers $Q^{1/2} = 0, 200, 400, 600$ and 800. For pure OHD flow the highest convective heat transport is found. Because of Joule's dissipation the Nusselt number decreases when a magnetic field corresponding to $Q^{1/2} = 200$ and $Q^{1/2} = 400$ is applied. Although Joule's dissipation of Q2D flow increases further, for $Q^{1/2} = 600$ a higher Nusselt number than for the weaker magnetic fields is obtained because the well structured flow at this particular Chandrasekhar number seems to result in a minimum of Joule's and viscous dissipation. For $Q^{1/2} = 800$ the Nusselt number is decreased again. The increased Joule's dissipation now is not further balanced by a decrease of viscous dissipation.

In appendix D.3 it is outlined that the total intensity of fluctuations, i.e. the mean square value, can be evaluated from the sum of all contributions to the energy spectrum S_n (equation 76). Limiting the summation to a distinct value of n we obtain a ms value that is related to fluctuations at a frequency f_n and frequencies below

$$E_n = \frac{1}{E_{n \to \infty}} \sum_1^n S_n. \tag{55}$$
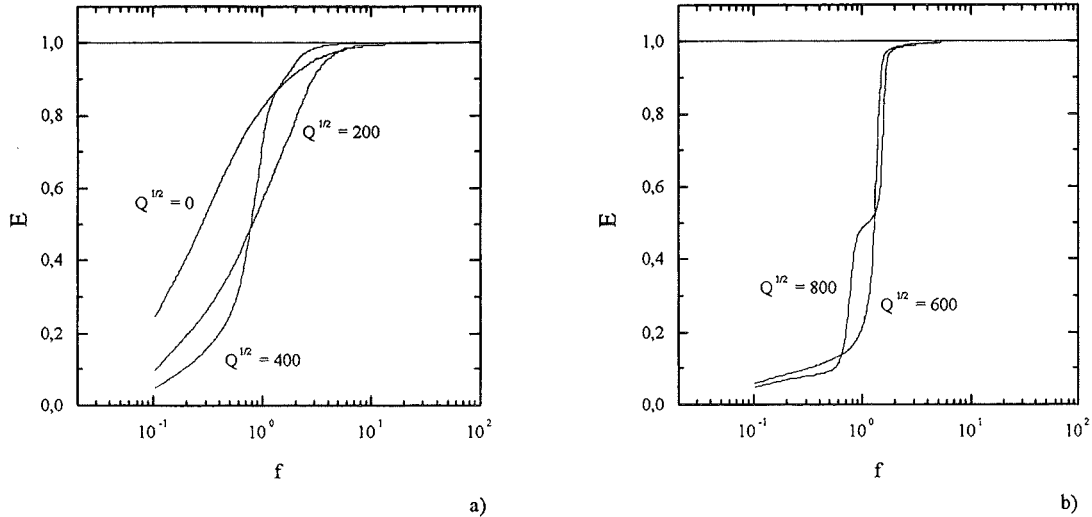
Figure 31: Influence of increasing Chandrasekhar numbers Q on the integrated power spectra defined from equation 55 at constant Rayleigh number $Ra = 5.0 \cdot 10^4$. a) hydrodynamic flow at $Q^{1/2} = 0$ and MHD flows at $Q^{1/2} = 200$ and $Q^{1/2} = 400$. b) MHD flows at $Q^{1/2} = 600$ and $Q^{1/2} = 800$.

Scaling with the over all ms-value $\overline{\Phi'^2} = E_{n \to \infty}$, obtained as n approaches infinity, the values tend to unity when all relevant frequencies of the signal have been taken into account. The functional increase of E_n with frequency is called the integrated power spectra $E(f)$. From the integrated power spectra we can estimate the importance of distinct frequency ranges for the obtained intensities of the temperature fluctuations. In figures 31a and b the integrated power spectra are plotted, evaluated from the power spectra in figure 30. At OHD flow ($Q^{1/2} = 0$ figure 31a) E increases strongly already in the low frequency range. The saturation level, defined as $E \geqq 0.98$ is reached for $f \approx 5.3$. For MHD flow at $Q^{1/2} = 200$ low frequency fluctuations are less important. The integrated power spectra increases strongly only for frequencies beyond $f \approx 0.4$ and the saturation level is reached at a comparable value of $f \approx 5.6$. This means that about 80% of the total energy is contained in the frequency range $0.4 < f < 5.6$. At $Q^{1/2} = 400$ a significant increase of E is found at even higher frequencies, but nevertheless, the saturation level is observeded at a significantly lower frequency $f \approx 2.8$. This concentration of fluctuating energy to a more and more narrow frequency range is caused by the increasing organization of the flow into a regular time dependent motion at one governing frequency. In figure 31b the integrated power spectra of the well organized flows at higher magnetic fields are plotted. At $Q^{1/2} = 600$ one governing frequency can be detected from the power spectrum. The integrated power spectra increases above $f \approx 1$ steeply until already at $f \approx 2$ the saturation level is reached. Thus time scales faster than half the thermal diffusion time do not occur in the fluctuating part of the temperature signal. The lower value of the discret frequency at $Q^{1/2} = 800$ causes the integrated power spectra to increase already at smaller frequencies. At $f \approx 1$ a small plateau value of $E \approx 0.5$ is reached from which the values increase furtheron to the saturation level feed by the contributions of the second discrete frequency. We can conclude that the fluctuation energy is about evenly distributed between the two governing frequencies.

From the power spectra and the integrated power spectra we find that if a horizontal magnetic field is applied to a turbulent convective flow at large Rayleigh number the time dependent flow gets more and more organized with the consequence that the fluctuating energy becomes increasingly concentrated to narrow frequency ranges. The governing time scale of the fluctuations in this range is close to the thermal diffusion time of the liquid. In the limiting case of strong magnetic fields the flow can be dominated by one frequency and its harmonics only, exhibiting no longer a turbulent behavior.

6   Conclusions

This report presents an experimental study of the influence of a horizontal magnetic field on liquid metal Rayleigh-Bénard convection. The test section is an electrically heated rectangular box of large aspect ratio 20 : 10 : 1 which is designed to cover the range of high heat fluxes which occur in technical applications like fusion blankets and material processing. The two major control parameters of the flow are the Rayleigh number Ra which expresses in non-dimensional form the temperature difference across the layer and the Chandrasekhar number Q which characterizes the magnitude of the applied magnetic field. In this experiment the range of parameters $0 < Ra < 10^5$ and $0 < Q < 1.44 \cdot 10^6$ is covered. The physical properties of the test fluid sodium potassium $Na^{22}K^{78}$ result in a very small Prandtl number ($0.017 < Pr < 0.021$) and therefore, the nonlinear inertial forces are important in the momentum balance of the flow.

The time averaged temperatures at the upper and the lower boundary are measured by five thermocouples within each confining copper wall. From the temperature difference across the layer and the known imposed heat flux, the integral heat transfer is characterized by calculating the Nusselt number Nu.

Local, time dependent temperature signals are evaluated from a four-element temperature probe placed in the middle of the liquid metal layer. The non-coplanar arrangement of the thermocouples enables the evaluation of the local time-dependent temperature gradient which allows to estimate local isotropy properties of the time dependent flow.

The discussion of characteristic time-scales, that hold for different flow phenomena, shows that in the covered parameter range the equalization of differences in the velocity distribution by electromagnetic forces along the magnetic field lines is much faster than the expected temporal dynamics of the convective motions. This leads to the formation of a strongly non-isotropic flow pattern characterized by convective rolls predominantly aligned with the direction of the applied magnetic field. In the limiting case of strong magnetic fields any differences in the velocity distribution along the direction of the magnetic field lines are removed and a pure two-dimensional flow in the plane perpendicular to the magnetic field is established where electromagnetic forces disappear. However, in closed cavities pure two-dimensional flow is not consistent with boundary conditions. The two-dimensional flow pattern in the core region matches the non-slip condition at vertical Hartmann walls perpendicular to the magnetic field by the formation of thin Hartmann layers. In such quasi two-dimensional (Q2D) flows the Hartmann layers and, provided they are electrically conducting, the Hartmann walls offer a closure path for the electric currents induced in the core region and Joule's dissipation enters the problem. From an analytical integration along magnetic field lines the flow in the core region may be expressed by two-dimensional equations where the damping effect of the magnetic field is expressed

by a similarity parameter $1/\tau$ that depends on the magnitude of the applied magnetic field, the distance between the Hartmann walls and their electrical conductivity. In the experimental setup Joule's dissipation of Q2D flow is small compared to Joule's dissipation of isotropic flow. Therefore strong convective motions can be obtained from the formation of non-isotropic flow even though a strong magnetic field is present. Moreover, in Q2D flows the cascading process of vortices towards smaller scales is inhibited and therefore viscous dissipation is reduced. From these facts it is expected that in the presence of a defined magnetic field the heat transfer across the layer may even be enhanced compared to ordinary hydrodynamic flow.

From the experimentally obtained Nusselt number graphs it is demonstrated, that the onset of convection in a finite layer of fluid is shifted to higher critical Rayleigh numbers when the magnetic field is increased. The obtained values are in reasonable agreement with predictions based on a linear stability analysis of the basic equations of Q2D flow.

If the Rayleigh number is increased beyond critical conditions, the Nusselt numbers at MHD flow increase first monotonously. At high supercritical Rayleigh numbers bifurcations of the flow occur and the experimentally obtained Nusselt numbers behave therefore in a rather non-systematic way. However, there are cases where, at the same Rayleigh number, MHD flow provides a higher convective heat transfer than OHD flow; but for most parameters the Nusselt numbers for MHD flow are smaller than for OHD flow.

Above the onset of convection there is for MHD flow a significant range of stationary convection. Beyond a second critical Rayleigh number time dependent flow sets in. At OHD flow the intensity of temperature fluctuations increases slowly with the Rayleigh number and reaches a saturation level beyond $Ra \approx 5 \cdot 10^4$. Beyond the delayed onset of time dependent flow the intensities of MHD flows are rapidly increasing and reach their saturation level which is always slightly lower than the one of OHD flow but is not systematically decreased with increasing magnetic field intensity. At high supercritical conditions the electromagnetic forces cause a transition of the time dependent flow from a state of turbulent convection, as it is observed for OHD flow, into an increasingly organized Q2D state where the temporal dynamics become dominated by few governing frequencies only. Compared to OHD flow the integral time-scale of MHD flow is observed to be significantly shorter. It reaches values of approximately the thermal diffusion time of the liquid metal layer. In contrary to the continous energy spectrum of OHD flow, most of the fluctuating energy under MHD conditions is concentrated in a narrow range around one governing frequency.

The probe measurements confirme, that the time dependent flow exhibits localy a strong non-isotropic character as the convective structures are aligned with the magnetic field. This tendency for the flow is confirmed by local temperature measurements using thermocouples fixed at the lower fluid wall interface where three thermocouples are arranged in a line parallel to the magnetic field. At high magnetic field, a high correlation of the temperature recordings indicates that convective rolls extend along the whole test section. At weaker magnetic fields correspondingly at higher Rayleigh numbers less correlated signals indicate a higher degree of horizontal isotropy.

Finally the question is raised what benefit can be taken from the use of a horizontal magnetic field in technical applications: In material processing, convective motions may be significantly influenced by a strong horizontal magnetic field due to the effect of Hartmann braking. Thus controlled homogeneous conditions may be provided at a solidification front. The existence of a laminar flow region may give the benefit of convective mixing

of a melt combined with stationary flow conditions at the solidification front. If higher convective transport is desired large amplitude fluctuations at one or more governing frequencies have to be accepted but nevertheless higher quality material may be generated when these fluctuations do not deteriorate the solidified material.

In the thermo-hydraulic design of heat transfer units such as fusion blankets the magnitude of the damping effect of the magnetic field has to be taken into account. If a formation of Q2D flow can be expected, an estimate of the damping effect of the magnetic field may be obtained from the magnetic damping parameter $1/\tau$. A conservative approach certainly is the assumption of pure heat conduction in the blanket. However doing so the problem of tritium transport is aggrivated. If the heat transfer can be described by numerical solution of the equations of Q2D flow, an additional transport equation for the concentration of tritium can give an estimate of the tritium content in the blanket. Therefore, the obtained results can be used as a first data basis for the development and validation of a computer code.

References

Barleon, L., Mack, K.-J. and Stieglitz, R.: 1996, The MEKKA-facility a flexible tool to investigate MHD-flow phenomena, *Wissenschaftlicher Bericht FZKA 5821*, Forschungszentrum Karlsruhe.

Batchelor, G. K.: 1959, Small-scale variation of convected quantities like temperature in turbulent fluid, *J. Fluid Mech.* **5**, 113–139.

Bühler, L.: 1996, Instabilities in quasi-two-dimensional magnetohydrodynamic flows, *J. Fluid Mech.* **326**, 125–150.

Burr, U.: 1998, Turbulente Transportvorgänge in magnetohydrodynamischen Kanalströmungen, *Wissenschaftlicher Bericht FZKA 6038*, Forschungszentrum Karlsruhe.

Burr, U. and Müller, U.: 1997, Der Einfluß magnetischer Felder auf eine von unten beheizte Schicht aus elektrisch leitender Flüssigkeit, *Wissenschaftlicher Bericht FZKA 5965*, Forschungszentrum Karlsruhe.

Burr, U., Barleon, L., Mack, K.-J. and Müller, U.: 1999, The effect of vertical magnetic field on liquid metal Rayleigh-Bénard convection, *Wissenschaftlicher Bericht FZKA 6267*, Forschungszentrum Karlsruhe.

Busse, F.: 1978, Non-linear properties of thermal convection, *Rep. Prog. Phys.* **41**, 1929–1967.

Busse, F. and Clever, R.: 1983, Stability of convection rolls in the presence of a horizontal magnetic field, *Journal de Mécaniquie et Appliquée* **2(4)**, 495–502.

Busse, F. and Clever, R.: 1989, Traveling-wave convection in the presence of a horizontal magnetic field, *Physical Review A* **40(4)**, 1954–1961.

Chandrasekhar, S.: 1961, *Hydrodynamic and Hydromagnetic Stability*, Dover Publications, Inc. New York.

Chu, T. and Goldstein, R.: 1973, Turbulent convection in a horizontal layer of water, *J. Fluid Mech.* **60**, 141–159.

Clever, R. and Busse, F.: 1974, Transition to time dependent convection, *J. Fluid Mech.* **65**, 625–645.

Davidson, P. A.: 1995, Magnetic damping of jets and vortices, *J. Fluid Mech.* **299**, 153–186.

Fauve, S., Laroche, C. and Libchaber, A.: 1981, Effect of a horizontal magnetic field on convective instabilities in mercury, *J. Physique-Lettres* **42**, L–455 – L–457.

Fauve, S., Laroche, C., Libchaber, A. and Perrin, B.: 1984, Chaotic phases and magnetic order in a convective fluid, *Physical Review Letters* **52(20)**, L–211 – L–216.

Foust, O.: 1972, *Sodium-NaK Engineering Handbook*, Vol. 1, Gordon and Breach SCIENCE Publishers; ISBN 0677030204.

Giancarli, L., Severy, Y., Baraer, L., Leroy, P., Mercier, J., Proust, E. and Quintric-Bossy, J.: 1992, Water-cooled lithium-lead blanket design studies for DEMO reactor: Definition and recent developments of the box-shaped concept, *Fusion Technology* **21**, 2081–2088.

Gieck, K.: 1981, *Technische Formelsammlung*, Gieck Verlag Heilbronn/N.

Hinze, J. O.: 1975, *Turbulence*, McGraw-Hill, Inc.

Kek, V.: 1989, Bénardkonvektion in flüssigen Natriumschichten, *Bericht KfK 4611*, Kernforschungszentrum Karlsruhe.

Kishida, Y. and Takeda, K.: 1994, Suppression of turbulent Bénard convection by horizontal D.C. magnetic field, *Proc. Int. Symp. on Electromagnetic Processing of Materials, October 25-28, Nagoya, Japan, ISIJ* pp. 80–85.

Krishnamurti, R.: 1973, Some further studies on the transition to turbulent convection, *J. Fluid Mech.* **60**, 285–303.

Lehnert, L. and Little, N. C.: 1956, Experiments on the effect of inhomogeneity and obliquity of a magnetic field inhibiting convection, *Tellus* **9**, 97–103.

Libchaber, A., Fauve, S. and Laroche, C.: 1983, Two parameter study of the route to chaos, *Physica* **7D**, 73–84.

Libchaber, A., Laroche, C. and Fauve, S.: 1982, Period doubling cascade in mercury a quantitative measurement, *J. Physique-Lettres* **43**, L–211 – L–216.

Lyon, N.: 1952, *Liquid metals handbook*, Navexos P-733; Second edition.

O'Donnel, J. O., Papanicolaou, P. G. and Reed, C. B.: 1989, The thermophysical and transport properties of eutectic NaK near room temperature, *Technical report*, ANL/FPP/TM-237.

Pellew, A. and Southwell, R.: 1940, On maintained convective motion in a fluid heated from below, *Proc. R. Soc. (London)* **A176**, 312–343.

Reid, W. and Harris, D.: 1958, Some further results on the Bénard problem, *Phys. Fluids* **1**, 102–110.

Shercliff, J. A.: 1965, *A textbook of Magnetohydrodynamics*, Pergamon Press, Oxford.

Sommeria, J. and Moreau, R.: 1982, Why, how and when, MHD turbulence becomes two-dimensional, *J. Fluid Mech.* **118**, 507–518.

Stork, K. and Müller, U.: 1972, Convection in boxes (Experiments), *J. Fluid Mech.* **54**, 599–611.

Walker, J. S.: 1981, Magnetohydrodynamic duct flows in rectangular ducts with thin conducting walls I, *Journal de Mécanique* **20(1)**, 79–112.

A Thermophysical data

A.1 Eutectic sodium-potassium alloy $Na^{22}K^{78}$

Temperature dependent thermophysical properties of sodium-potassium $Na^{22}K^{78}$ are obtained from Lyon (1952), O'Donnel, Papanicolaou and Reed (1989), and Foust (1972). The values are fitted by polynominal regression leading to the equations below for:
   density

$$\rho(T) = 873.35 - 0.258 \cdot T \quad [kg/m^3]; \quad 0°C < T < 204°C \tag{56}$$

kinematic viscosity

$$\nu(T) = 0.89994 - 0.00328 \cdot T + 4.88 \cdot 10^{-6} \cdot T^2 \quad [10^{-6}m^2/s]; \quad 0°C < T < 300°C \tag{57}$$

thermal conductivity

$$\lambda(T) = 21.38 + 0.0208 \cdot T - 2.207 \cdot 10^{-5} \cdot T^2 \quad [W/mK]; \quad 0°C < T < 400°C \tag{58}$$

specific heat

$$c_p(T) = 990.7 - 0.5133 \cdot T + 5.37 \cdot 10^{-4} \cdot T^2 \quad [J/kgK]; \quad 0°C < T < 450°C \tag{59}$$

electrical conductivity

$$\sigma(T) = 2.976 \cdot 10^6 - 5.05 \cdot 10^3 \cdot T + 7.188 \cdot T^2 \quad [10^6 1/\Omega m]; \quad 0°C < T < 400°C. \tag{60}$$

B Calculation of temperature gradient ∇T

In figure 32 the sensing tip of the probe consisting of four thermocouples is sketched. The probe coordinate system is parallel to the coordinate system of the test section in
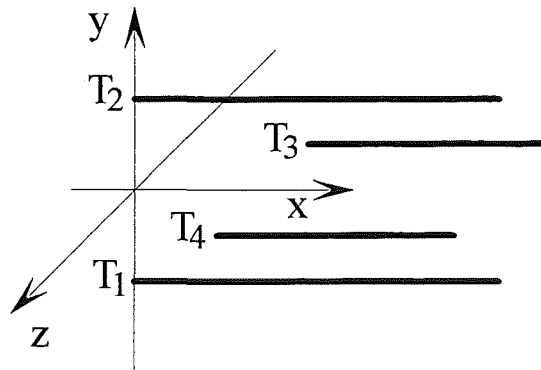
Figure 32: Arrangement of the thermocouples at the sensing tip of the four thermocouples temperature probe. T_1 and T_2 are laying in the x, y-plane, T_3 and T_4 in the x, z-plane.

figure 8. Before the probe was inserted into the test section, the exact coordinates of the measurement positions x_i, y_i, z_i of the thermocouples T_i have been determined by a

	$x_i[mm]$	$y_i[mm]$	$z_i[mm]$
T_1	0.102	−1.000	0.000
T_2	0.000	1.000	0.000
T_3	1.217	0.000	−1.000
T_4	1.315	−1.000	1.000

Table 2: Coordinates of the probe thermocouples

microscope to an accuracy of $0.001mm$. After glueing the thermocouples into the shaft, their axial position can no longer be adjusted. This leads to small deviations of the values summarized in table 2 from the rated values given in figure 9.

If the temperatures T_{1-4} are all known from a simultaneous measurement, the components of the local temperature gradient $\nabla T = (\partial_x T, \partial_y T, \partial_z T)$ are approximated by finite differences between the thermocouples as:

$$\partial_x T = \frac{T_3 + T_4 - T_1 - T_2}{x_3 + x_4 - x_1 - x_2}, \tag{61}$$

$$\partial_y T = \frac{T_2 - T_1}{y_2 - y_1}, \tag{62}$$

and

$$\partial_z T = \frac{T_3 - T_4}{z_3 - z_4}. \tag{63}$$

C Standard polynomes for thermo-potentials

The temperature $T[°C]$ is calculated from the thermo-voltage $U[V]$ measured in reference to an ice point of exactly $0°C$ using the polynomes below.

For $Cu - CuNi$ thermopairing:

$$T = 0.3705 + 25269.6 \cdot U - 511600 \cdot U^2 + 1.14 \cdot 10^7 \cdot U^3 \tag{64}$$

For $Ni - CrNi$ thermopairing:

$$T = 0.0989 + 25092.6 \cdot U - 273900 \cdot U^2 + 2.67 \cdot 10^7 \cdot U^3 \tag{65}$$

D Statistical properties of time dependent data

Generally any flow quantity is an arbitrary function of space (x, y, z) and time t, so the temporal behavior of a flow quantity Φ at a fixed position may not be described by simple mathematical functions. Thus temporal characteristics of a signal, obtained from a measurement, have to be described by statistic properties. The definitions below are limited to fully developed (non-transient) conditions where no evaluated quantity depends on the moment of its measurement.

It is convenient to split up the present value of a flow quantity $\Phi(t)$ into its temporal mean value $\overline{\Phi}$ denoted by an overbar and its fluctuating part $\Phi'(t)$ denoted by a prime:

$$\Phi(x, y, z, t) = \overline{\Phi(x, y, z)} + \Phi'(x, y, z, t), \tag{66}$$

where the temporal mean value in the time period τ is defined by

$$\overline{\Phi(x,y,z)} = \frac{1}{\tau} \int\limits_0^\tau \Phi(x,y,z,t)\ dt. \tag{67}$$

The time period τ has to be chosen such long that the mean value becomes independent from any further increase of it. With this definition, the mean value of the fluctuating part is always zero:

$$\overline{\Phi'} = 0. \tag{68}$$

D.1   Correlations

The temporal mean values of products of fluctuating parts

$$Q = \overline{\Phi_1'\Phi_2'.....\Phi_n'} = \frac{1}{\tau} \int\limits_0^\tau \Phi_1' \cdot \Phi_1' \cdot .... \cdot \Phi_n'\, dt \tag{69}$$

are called correlations. If they are calculated from two ore more identical signals

$$\overline{\Phi'^{\,n}} = \frac{1}{\tau} \int\limits_0^\tau \Phi'^{\,n}\, dt, \tag{70}$$

one obtains the n-th order moments of Φ'.

At $n = 2$ we obtain the mean-square (ms-) value

$$s^2 = \overline{\Phi'^{\,2}}, \tag{71}$$

its square root

$$s = \sqrt{\overline{\Phi'^{\,2}}} \tag{72}$$

is the root-mean-square (rms-) value.

Correlations, normalized by the rms-values

$$K = \frac{\overline{\Phi_1'\Phi_2'.....\Phi_n'}}{\sqrt{\overline{\Phi_1'^{\,2}}} \cdot \sqrt{\overline{\Phi_1'^{\,2}}} \cdot ...... \cdot \sqrt{\overline{\Phi_n'^{\,2}}}}. \tag{73}$$

are called correlation coefficients. They become one for identical signals and zero for statistically independent signals.

D.2   Correlation functions

Any correlation or correlation coefficient may be expressed as a dependency from one ore more parameters e.g. space or time what results in so called correlation functions.

Thus the autocorrelation function is obtained from the correlation coefficient of a time dependent signal with the identical signal at varying time shift $\underline{t}$:

$$A_K(\underline{t}) = \frac{1}{\tau\overline{\Phi'^2}} \int\limits_0^\tau \Phi'(t) \cdot \Phi'(t+\underline{t})dt. \tag{74}$$

D.3 Power spectra

Any time series $\Phi(t)$ that is known in the time period τ can be expressed by a Fourier series:

$$\Phi(t) = \frac{a_0}{2} + \sum_{n=1}^{\infty} A_n \sin(\omega_n t + \varphi_n) \tag{75}$$

$$A_n = \sqrt{a_n^2 + b_n^2}, \quad \tan\varphi_n = \frac{a_n}{b_n}, \quad \omega_n = \frac{2\pi \cdot n}{\tau}$$

$$a_n = \frac{2}{\tau} \int_0^{\tau} \phi(t) \cos(\omega_n t) \, dt, \quad n = 0, 1, 2, \ldots$$

$$b_n = \frac{2}{\tau} \int_0^{\tau} \phi(t) \sin(\omega_n t) \, dt, \quad n = 0, 1, 2, \ldots$$

Introducing equation 75 in the definition of the ms-value (equation 71) one obtains for $\tau \to \infty$:

$$\overline{\Phi'^2} = \frac{1}{2} \sum_{n=1}^{\infty} A_n^2 = \sum_{n=1}^{\infty} S_n. \tag{76}$$

The discrete elements S_n are indicating the contribution of fluctuations of the discrete frequency

$$f_n = \frac{\omega_n}{2\pi} = \frac{n}{\tau} \tag{77}$$

to the ms-value. Their functional dependance from f_n is called the power spectra S of the function $\Phi(t)$.

In order to lower the statistic error, the elements of the power spectra S_n can be calculated as an average of M values obtained from M different time series:

$$< S_n >_M = \frac{1}{M} \sum_{i=1}^{M} S_{n,i}. \tag{78}$$

The average value $< S_n >_M$ is denoted by brackets, $S_{n,i}$ is the value of S_n obtained in the i-th time period. The functional dependance from f_n is denoted by $< S >_M$.

D.4 Statistical averaging of data

Suppose a time dependent signal $\Phi(t)$, known in the time period τ, consists of a true part caused by some physical effect $\Phi_r(t)$ we are interested in and a part caused by some random disturbances $\Phi_s(t)$:

$$\Phi(t) = \Phi_r(t) + \Phi_s(t) \tag{79}$$

All three functions can be expressed by Fourier series (equation 75):

$$\Phi(t) = \sum_{n=1}^{\infty} A_n \sin(\omega_n t + \varphi_n) \tag{80}$$

$$\Phi_r(t) = \sum_{n=1}^{\infty} A_{n,r} \sin(\omega_n t + \varphi_{n,r}) \tag{81}$$

63

$$\Phi_s(t) \;=\; \sum_{n=1}^{\infty} A_{n,s}\, sin(\omega_n t + \varphi_{n,s}) \tag{82}$$

where the phase of $\Phi_r(t)$ can be defined as zero ($\varphi_{n,r} = 0$) for any angular velocity ω_n. Introducing equations 80 - 82 to 79 and calculating the ms-values (equation 71) of each side we obtain for the Fourier coefficients:

$$A_n^2 = A_{n,r}^2 + A_{n,s}^2 + 2 \cdot A_{n,r} \cdot A_{n,s} \cdot cos(\varphi_{n,s})$$

If we consider an infinite number of time series ($M >> 1$) the following conditions hold:

- The probability distributions of $A_{n,r}, A_{n,s}$ and $\varphi_{n,s}$ are independent from each other.

- $\varphi_{n,s}$ is even distributed:

$$\rho(\varphi_{n,s}) = \frac{1}{2\pi}; 0 \le \varphi_{n,s} \le 2\pi$$

And we obtain after averaging over an infinite number of time series:

$$< A_n^2 > = < A_{n,r}^2 > + < A_{n,s}^2 > + 2 \cdot \underbrace{\underbrace{< A_{n,r} \cdot A_{n,s} \cdot cos(\varphi_{n,s}) >}_{=<A_{n,r}> \cdot <A_{n,s}> \cdot \underbrace{< cos(\varphi_{n,s}) >}_{=0}}} \tag{83}$$

Using equation 76 the coefficients of the power spectra

$$< S_n > = < S_{n,r} > + < S_{n,s} > \tag{84}$$

and the ms values

$$< \overline{\Phi'^2} > = < \overline{\Phi_r'^2} > + < \overline{\Phi_s'^2} > \tag{85}$$

can easily be derived.

D.5 Some remarks on data obtained from measurements

From a measurement $\Phi(t)$ is not obtained as a continous function. In a time period τ, discrete values Φ^t are acquired at an acquisition frequency f_{aq}, where the index t runs from $t = 1$ to the number of acquired points $t = N$ calculated from $N = f_{aq} \cdot \tau$. Statistical properties as they are defined in the above sections have therefore to be calculated using reasonable assumptions. For example, the mean value of $\Phi(t)$ (equation 67) is approximated by

$$\overline{\Phi} = \frac{1}{N} \sum_{t=1}^{N} \Phi^t. \tag{86}$$

A Fourier series (see equation 75) calculated from a discrete time series is limited to a finite number of Fourier coefficients A_n, where the index n runs from 1 to $N/2$. In such a discrete Fourier series only contributions between the lowest frequency $f_{min} = 1/\tau$ and the highest frequency $f_{max} = f_{aq}/2$ occur. Thus the power spectra defined from equation 76 is not a continuous function but a series of limited elements. In the discussion this point is sometimes neglected but when all relevant frequencies of a signal have been covered in the measurement by a long enough acquisition time and a high enough acquisition frequency the discrete functions are well represented by the series.

64

E   Performed experiments

In the tables below the essential physical parameters and non-dimensional numbers of the experiments are summarized. P is the elctrical power supplied to the test section, H indicates the used power supply (k: controlled, g: non-controlled), B is the magnitude of the applied magnetic field, q the resulting heat flux after taking into account heat losses (see section 4.4), ΔT the measured temperature difference across the layer, T_m the mean temperature of the fluid, Q the Chandrasekhar number, Ra the Rayleigh number, Pr the Prandtl number and Nu the Nusselt number. The critical Rayleigh number Ra_c is obtained from linear theory (see section 3.4) and based on the magnetic damping parameter $1/\tau$ as defined from equation 40.

E.1   Test matrix $M0$, short time series at $P \approx 2400W$

P	H	B	q	ΔT	T_m	$Q^{1/2}$	Ra	Pr	Nu
[W]		[T]	[W/m²]	[°C]	[°C]				
2419.4	k	0	2.82E+04	14.45	110.24	0	19677	0.020	1.67
2402.8	k	9.53E-02	2.80E+04	16.32	113.31	132	22402	0.020	1.46
2404.7	k	1.46E-01	2.81E+04	16.05	114.03	203	22072	0.020	1.49
2402.2	k	1.88E-01	2.81E+04	14.60	112.51	260	19999	0.020	1.64
2401.4	k	2.80E-01	2.80E+04	14.61	112.59	387	20010	0.020	1.64
2401.3	k	3.74E-01	2.80E+04	16.89	113.81	519	23205	0.020	1.41
2398.1	k	4.22E-01	2.79E+04	19.39	115.17	586	26746	0.020	1.22
2400.3	k	4.67E-01	2.79E+04	20.16	115.52	649	27828	0.020	1.18
2397.0	k	5.59E-01	2.78E+04	21.57	116.24	777	29832	0.020	1.10
2398.2	k	6.53E-01	2.78E+04	22.31	116.61	908	30881	0.020	1.06
2397.6	k	7.44E-01	2.78E+04	23.06	117.06	1036	31953	0.020	1.02
2397.4	k	8.65E-01	2.78E+04	23.39	117.06	1204	32414	0.020	1.01

E.2   Test matrix $M1$, short time series

E.2.1   Ordinary hydrodynamic flow $(Q^{1/2} = 0)$:

$1/\tau = 0$, $Ra_c \approx 1708$

P	H	B	q	ΔT	T_m	$Q^{1/2}$	Ra	Pr	Nu
[W]		[T]	[W/m²]	[°C]	[°C]				
169.7	k	0	1.26E+03	0.97	101.60	0	1295	0.021	1.12
199.6	k	0	1.62E+03	1.33	101.59	0	1766	0.021	1.05
244.3	k	0	2.16E+03	1.75	102.23	0	2330	0.021	1.06
311.4	k	0	2.97E+03	2.34	101.81	0	3116	0.021	1.09
496.5	k	0	5.17E+03	3.61	103.30	0	4833	0.021	1.23
754.1	k	0	8.24E+03	5.28	104.49	0	7077	0.021	1.34
1014.5	k	0	1.13E+04	7.01	106.78	0	9463	0.021	1.38
1202.6	k	0	1.36E+04	8.04	107.23	0	10867	0.021	1.45
1808.9	k	0	2.09E+04	11.28	108.85	0	15300	0.020	1.58
2419.4	k	0	2.82E+04	14.45	110.24	0	19677	0.020	1.67
2275.9	g	0	2.65E+04	13.73	112.19	0	18789	0.020	1.65
3526.8	g	0	4.16E+04	19.77	115.38	0	27273	0.020	1.79
5178.7	g	0	6.15E+04	26.80	120.24	0	37452	0.019	1.95
6929.8	g	0	8.26E+04	33.67	125.22	0	47655	0.019	2.08
8746.2	g	0	1.05E+05	40.34	130.19	0	57836	0.018	2.19
10430.0	g	0	1.25E+05	45.97	134.46	0	66641	0.018	2.28

E.2.2 MHD flow at $Q^{1/2} \approx 200$:

$1/\tau = 36.6$, $Ra_c \approx 3653$

P	H	B	q	ΔT	T_m	$Q^{1/2}$	Ra	Pr	Nu
[W]		[T]	[W/m²]	[°C]	[°C]				
198.5	k	1.49E-01	1.62E+03	0.97	102.63	204	1301	0.021	1.01
240.0	k	1.49E-01	2.11E+03	1.39	102.86	204	1866	0.021	1.00
361.4	k	1.46E-01	3.59E+03	2.42	103.43	200	3238	0.021	1.10
503.0	k	1.46E-01	5.28E+03	3.51	104.30	200	4706	0.021	1.17
603.6	k	1.46E-01	6.48E+03	4.22	104.89	200	5676	0.021	1.22
903.1	k	1.46E-01	1.01E+04	6.04	106.56	201	8155	0.021	1.35
1204.2	k	1.46E-01	1.36E+04	8.01	109.20	201	10882	0.020	1.40
1806.6	k	1.46E-01	2.09E+04	12.84	112.10	202	17573	0.020	1.35
1802.1	k	1.47E-01	2.09E+04	12.01	111.69	203	16422	0.020	1.44
1804.3	k	1.47E-01	2.09E+04	12.43	112.02	203	17010	0.020	1.40
2404.7	k	1.46E-01	2.81E+04	16.05	114.03	203	22075	0.020	1.46
2999.0	k	1.46E-01	3.52E+04	19.68	115.77	203	27182	0.020	1.49
3606.4	k	1.46E-01	4.25E+04	22.85	117.51	204	31713	0.020	1.55
3996.1	k	1.46E-01	4.72E+04	24.66	118.44	204	34304	0.019	1.60
5346.4	g	1.44E-01	6.35E+04	32.42	123.70	202	45713	0.019	1.65
6998.5	g	1.44E-01	8.34E+04	39.60	128.61	203	56548	0.019	1.78
8743.5	g	1.43E-01	1.04E+05	47.35	133.83	204	68528	0.018	1.86

E.2.3 MHD flow at $Q^{1/2} \approx 400$:

$1/\tau = 106.4$, $Ra_c \approx 6971$

P	H	B	q	ΔT	T_m	$Q^{1/2}$	Ra	Pr	Nu
[W]		[T]	[W/m²]	[°C]	[°C]				
400.2	k	2.92E-01	4.04E+03	3.34	102.78	399	4458	0.021	1.04
507.1	k	2.92E-01	5.33E+03	4.41	103.09	400	5892	0.021	1.04
605.4	k	2.93E-01	6.51E+03	5.25	103.63	401	7023	0.021	1.07
905.2	k	2.92E-01	1.01E+04	7.60	107.36	402	10276	0.021	1.13
1201.9	k	2.90E-01	1.36E+04	9.48	109.37	400	12879	0.020	1.23
1801.2	k	2.90E-01	2.08E+04	11.81	110.97	400	16114	0.020	1.51
2402.5	k	2.90E-01	2.81E+04	13.95	111.55	401	19058	0.020	1.72
3599.4	k	2.90E-01	4.25E+04	18.69	114.56	402	25730	0.020	1.94
3902.9	k	2.90E-01	4.62E+04	19.77	115.23	402	27265	0.020	1.99
3487.2	g	2.88E-01	4.11E+04	22.16	117.16	400	30715	0.020	1.58
4230.2	g	2.88E-01	5.00E+04	26.78	120.07	402	37408	0.019	1.59
5341.8	g	2.83E-01	6.33E+04	35.60	125.42	397	50417	0.019	1.50
6992.6	g	2.83E-01	8.31E+04	45.56	131.90	401	65605	0.018	1.54
6980.2	g	2.88E-01	8.30E+04	44.61	131.45	408	64162	0.018	1.57
8743.7	g	2.83E-01	1.04E+05	53.94	137.39	403	78782	0.018	1.62

E.2.4 MHD flow at $Q^{1/2} \approx 600$:

$1/\tau = 209.5$, $Ra_c \approx 11386$

P	H	B	q	ΔT	T_m	$Q^{1/2}$	Ra	Pr	Nu
[W]		[T]	[W/m²]	[°C]	[°C]				
401.9	k	4.41E-01	4.08E+03	3.12	104.39	604	4185	0.021	0.91
601.0	k	4.41E-01	6.44E+03	4.75	105.60	605	6395	0.021	1.02
901.5	k	4.37E-01	1.00E+04	7.60	106.71	601	10254	0.021	1.03
1197.2	k	4.35E-01	1.35E+04	10.40	110.38	600	14170	0.020	1.03
1804.7	k	4.35E-01	2.08E+04	15.69	114.04	603	21576	0.020	1.08
1906.4	k	3.39E-01	2.21E+04	15.37	113.89	470	21129	0.020	1.18
2403.5	k	4.35E-01	2.80E+04	18.81	115.69	604	25977	0.020	1.23
3015.1	k	4.33E-01	3.54E+04	23.05	117.71	604	32000	0.020	1.27
3607.9	k	4.33E-01	4.26E+04	22.67	117.92	604	31490	0.020	1.56
3901.8	k	4.34E-01	4.61E+04	24.03	118.79	605	33451	0.019	1.60
4170.3	g	4.32E-01	4.93E+04	26.35	119.13	603	36712	0.019	1.59
5273.1	g	4.29E-01	6.26E+04	31.74	123.51	602	44730	0.019	1.67
7086.3	g	4.25E-01	8.44E+04	40.58	129.46	600	58076	0.018	1.76
8766.4	g	4.24E-01	1.05E+05	49.30	135.37	604	71650	0.018	1.78

E.2.5 MHD flow at $Q^{1/2} \approx 800$:

$1/\tau = 345.7$, $Ra_c \approx 17075$

P	H	B	q	ΔT	T_m	$Q^{1/2}$	Ra	Pr	Nu
[W]		[T]	[W/m²]	[°C]	[°C]				
1211.7	k	5.79E-01	1.37E+04	11.48	109.53	799	15598	0.020	1.02
1413.4	k	5.79E-01	1.61E+04	13.36	111.67	801	18265	0.020	1.03
1625.9	k	5.79E-01	1.86E+04	15.49	112.77	802	21226	0.020	1.02
1804.9	k	5.79E-01	2.07E+04	17.04	113.72	803	23417	0.020	1.04
1991.9	k	5.79E-01	2.29E+04	18.62	114.61	804	25635	0.020	1.05
2363.7	k	5.79E-01	2.74E+04	21.59	116.15	805	29853	0.020	1.08
2704.0	k	5.76E-01	3.15E+04	23.75	117.62	803	32957	0.020	1.13
3047.4	k	5.79E-01	3.56E+04	25.14	117.91	807	34911	0.020	1.20
3614.5	k	5.79E-01	4.24E+04	29.15	120.43	809	40748	0.019	1.24
3904.1	k	5.80E-01	4.59E+04	29.65	120.14	810	41418	0.019	1.31
3964.7	k	5.78E-01	4.67E+04	31.09	122.69	809	43718	0.019	1.27
3542.3	g	5.75E-01	4.16E+04	28.42	120.73	803	39764	0.019	1.24
4207.3	g	5.72E-01	4.96E+04	33.38	123.74	803	47062	0.019	1.26
5259.1	g	5.69E-01	6.23E+04	37.30	126.66	802	52994	0.019	1.41

E.3 Test matrix $M3$, long time series with $Ra \approx 5 \cdot 10^4$

$\tau = 8192 \ s$, $f_{aq} = 128 \ Hz$, $N = 1048576$ (for probe only)

P	H	B	q	ΔT	T_m	$Q^{1/2}$	Ra	Pr	Nu
$[W]$		$[T]$	$[W/m^2]$	$[^\circ C]$	$[^\circ C]$				
7073.2	g	0	8.43E+04	34.53	126.76	0	49072	0.019	2.06
5959.3	g	1.44E-01	7.09E+04	35.27	125.93	202	50011	0.019	1.70
5161.8	g	2.85E-01	6.11E+04	35.66	125.22	401	50481	0.019	1.45
5946.0	g	4.29E-01	7.07E+04	34.85	125.84	603	49405	0.019	1.72
4852.8	g	5.71E-01	5.74E+04	35.21	125.01	802	49810	0.019	1.38

F Symbols

Skalar Properties:

a	horizontal wave number
a_c	critical wave number
A_n	Fourier coefficients
$A_k(t)$	autocorrelation function
A_{xz}	horizontal isotropy coefficient
A_{yz}	vertical isotropy coefficient
b	half of distance between Hartmann walls
B_0	magnitude of magnetic induction
c_p	specific heat capacity
c	wall conductance ratio
c_H	wall conductance ratio of Hartmann wall
d	vortex diameter
e_b	energy released by buoyant forces
$E(f_n)$	integrated power spectra
f	frequency
f	shape function
f_n	discrete frequency n
$f_0 = \kappa/h^2$	characteristic frequency
f_{aq}	aquisition frequency
F_b	buoyant forces
F_{is}	non-stationary inertial forces
F_{iu}	stationary inertial forces
g	magnitude of acceleration of gravity ($g = 9.81 m/s^2$)
h	hight of the liquid metal layer
k_e	kinetic energy
K	correlation coefficient
$l_\perp$	lengthscale perpendicular to $\mathbf{B}$
l	lengthscale in direction of $\mathbf{B}$
p	pressure
p^*	non-dimensional pressure
P	power
Q	correlation
q	magnitude of heat flux
q_0	heat flux equivalent to pure heat conduction
q_{co}	convective heat flux
S	power spectra
S	discrete element of power spectra n
S_T	power spectra of temperature fluctuations
S_v	power spectra of velocity fluctuations
s	root-mean-square (rms-) value
s	wall thickness
s^2	mean-square (ms-) value

t	time; discrete time step when used as upper index
$t_0 = v_0/a$	characteristic time
$t_0 = h^2/\kappa$	thermal diffusion time
T	temperature
T_b	temperature of the bottom plate
T_m	mean temperature of the fluid
T_t	temperature of the top plate
T_e	temperature of the environment
ΔT	temperature difference across the layer
$T_{i,j}$	temperatures in the copper plates
	index $i = M$ (central) or N, S, E, W (four winds)
	index $j = b$ (bottom plate) or t (top plate)
T_{1-4}	temperatures of the probe elements
U	voltage
U_T	thermo-voltage
u	velocity in x-direction
v	velocity in y-direction
w	velocity in z-direction
$v_0 = \kappa/h$	characteristic velocity
v_b	buoyant velocity
x, y, z	cartesian coordinate system
x_i, y_i, z_i	position of probe thermocouple T_i
α	diffusivity of $\boldsymbol{\omega}$ along $\mathbf{B}$
β	cubic thermal expansion coefficient
Γ	signal to noise ratio
Γ_n	signal to noise ratio at discrete frequency
δ_H	thickness of Hartmann layer
δU	resolution of voltage
δT	resolution of temperature
ζ	rescaled boundary layer coordinate
κ	thermal diffusivity
λ	thermal conductivity
λ_{Cu}	thermal conductivity of copper
λ_c	critical wavelength
μ	magnetic permeability
ν	kinematic viscosity
ρ	density
σ	electrical conductivity
σ_W	electrical conductivity of walls

τ	time period
τ	similarity parameter of magnetic damping
τ_I	integral time-scale
τ_{JD}	Joule's dissipation time-scale
τ_{VD}	viscous dissipation time-scale
τ_{to}	eddy turnover time
τ_H	Hartmann braking time-scale
ϕ	electric potential
Φ	arbitrary Variable
ψ	stream function
ω	vorticity in x-direction $(\omega = \omega_x)$
ω_n	discrete angular velocity n

Vectors (bold):

$\mathbf{B} = (b_x, b_y, b_z)$	magnetic field
$\mathbf{E} = (e_x, e_y, e_z)$	electric field
$\mathbf{F}_L$	Lorentz force
$\mathbf{e}_x, \mathbf{e}_y, \mathbf{e}_z$	unit vectors in spacial directions x, y and z
$\mathbf{g}$	acceleration of gravity
$\mathbf{j} = (j_x, j_y, j_z)$	current density
$\mathbf{q} = (q_x, q_y, q_z)$	heat flux
$\mathbf{v} = (u, v, w)$	velocity
$\boldsymbol{\omega} = (\omega_x, \omega_y, \omega_z)$	vorticity $\boldsymbol{\omega} = \nabla \times \mathbf{v}$

Characteristic numbers:

M	Hartmann-Number
N	Interaction parameter
Nu	Nusselt number
Pr	Prandtl number
Q	Chandrasekhar number
Ra	Rayleigh number
Ra_c	critical Rayleigh number (for onset of convection)
Ra_t	critical Rayleigh number (for onset of time dependent flow)
Ra_r	reduced Rayleigh number $Ra_r = Ra - Ra_c$
Re	Reynolds number (based on h)
Re_d	Reynolds number (based on d)
Pm	magnetic Prandtl number

Mathematical notation:

∇	gradient
$\nabla\cdot$	divergence
∇^2	laplacian
∇^2_{yz}	vertical laplacian
$\nabla\times$	curl
$\frac{\partial}{\partial x_i}\Phi = \partial_{x_i}\Phi$	partial derivative of Φ in x_i-direction
$\overline{\Phi}$	temporal mean value of Φ
Φ'	fluctuating part of Φ
$<\Phi>_M$	average over M samples